Durham E-Theses

Correlated magnetic oxides studied using muon-spin spectroscopy

WILLIAMS, ROBERT,CHARLES

How to cite:

Use policy

Correlated magnetic oxides studied using muon-spin spectroscopy

Robert C. Williams

A thesis presented for the degree of
Doctor of Philosophy

Department of Physics
Durham University
UK

March 2016

Abstract

This thesis is concerned with the application of muon-spin spectroscopy (μSR) in the study of correlated magnetic oxides. The results of four studies are presented, where μSR is used to provide insight into both the static and dynamic magnetic behaviours of the materials in question.

The results of μSR measurements on the double perovskite compounds Sr_2BOsO_6 (B = Co, Fe, Y, In) are presented. The Co compound exhibits lattice-site-specific ground states and spin dynamics with two distinct, partially ordered antiferromagnetic states encountered upon cooling from room temperature. Here, and also for the Fe compound, the μSR results reveal the evolution of the internal fields through the phase transitions and as dynamic relaxation channels freeze out on further cooling. The possibility of incommensurate magnetic ordering is considered for the Y and In compounds.

The magnetic properties of the tetrahedral spin-chain oxide $CsCoO_2$ are investigated using μSR, with results that are consistent with a magnetic structure comprising ferromagnetically ordered Co-Co spin dimers, themselves arranged in antiferromagnetic chains. The critical behaviour near T_N and the magnetostructural coupling in the vicinity of a structural phase transition are examined. These results help elucidate a complex freezing out of relaxation processes upon cooling, induced by a bifurcation of superexchange bond angles.

A revised magnetic phase diagram is reported for the antiferromagnetic insulating series $La_{2-x}Sr_xCoO_4$, which has been shown to support charge ordered and magnetic stripe phases and an hourglass magnetic excitation spectrum. It is found that the suppression of the magnetic ordering temperature is highly sensitive to small concentrations of holes. Distinct behaviour within an intermediate x range suggests that the putative stripe ordered phase extends to lower x than previously thought, whereas further charge doping prevents magnetic ordering for $T \gtrsim 1.5$ K.

Finally, the results of the first transverse field μSR measurements to be made on a skyrmion lattice phase are presented. The muon response to that phase and the surrounding ones within Cu_2OSeO_3 is used to demonstrate how the technique is sensitive to the skyrmion lattice via the frequency domain lineshape.

Declaration

The work in this thesis is based on research carried out under the supervision of Dr Tom Lancaster, in the Department of Physics, University of Durham, England. No part of this thesis has been submitted elsewhere for any other degree or qualification and it is all my own work unless referenced to the contrary in the text.

Copyright © 2016 by Robert C. Williams.

Publications

- B. Yan, A. K. Paul, S. Kanungo, M. Reechius, A. Hoser, D. M. Többens, W. Schnelle, **R. C. Williams**, T. Lancaster, F. Xiao, J. S. Möller, S. J. Blundell, W. Hayes, C. Felser and M. Jansen. "Lattice-Site-Specific Spin Dynamics in Double Perovskite Sr_2CoOsO_6". *Phys. Rev. Lett.*, **112**, 147202 (2014). *This work forms part of Chap. 3.*

- **R. C. Williams**, F. Xiao, I. O. Thomas, S. J. Clark, T. Lancaster, G. A. Cornish, S. J. Blundell, W. Hayes, B. Yan, A. K. Paul, C. Felser and M. Jansen. "Muon-spin relaxation study of the double perovskite insulators Sr_2BOsO_6 ($B = Fe, Y, In$)". *J. Phys. Condens. Matter*, **28**, 076001 (2016). *This work forms part of Chap. 3.*

- N. Z. Ali, **R. C. Williams**, F. Xiao, S. J. Clark, T. Lancaster, S. J. Blundell, D. V. Sheptyakov, and M. Jansen. "Magnetostructural relationship in the tetrahedral spin-chain oxide $CsCoO_2$". *Phys. Rev. B*, **91**, 024419 (2015). *This work forms the basis of Chap. 4.*

- **R. C. Williams**, F. Xiao, T. Lancaster, R. De Renzi, S. Bordignon, P. G. Freeman, F. L. Pratt, S. R. Giblin, J. S. Möller, S. J. Blundell, A. T. Boothroyd and D. Prabhakaran. "Magnetic phase diagram of $La_{2-x}Sr_xCoO_4$ revised using muon-spin relaxation". *Phys. Rev. B*, **93**, 140406(R) (2016). *This work forms the basis of Chap. 5.*

- T. Lancaster, **R. C. Williams**, I. O. Thomas, F. Xiao, F. L. Pratt, S. J. Blundell, J. C. Loudon, T. Hesjedal, S. J. Clark, P. D. Hatton, M. Ciomaga Hatnean, D. S. Keeble and G. Balakrishnan. "Transverse field muon-spin rotation signature of the skyrmion-lattice phase in Cu_2OSeO_3". *Phys. Rev. B*, **91**, 224408 (2015). *This work forms the basis of Chap. 6.*

- F. Xiao, J. S. Möller, T. Lancaster, **R. C. Williams**, F. L. Pratt, S. J. Blundell, D. Ceresoli, A. M. Barton and J. L. Manson. "Spin diffusion in the low-dimensional molecular quantum Heisenberg antiferromagnet $Cu(pyz)(NO_3)_2$ detected with implanted muons". *Phys. Rev. B*, **91**, 144417 (2015).

- L. Dos Santos *et al.* "Experimental and theoretical electron density analysis of copper pyrazine nitrate quasi-low-dimensional quantum magnets". *J. Am. Chem. Soc.*, **138**, 2280 (2016).

- J. Liu *et al.* "Antiferromagnetism in a family of $S = 1$ square lattice coordination polymers $NiX_2(pyz)_2$ (X = Cl, Br, I, NCS; pyz = pyrazine)". *Inorg. Chem.*, **55**, 3515 (2016).

Acknowledgements

Utmost thanks are due to my supervisor Tom Lancaster, who has been a constant source of inspiration, encouragement and insight throughout the entirety of this project. His endless humour, optimism and enthusiasm for physics have made these last few years a real pleasure.

My thanks must also go to Fan Xiao, who has been supremely patient when helping me solve problems both great and small during my time in Durham. In particular, I am grateful to him for sharing his expertise in the mysterious ways of the SQUID-Magnetometer.

Collaborators in Durham have contributed a great deal of numerical expertise, and I thank both Iowerth Thomas and Stewart Clark for all of their efforts performing DFT and dipole field calculations as part of this project. I am also grateful to Peter Hatton for his support of this project. Further afield, I consider myself very lucky to have worked alongside Stephen Blundell, Roberto de Renzi and Andrew Boothroyd, and to have benefited from their expansive joint knowledge of magnetism (and journal referees).

The majority of this work was carried out at the Swiss muon source SμS, Paul Scherrer Institut, Switzerland and the STFC ISIS Facility, Rutherford Appleton Laboratory, UK. I am grateful for the provision of beamtime at both facilities. Thanks are due to Alex Amato, Hubertus Luetkens and Christopher Baines at SμS, and Peter Baker and Francis Pratt at the ISIS facility for their superb experimental assistance. Extra thanks go to Francis, since I have made extensive use of his data analysis software, WiMDA.

None of this work would have been possible without the truly impressive work of those who grew the samples, and I am particularly grateful to Geetha Balakrishnan in Warwick and Prabhakaran in Oxford.

My time in Durham has been greatly enhanced by my friendships with many people. I'm very grateful to Clare Gussin, George Wells, Richard Rowan-Robinson, Ewan Hemingway, Kelly Johnson, Tom Frawley, Peter Byrne, Lara Small, David Hoyle, Ranga and Liam Stubbington for their friendship, scientific discussion, company on hills, bicycles and rock faces, and various combinations of the above. Thanks also go to my family, Alison, Howard and Matt, for all of their unwavering support.

Contents

1

Introduction

Modern condensed matter physics is perhaps best summarised by the title of Philip Anderson's famous article, "More is different" [1]. Over the second half of the 20th century, it became increasingly apparent that the behaviour of many-body systems is governed by collective phenomena that are unlikely to be predicted from a reductionist, ground-up approach. Spectacular demonstrations of this principle were provided by breakthrough solutions to problems such as (conventional) superconductivity and the quantum Hall effect. In fact, the behaviour of apparently quite different systems has been increasingly unified by the adoption of the language and strategies employed by low-energy quantum field theory [2]. In this approach, phases of matter comprising many interacting particles may be reduced in complexity greatly by considering their collective behaviour. Excitations may be regarded as particles known as *quasiparticles*, which arise from ground states (or 'vacua' in the nomenclature of field theory) characterised by their fundamental symmetries. An example of this

approach is the vastly successful Landau Fermi-liquid theory, which originated as a phenomenological description of interacting fermions but has since been shown to be consistent with the results of a full field theory treatment.

Since symmetry plays such a seminal role in this picture, it is perhaps not surprising that *phase transitions*, associated with the spontaneous breaking of a subset of systems' symmetries, are so profoundly significant in condensed matter physics. Different phases of matter correspond to dramatic rearrangements of the many-body ground state, and therefore it is to be expected that distinct, emergent excitations arise from the fundamentally different vacua on either side of a transition. Phase transitions are ubiquitous, and it transpires that the behaviour of systems in their vicinity, known as 'critical phenomena', may be understood and anticipated by neglecting the complexity of the microscopic interactions present, and reducing the problem to a small number of dimensionalities and symmetries. This beautiful hypothesis of *universality* allows transitions as seemingly disparate as the melting of a snowflake and destruction of the superconducting state to be commonly understood [3]. Furthermore, excitations known as *topological objects* arise quite naturally in such a picture, where symmetries break differently in different spatial regions [4, 5].

As one the most intensively researched field of condensed matter, magnetism continues to serve as a playground for both theoretical and experimental investigations of quantum many-body physics. Magnetism is an inherently collective phenomenon, driven by electron correlations arising due to Coulombic interactions [6, 7]. Advances in chemical synthesis provide ever more diverse and exotic testing grounds for theory, since compounds may be created that closely approximate idealised models and therefore proffer experimentally accessible ways of probing many-body phenomena. Besides temperature, externally controlled variables such as pressure or magnetic field may be tuned to drive *quantum* phase transitions, and potentially realise hitherto undiscovered phases of matter [8]. Here, quantum fluctuations resulting from the Heisenberg uncertainty principle are the driving force for the transition, rather than thermal fluctuations as in conventional phase transitions.

Transition metal oxides exhibit a vast array of magnetic phenomena as there is strong interplay between spin, orbital, charge and lattice degrees of freedom. In

addition, delicate balances between competing interactions, or frustration introduced by the underlying geometry of the lattice give rise to diverse and fascinating effects. The multifarious magnetic properties observed in transition metals are primarily due to the behaviour of their partially filled d orbitals; they feature numerous accessible valence states which can be magnetically active through both spin and orbital angular momenta. The relatively small spatial extent of $3d$ orbitals leads to narrow electronic bandwidths and the manifestation of correlation effects, whereas the inclusion of heavier elements, such as $5d$ osmium, means additional effects such as spin-orbit coupling may also influence the magnetic behaviour within materials [9, 10].

Recently, a tremendous quantity of research has focussed on high temperature superconductors and related compounds, where the interplay between multiple broken symmetry phases including magnetism and unconventional superconductivity is the topic of much debate [11]. This class of materials is exemplified by the prototypical cuprate superconductors, where antiferromagnetic parent compounds display Mott-like insulating states, yet the introduction of mobile charge carriers into the 2D CuO_2 layers via doping generates a rich and complex phase diagram. Experimental and theoretical studies of related compounds comprising layered structured transition metal oxides may help elucidate this problem [12], especially given the serendipitous nature of many discoveries in the history of science.

1.1   Layout of Thesis

This thesis is organised as follows:

Chapter 2:   The experimental technique of muon-spin spectroscopy (μSR) is introduced, which is the primary technique used throughout this thesis. Particular emphasis is placed on the underlying theory, practical experimental considerations and the derivation of idealised relaxation functions.

Chapter 3:   The results of a μSR study on four related osmate double perovskite compounds Sr_2BOsO_6 ($B = Co, Fe, Y, In$) are presented. In conjunction with AC susceptibility and neutron diffraction results, our μSR measurements identify complex

lattice-site specific dynamics in Sr_2CoOsO_6, arising due to weak inter-sublattice exchange coupling. The results of complementary density functional theory and dipole field calculations are used to aid interpretation of the muon results for Sr_2FeOsO_6. The possibility of incommensurate magnetic ordering is discussed for Sr_2InOsO_6 and Sr_2YOsO_6.

Chapter 4: The results of μSR measurements on the tetrahedral spin-chain oxide $CsCoO_2$ are presented. Dipole field simulations are used in conjunction with Bayesian analysis to demonstrate the consistency of the muon results with magnetic spin structures proposed on the basis of neutron scattering results.

Chapter 5: The results of an extensive μSR study of the layered cobaltate system $La_{2-x}Sr_xCoO_4$ are used to derive a revised magnetic phase diagram as a function of dopant concentration and temperature.

Chapter 6: Results are presented of the first transverse field muon-spin rotation measurements to be made within a skyrmion lattice phase. AC susceptibility measurements confirm the presence of the skyrmion lattice within the sample of Cu_2OSeO_3, and dipole field calculations are employed to support the claim that the μSR lineshape may be used to distinguish the skyrmion phase from those neighbouring it.

Chapter 7: The thesis is concluded and future avenues for research and development of the μSR technique are discussed.

Data presented in this thesis are available at http://dx.doi.org/10.15128/r1fj2362083.

2

The μSR Technique

This chapter shall introduce the technique of muon-spin relaxation (μSR), which is the primary experimental method used in this thesis. The fundamental principles of the technique are explained, including the phenomenon of spin precession and the asymmetric nature of muon decay into the detected positron. A brief account of the experimental procedure is provided, including the production of spin-polarised muons, the definition of the measured asymmetry $A(t)$ and how its time evolution may be studied in order to extract information regarding static and dynamic magnetic effects. A quantum mechanical treatment of bound muon fluorine states is presented, where the expected polarisation is analytically soluble. The field of molecular magnetism is introduced, which is an area where the technique has recently proved to be particularly powerful, and a miniature case study demonstrating some of the key experimental outcomes from zero field μSR is presented.

2.1 Principles of μSR

Two consecutive papers published within a single volume of *Physical Review* in 1957 confirmed Lee and Yang's hypothesis that parity is violated in interactions mediated by the weak force [13]. The first was the seminal paper by Wu *et al.*, where the asymmetric beta decay of spin-polarised ^{60}Co nuclei was confirmed [14]. In the second paper, Garwin, Lederman and Weinrich demonstrated that the angular distribution of positrons arising from the decay of positive muons is also asymmetric; the positron is emitted preferentially along the instantaneous direction of the muon's spin-polarisation [15]. This latter result may be considered to be the very first muon-spin rotation experiment [16], where spin-polarised muons were stopped in a target and subsequently precessed around a uniform externally applied magnetic field, while the distribution of decay positrons allowed the time-dependent spin-polarisation of the muon ensemble to be followed. The potential use of this phenomenon to infer information about spatial magnetic field distributions within materials was very quickly realised [17]. In fact, the original paper concluded with the remark "It seems possible that polarised positive ... muons will become a powerful tool for exploring magnetic fields in ... interatomic regions" [15]. Indeed, the authors were correct and in the following decades the field of muon-spin relaxation/resonance/resonance (collectively termed 'μSR') has developed continually into an ever more powerful and versatile tool for the study of magnetic behaviour in condensed matter systems.

Muon spectroscopy serves as a sensitive *local* probe of magnetism, where the time-dependent spin of a muon ensemble is the experimental observable. In this context, *relaxation* refers to the dephasing (loss of initial polarisation) of the ensemble via spatial or temporal field distributions. *Rotation* encompasses precession about an externally applied field which is modulated by any internal magnetic fields within the sample. These two cases will be introduced in greater detail later in the chapter. Finally, *resonance* implies the use of resonant radio frequency (RF) or microwave fields [18, 19], and will not be discussed further in this thesis.

A fortunate further consequence of parity violation is that the production of spin-polarised muons is relatively straightforward [20] (discussed in Sec. 2.2.1). Once

implanted in an experimental sample, these polarised muons are in an initial state that is as far from thermal equilibrium as is conceivable. This means that, in contrast to nuclear magnetic resonance (NMR), for example, the system under study does not need to be subjected to a RF or microwave pulse prior to measurement. Another major advantage of μSR is its versatility; measurements may be made in a wide range (including the absence) of external magnetic field strengths and orientations, for samples in any physical phase and containing any chemical elements whatsoever. This latter point is of particular benefit when compared to NMR where certain atomic nuclei must be present, and neutron scattering which often requires samples to be deuterated in order to minimize beam attenuation due to the large incoherent scattering cross section of hydrogen, and whose sensitivity is dependent on the scattering lengths of the particular chemical elements present.

2.1.1 Muon Properties

A muon is a second generation lepton, and is therefore an elementary particle with spin $S = 1/2$. A positive muon may be considered to be a heavy positron with $m_\mu = 105.7$ MeV $\approx 207 m_e$, although in some instances it is more useful to consider it as a light proton with $m_\mu \approx m_p/9$. Since muons possess both electrical charge and non-zero spin, they have an associated magnetic moment. For a current I circulating around an elementary vector area $d\boldsymbol{A}$, the magnetic moment is defined as $d\boldsymbol{\mu} = I d\boldsymbol{A}$.

As a first approximation to calculate the magnetic moment of a lepton, considering it to be a uniformly charged sphere (with total charge q and mass m) rotating about its own axis yields $\mu = qL/2m$, where L is the angular momentum of the sphere. This result illustrates a key concept: the magnetic moment is associated with angular momentum. It is convenient to quantify this relationship by defining the gyromagnetic ratio γ via

$$\boldsymbol{\mu} = \gamma \boldsymbol{L}. \tag{2.1}$$

For the classical rotating sphere, this predicts $\gamma = q/2m$, however in a lepton it is the intrinsic angular momentum of spin $\boldsymbol{S}$ which generates the magnetic moment, which has no true classical analogue. Nevertheless, this approximation is surprisingly successful and differs from the experimental result by only a constant of proportional-

	charge	spin	mass	moment	$\gamma/2\pi$ (MHz T^{-1})	lifetime (μs)
e	$\pm e$	$1/2$	m_e	$657\mu_\mathrm{p}$	28,000	$> 10^{40}$
μ	$\pm e$	$1/2$	$207m_\mathrm{e}$	$3.18\mu_\mathrm{p}$	135.5	2.197
p	$\pm e$	$1/2$	$1836m_\mathrm{e}$	μ_p	42.6	$> 10^{42}$

Table 2.1: A comparison of the properties of electrons, muons and protons. Data from Ref. [22].

ity: the g-factor. Dirac's relativistic theory of the electron predicts that g is exactly equal to 2, however, quantum electrodynamics introduces a series of terms of higher order in the fine structure constant α. For most purposes the g-factor of a muon may be taken as equal to that of the electron [21]. In conclusion, for a muon we have:

$$\boldsymbol{\mu} = \gamma_\mu \boldsymbol{S}, \tag{2.2a}$$

$$\gamma_\mu = g\frac{|e|}{2m_\mu}, \tag{2.2b}$$

where we have used $q = |e|$ for a positive muon.

Thus far $\boldsymbol{S}$ has simply represented the vector angular momentum associated with spin, however we will want to generalise to quantum mechanical spin operators $\hat{\boldsymbol{S}}^2|S, m_S\rangle = S(S+1)|S, m_S\rangle$ and $\hat{S}_z|S, m_S\rangle = m_S|S, m_S\rangle$. The associated eigenvalues $S(S + 1)$ and m_S are dimensionless, and so if a factor of $\hbar$ accompanies the $\boldsymbol{S}$ in Eq. 2.2a then it may be used in a quantum mechanical context too. We therefore obtain

$$\boldsymbol{\mu} = g\frac{e\hbar}{2m_\mu}\hat{\boldsymbol{S}}. \tag{2.3}$$

For the case of the electron $\boldsymbol{\mu} = -g\mu_\mathrm{B}\hat{\boldsymbol{S}}$, where $\mu_\mathrm{B} = |e|\hbar/2m_\mathrm{e} = 9.27 \times 10^{-24}$ J T^{-1} is the Bohr magneton.

2.1.2 Classical Precession

Classical electromagnetism tells us that a magnetic moment $\boldsymbol{\mu}$ in a magnetic field $\boldsymbol{B}$ has an energy given by $E = -\boldsymbol{\mu} \cdot \boldsymbol{B}$ and experiences a torque

$$\boldsymbol{G} = \boldsymbol{\mu} \times \boldsymbol{B}. \tag{2.4}$$

The energy is minimised when the dipole moment is aligned with the applied field, however the torque does not serve to orientate the dipole towards the field direction

since the moment is itself associated with angular momentum via Eq. 2.1. Therefore, upon substitution of Eq. 2.1 into Eq. 2.4, the rate of change of $\boldsymbol{\mu}$ is given by

$$\frac{\mathrm{d}\boldsymbol{\mu}}{\mathrm{d}t} = \gamma\boldsymbol{\mu} \times \boldsymbol{B}. \tag{2.5}$$

This equation describes Larmor *precession*; at any instant in time the incremental change in $\boldsymbol{\mu}$ is perpendicular to both $\boldsymbol{\mu}$ and $\boldsymbol{B}$, therefore the moment direction is never rotated towards the field but instead precesses. The Larmor precession angular frequency is given for a muon by

$$\omega_{\mathrm{L}} = \gamma_\mu B, \tag{2.6}$$

where $B = |\boldsymbol{B}|$ is the magnitude of the magnetic field at the muon site. It is important to note that the torque $\boldsymbol{G}$ is equal to zero when $\boldsymbol{\mu}$ and $\boldsymbol{B}$ are parallel, and hence precession only occurs when there is a field component perpendicular to the dipole moment.

This classical approach is illustrative, but is ultimately unsatisfactory when applied to the heavily quantised world of $S = 1/2$ muons. The observed values of spin angular momentum in any given direction may only assume the values $m_S = \pm 1/2$, and therefore the classical picture of a precessing dipole vector seems hopelessly inadequate. However, the same result will be obtained by a full quantum mechanical treatment in Sec. 2.4.1.

The phenomenon of spin precession in a magnetic field (with precession frequency proportional to the field strength B) implies that muons are able to be used to study magnetic field distributions once implanted within materials, provided it is possible to track the time-evolution of the polarisation. It transpires that the decay of an ensemble of muons into positrons allows their instantaneous spin direction to be deduced.

2.2   Experimental Procedure

2.2.1   Basic Principles

Muon production begins with high energy protons from a synchrotron, which collide with protons in a graphite target to produce stationary, spin-zero pions via $p + p \rightarrow$

$p + n + \pi^+$ [23, 24]. The pions subsequently decay into so-called *surface-muons* through the weak, two-body decay $\pi^+ \rightarrow \mu^+ + \nu_\mu$. The muon and neutrino must possess equal and opposite momenta, and since neutrinos always have spin and momentum anti-aligned [20] then so must the muon in order to conserve both linear and angular momentum. Hence, one has a means of producing a 100% spin-polarised beam of muons.

The beam is steered and focussed as necessary using dipole and quadrupole magnets, respectively, before being implanted into the study sample. The incident muons lose their energy to the sample (initially ≈ 4.1 MeV) by scattering, ionisation and electron capture/loss processes, before coming to rest in regions well separated from any radiation damage [25]. These interactions are all Coulombic in origin, and as such do not generate any loss of polarisation, and occur on the nanosecond scale, so that the initial polarisation of the stationary muons is still well-known. Samples are usually sealed in an envelope (of typical foil thickness 12.5 or 25 microns) which is subsequently mounted on a backing plate. Normally, silver is used for both the plate and the foil, since elemental silver is diamagnetic (i.e., has no electronic moment) and has only very small nuclear moments. Therefore, muons stopping outside of the sample should only contribute a time-independent background term to the asymmetry. For small or weakly magnetic samples this background contribution to the signal may be further reduced by employing the so-called *fly-past* arrangement, where the foil envelope is attached to the prongs of a silver fork, rather than a solid plate, so that muons that do not stop in the sample are removed from the experiment.

As shown in Table 2.1, a muon is unstable, and will undergo decay to a positron via the reaction pathway $\mu^+ \rightarrow e^+ + \nu_e + \overline{\nu}_\mu$ with an average lifetime of 2.2 μs. This decay is mediated by the weak force, and violates parity conservation; the resulting positron is emitted preferentially along the direction of the muon's polarisation [15]. For this three-body decay the positron's kinetic energy is not uniquely constrained, but instead follows the distribution function $p(\epsilon) = 2(3 - 2\epsilon)\epsilon^2$, where ϵ is the kinetic energy normalised with respect to the maximum energy $E_{\text{max}} = 53$ MeV [26]. The angular probability function for a positron to be emitted at an angle θ to the muon's instantaneous spin direction is given by $W(\epsilon, \theta) \propto 1 + a(\epsilon) \cos \theta$, where the asymmetry
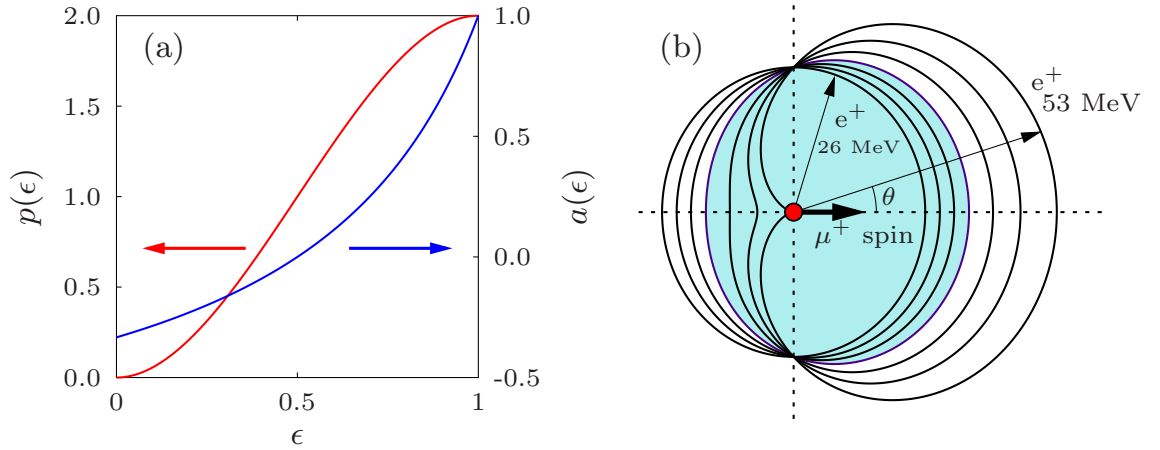
Figure 2.1: (a) The energy distribution $p(\epsilon)$ and asymmetry parameter $a(\epsilon)$ of the decay positron as functions of its normalised kinetic energy ϵ. (b) The angular probability distribution $W(\epsilon, \theta)$ shown for positrons emitted with kinetic energies between $E_{\max}/2$ and $E_{\max}$. The shaded area corresponds to the energy-averaged value of $\langle a \rangle = 1/3$.

parameter $a(\epsilon) = (2\epsilon - 1)/(3 - 2\epsilon)$ varies monotonically with the normalised positron energy ϵ up to $a = 1$. The energy distribution function and asymmetry parameter are plotted in Fig. 2.1(a). It may be seen that $a(\epsilon)$ is in fact negative for $\epsilon \leq 0.5$, but fortuitously production of these low energy positrons is not favoured by $p(\epsilon)$ and they are also less likely to penetrate far enough to reach the detectors. The angular distribution function $W(\epsilon, \theta)$ is shown in Fig. 2.1(b), where the distribution corresponding to the energy-averaged value of $a(\epsilon) = 1/3$ is highlighted.

Most emitted positrons are highly energetic, and readily penetrate the sample and any cryostat material before impinging on detectors comprising scintillators and photomultiplier tubes. Detectors are usually grouped to define 'forward' and 'backward' directions with respect to the muon's original momentum, and the measured quantity is the normalised *asymmetry function* $A(t)$ given by

$$A(t) = \frac{N_{\mathrm{B}}(t) - \alpha N_{\mathrm{F}}(t)}{N_{\mathrm{B}}(t) + \alpha N_{\mathrm{F}}(t)}, \tag{2.7}$$

where $N_{\mathrm{B,F}}$ are the backward and forward count histograms, respectively, and α is an experimental calibration constant accounting for detector efficiencies and solid angle discrepancies due to sample location with respect to the detectors. The asymmetry $A(t)$ is proportional to the spin-polarisation of the muon ensemble. A schematic of the experimental arrangement is shown in Fig. 2.2. The maximum observable
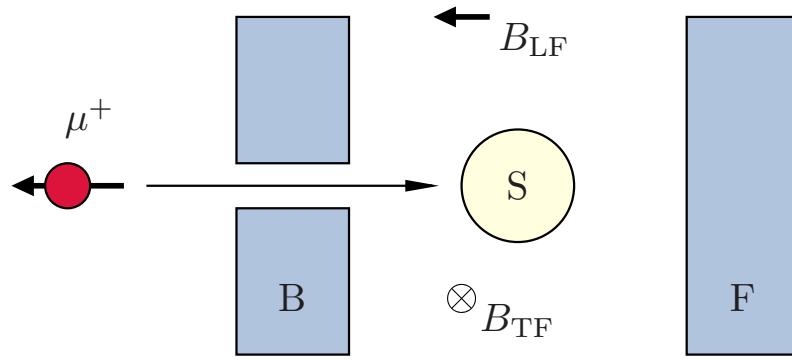
Figure 2.2: A schematic illustration of the experimental arrangement showing the sample S between the forward and backward detector groups (F and B, respectively). Also shown are the directions of externally applied magnetic fields for the TF and LF geometries, as defined in Sec. 2.4.3.

asymmetry is obtained by an appropriate integration over the energy-dependent probabilities of positron emission and detection, the asymmetry function $W(\epsilon, \theta)$ and the solid angle of the detector groupings.

2.2.2 Experimental Considerations

There are two main categories of muon source; *continuous* and *pulsed*, which are described briefly below.

- In a continuous source [such as the Swiss Muon Source (SμS) in Switzerland] single muons arrive intermittently and the experimental start time $t = 0$ coincides with the implantation of each muon in the sample. The clock stops when a decay positron is recorded, which constitutes a single *event*. This strategy relies upon the presence of only one muon at a time in the sample, since each positron detection needs to be unambiguously assigned to the decay of a particular muon. This constraint limits both the count-rate and low-frequency resolution of a continuous source, since the arrival of a further muon before the preceding muon's decay has been recorded invalidates the event associated with the detection of any positrons. As such, both the rate of incident muons and time window for positron detection must be limited, which in practice places an upper limit of around 10 μs on datasets.

- Pulsed muon sources (such as the ISIS synchrotron, UK) are able to reliably measure asymmetry data to much longer times, since muons arrive in intense pulses which are well-separated with respect to the muon lifetime. In this scenario the time t is defined relative to arrival of the pulse, which constrains the high-frequency resolution of the experiment due to the finite temporal width of the incident pulse (the full-width at half-maximum at ISIS is around 80 ns, with pulse frequency 50 Hz). High count rates are limited by the dead times of detectors (the minimum time required between the arrival of successive positrons for the individual events to be resolvable), which is mitigated by the use of many, small detectors arranged in groups. For example, the MuSR spectrometer at ISIS has 64 detectors compared to only 5 on the GPS instrument at SμS.

2.2.3   Time Window of μSR

One particular characteristic of the μSR technique which makes it either advantageous versus, or complementary to, other experimental probes of magnetism is the range of dynamical fluctuation rates to which it is sensitive. This so-called *dynamic range* is determined by the muon lifetime $\tau = 2.2$ μs and its gyromagnetic ratio $\gamma_\mu = 2\pi \times 135.5$ MHz T^{-1} (see Table 2.1). A lower limit on this range is set by the longest time window achievable at pulsed sources (e.g., ISIS) which is around 20–30 μs, corresponding to frequencies and relaxation rates of order 0.05 MHz and magnetic field strengths of about 0.04 mT [26]. This sensitivity to slow dynamics and low frequencies makes μSR well suited to the study of magnetic materials with very small ordered moment sizes, of minimum magnitudes of around $10^{-3}\mu_{\mathrm{B}}$ [27]. The highest time resolution available equates to magnetic fields of order 10 T (using the recently commissioned HAL-9500 spectrometer at SμS), which implies a high-frequency resolution of around 10 GHz, or time scales of 1 ns. It is important to note that this dynamic range comprising around seven orders of magnitude is not simultaneously achievable in a given experiment, but represents the absolute limits on the time scales probed depending on the properties of the sample and the choice of instrument and experimental arrangement utilised.

The dynamic range of μSR allows one to study the behaviour of magnetic fluctuations on a time scale distinct to that of neutron scattering. The slowest dynamics accessible to neutrons are those probed by inelastic scattering measurements, with a time scale of $\hbar/\Delta E \approx 10^{-11}$ s (where $\Delta E \approx 1$ meV is the energy scale of the resolution of the measurement). In contrast, magnetisation measurements provide a probe of dynamics ranging from around 1 kHz (1 μs, using AC susceptibility) to 10^{-4} Hz (remanent magnetisation studies on the scale of hours).

2.3 The Magnetic Field at the Muon Site

The total magnetic field at the muon stopping site is a vector sum of all contributing terms, which are briefly outlined below [26, 27].

- The externally applied field $\boldsymbol{B}_0$, the effect of which is described in Sec. 2.4.3.

- The dipole coupling $\boldsymbol{B}_{\mathrm{dip}}$ between the muon and localised electronic or nuclear magnetic moments. The dipole field within a sample may be calculated, as described in Sec. 4.4.1, by summation over magnetic moments within a Lorentz sphere. This strategy also leads to the consideration of two extra field contributions. These are: (i) the Lorentz field $\boldsymbol{B}_{\mathrm{L}}$ due to magnetic moments lying outside of the Lorentz sphere, and (ii) the demagnetising field $\boldsymbol{B}_{\mathrm{dem}}$ due to magnetisation induced at the surface of the sample.

- The contact hyperfine field $\boldsymbol{B}_{\mathrm{hyper}}$ due to direct spatial overlap of the muon wavefunction with any local electronic spin density. This contribution is discussed in more detail in Sec. 4.4.1. The magnitude of $\boldsymbol{B}_{\mathrm{hyper}}$ defines two categories of muon stopping sites. Firstly, *diamagnetic* sites have negligible hyperfine coupling, and the local magnetic field is predominantly dipolar. In contrast, considerable overlap between muon and electron wavefunctions may lead to the formation of a hydrogenic muon-electron bound state, termed *muonium* [23, 26]. The latter category is termed *paramagnetic* and is not relevant to the studies presented in this thesis.

In certain instances the following terms also need to be considered, however they are not relevant to the materials considered within this thesis.

- The transferred hyperfine field $\boldsymbol{B}_{\mathrm{trans}}$ due to the RKKY (Ruderman-Kittel-Kasuya-Yosida) interaction mediated by conduction electrons in metals [28–30].

- The diamagnetic field $\boldsymbol{B}_{\mathrm{dia}}$ which arises due to screening currents in superconductors.

2.4 Theory of μSR

In μSR experiments the observable quantity is the time evolution of the average muon-spin polarisation with respect to the axis of observation b:

$$D_b(t) = \langle \hat{\sigma}_b(t) \rangle = \mathrm{Tr}\{\hat{\rho} \cdot \hat{\sigma}_b(t)\}, \tag{2.8}$$

where $\hat{\rho}$ is the system's density operator [31] and $\hat{\sigma}_b(t) = \exp(\mathrm{i}\hat{\mathcal{H}}t/\hbar)\hat{\sigma}_b \exp(-\mathrm{i}\hat{\mathcal{H}}t/\hbar)$ is the time-dependent Pauli spin operator (expressed in the Heisenberg representation) [32]. In a longitudinal field (LF, see Sec. 2.4.3) experimental arrangement, which is also utilised in the zero field (ZF) case, both the initial beam polarisation and applied magnetic fields lie along $\hat{\boldsymbol{z}}$ so that $b = z$, and the entirely polarised initial state of the muon ensemble implies that

$$\hat{\rho} = \begin{pmatrix} 1 & 0 \\ 0 & 0 \end{pmatrix} = \frac{1}{2}(\hat{\mathrm{I}} + \hat{\sigma}_z), \tag{2.9}$$

where $\hat{\mathrm{I}}$ is the identity operator, and the basis $|\uparrow\rangle, |\downarrow\rangle$ with respect to the z-axis has been used. If the Hamiltonian $\hat{\mathcal{H}}$ is diagonalisable then $D_z(t)$ is exactly soluble, and hence (using $\mathrm{Tr}\{\hat{\sigma}_i\} = 0$) we find

$$D_z(t) = \langle \hat{\sigma}_z(t) \rangle = \frac{1}{2}\mathrm{Tr}\{\hat{\sigma}_z(t) \cdot \hat{\sigma}_z(t)\} = \frac{1}{2}\sum_{m,n} |\langle m|\hat{\sigma}_z|n\rangle|^2 \cos(\omega_{mn}t), \tag{2.10}$$

where $|n\rangle$ are the energy eigenstates of $\hat{\mathcal{H}}$ with eigenenergies $E_n = \hbar\omega_n$, and $\omega_{mn} = (E_m - E_n)/\hbar$.
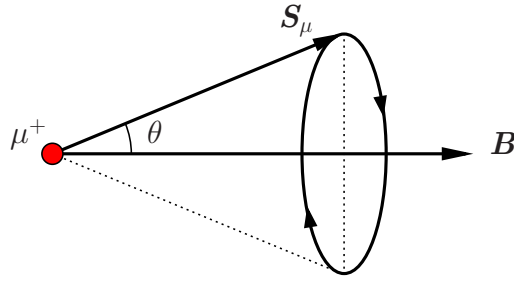
Figure 2.3: The semi-classical picture of a muon's spin precessing about the magnetic field direction.

2.4.1 Quantum Precession

Let us again consider a stationary muon residing in a static magnetic field $\boldsymbol{B}$. The Hamiltonian for this system is $\hat{\mathcal{H}} = -\boldsymbol{\mu} \cdot \boldsymbol{B} = -\gamma_\mu \hbar \hat{\boldsymbol{S}} \cdot \boldsymbol{B}$ (where use has been made of Eq. 2.3). If we choose $\boldsymbol{B} = B\hat{\boldsymbol{z}}$ then we may project the spin operator along the z-axis, giving $E = -\gamma_\mu \hbar m_S B$ with eigenkets $|\uparrow\rangle$ and $|\downarrow\rangle$ corresponding to the muon spin being aligned parallel or antiparallel to the z-axis, respectively. These kets will form our basis, and have eigenenergies of $\mp\gamma_\mu \hbar B/2$ corresponding to $m_S = \pm 1/2$.

More generally, following the approach in Ref. [33], the Hamiltonian describing a field orientated in the arbitrary direction given by (θ, ϕ) in spherical polar coordinates may be expressed as

$$\hat{\mathcal{H}} = \frac{-\gamma_\mu \hbar B}{2} \begin{pmatrix} \cos\theta & \sin\theta e^{-i\phi} \\ \sin\theta e^{i\phi} & -\cos\theta \end{pmatrix}, \tag{2.11}$$

which may be diagonalised to find eigenenergies $E_\pm = \pm\gamma_\mu \hbar B/2$ corresponding to eigenkets:

$$\begin{aligned} |+\rangle &= \sin\left(\frac{\theta}{2}\right) e^{-i\phi/2} |\uparrow\rangle - \cos\left(\frac{\theta}{2}\right) e^{+i\phi/2} |\downarrow\rangle, \\ |-\rangle &= \cos\left(\frac{\theta}{2}\right) e^{-i\phi/2} |\uparrow\rangle + \sin\left(\frac{\theta}{2}\right) e^{+i\phi/2} |\downarrow\rangle. \end{aligned} \tag{2.12}$$

Since there is no dependence on B, we note that these expressions represent a muon whose spin lies along an arbitrary axis given by (θ, ϕ). Substituting these eigenkets into Eq. 2.10 yields the static-field polarisation for the LF geometry

$$D_z(t) = \cos^2\theta + \sin^2\theta\cos\omega t, \tag{2.13}$$
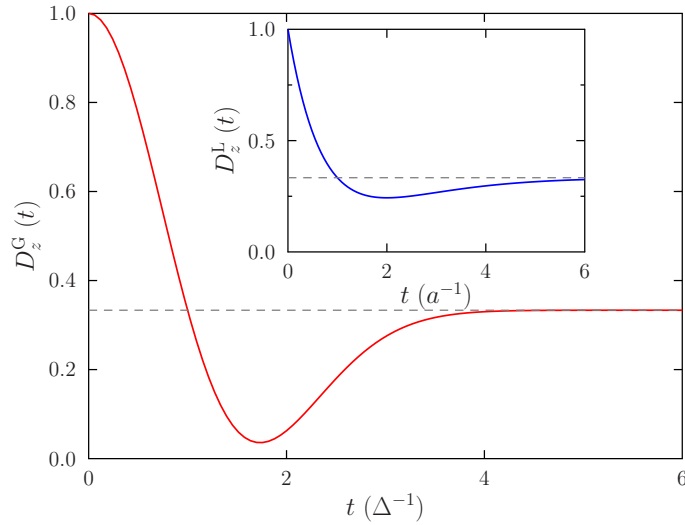
Figure 2.4: The *Kubo-Toyabe* relaxation function due to a Gaussian static-field PDF, Eq. 2.17 , showing the characteristic '1/3-tail' and Gaussian relaxation for small times. Inset shows the equivalent function arising from a Lorentzian PDF, Eq. 2.18.

where $\omega = \gamma_\mu B = \omega_{\mathrm{L}}$. This represents spin precession about the field $\boldsymbol{B}$ with the Larmor frequency as described in Sec. 2.1.2 (shown schematically in Fig. 2.3). In the case of a finely powdered sample, or randomly aligned paramagnets, the dipole field direction may take any direction with equal probability. Averaging over θ yields

$$D_z(t) = \frac{1}{3} + \frac{2}{3} \cos \omega t, \tag{2.14}$$

which demonstrates that, on average, 1/3 of a muon ensemble's spins can be expected to lie parallel to the field and so won't precess, whereas 2/3 will lie perpendicular and precess with frequency proportional to the local field at that site.

2.4.2   Field Distributions

We may extend the above discussion from uniquely valued magnetic fields to include static field distributions. One commonly encountered situation is that of randomly orientated magnetic moments, which occurs, for instance, for nuclear magnetic moments in paramagnet where the electronic moments are rapidly fluctuating outside of the time window of μSR. This scenario will generate a Gaussian distribution of dipole field strengths (according to the central limit theorem), where in zero applied field $\langle B_i \rangle = 0$. The normalised probability distribution function (PDF) $P(B_i)$ for

the ith component of $\boldsymbol{B}$ is given by

$$P^{\text{G}}(B_i) = \frac{\gamma_\mu}{\sqrt{2\pi}\Delta} \exp\left(-\frac{\gamma_\mu^2 B_i^2}{2\Delta^2}\right), \tag{2.15}$$

where $\Delta/\gamma_\mu = \langle(B - \langle B\rangle)^2\rangle^{1/2}$ is the field width (or second moment of the local field distribution) [23]. The corresponding PDF for the magnetic field strength $B = |\boldsymbol{B}|$ is therefore

$$P^{\text{G}}(B) = \frac{\gamma_\mu^3}{\Delta^3}\left(\frac{2}{\pi}\right)^{1/2} B^2 \exp\left(-\frac{\gamma_\mu^2 B^2}{2\Delta^2}\right). \tag{2.16}$$

Averaging Eq. 2.14 over field strengths following the Gaussian PDF yields

$$D_z^{\text{G}}(t) = \frac{1}{3} + \frac{2}{3}(1 - \Delta^2 t^2)e^{-\Delta^2 t^2/2}, \tag{2.17}$$

which is the famous *Kubo-Toyabe* (KT) relaxation function, plotted in Fig. 2.4. At long times this shows the characteristic '1/3 tail', and for short times is well approximated by the Gaussian relaxation $D_z(t) = \exp\left(-\Delta^2 t^2\right)$. The range of precession frequencies generated by the distribution of field strengths leads to *dephasing* of the muon ensemble's polarisation.

In contrast, it may be shown that in dilute spin systems the field PDF is well represented by a Lorentzian form [34], which (following the same prescription) generates the polarisation function

$$D_z^{\text{L}}(t) = \frac{1}{3} + \frac{2}{3}(1 - at)e^{-at}, \tag{2.18}$$

where the parameter a relates to the number density of spin moments [35]. This function decays more rapidly at small times due to the wider distribution of local fields within the material. A comparison of the relaxation functions due to static Gaussian and Lorentzian field distributions is provided in Fig. 2.4.

2.4.3 ZF, LF and TF

The application of a longitudinal magnetic field (LF) along the direction of initial polarisation ($\boldsymbol{B}_0 = B_0\hat{\boldsymbol{z}}$) is a very useful experimental technique. The above results derived for zero applied field (ZF) are in fact just the limiting case of the LF experiment, and following the same analysis approach using $B_z \to B_z - B_0$ with the
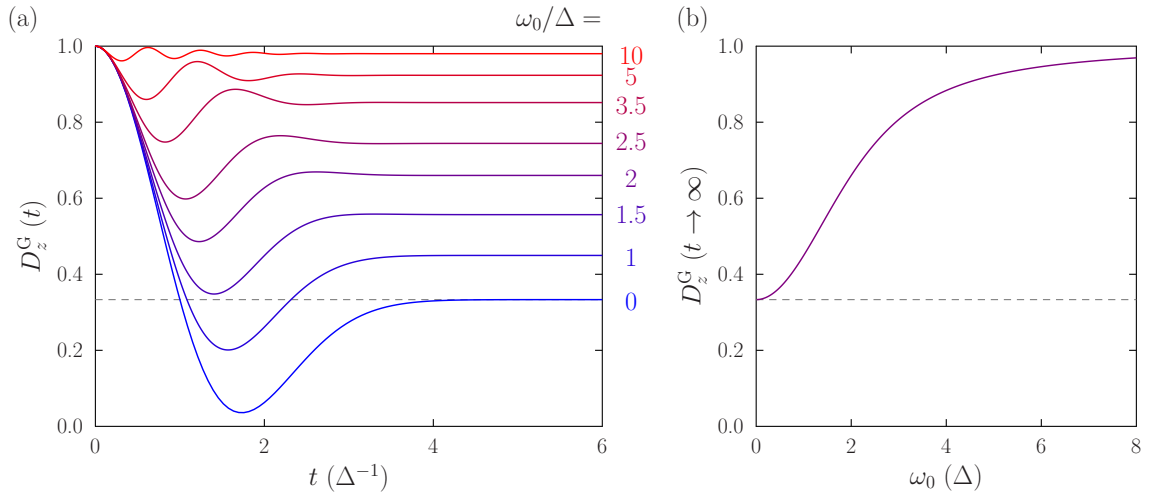
Figure 2.5: (a) The KT relaxation function in various applied longitudinal magnetic fields $B_0 = \omega_0/\gamma_\mu$, where the polarisation is given by Eq. 2.19. (b) The asymptotic value of the polarisation function at long times as a function of external field strength.

Gaussian distribution Eq. 2.15 yields

$$D_z^{\mathrm{G}}(t) = 1 - \left(\frac{2\Delta^2}{\omega_0^2}\right)\left[1 - e^{-\Delta^2 t^2/2}\cos(\omega_0 t)\right] + \left(\frac{2\Delta^4}{\omega_0^3}\right)\int_0^t e^{-\Delta^2\tau^2/2}\cos(\omega_0\tau)\,\mathrm{d}\tau,$$

$$(2.19)$$

where $\omega_0 = \gamma_\mu B_0$ [36]. This polarisation function is plotted in Fig. 2.5(a) for various field strengths, where a restoration of asymmetry is visible for applied fields. This effect is called *decoupling*, where the $1/3$ tail recovers to a higher value; $1/2$ when $\omega_0 \approx 1.25\Delta$ and complete repolarisation $[\lim_{t\to\infty}D(t) = D(0)]$ when $\omega_0 \gg \Delta$ [see 2.5(b)]. Physically, the applied field 'locks in' the spin direction of more muons, since a larger field component now lies parallel to the beam polarisation.

Alternatively, muon-spin *rotation* employs transverse fields (TF, see Fig. 2.2) in order to study internal field distributions. In this scenario, the time-dependence of the transverse component of the polarization will evolve as

$$D_x(t) = \int_0^\infty \mathrm{d}B\, p(B)\cos(\gamma_\mu B t + \phi), \qquad (2.20)$$

where $p(B)$ is the PDF of the total magnetic field strength (defined in Sec. 2.3) experienced at the muons stopping sites, and ϕ is a phase arising due to detector geometry. This technique has proved particularly useful in the study of the vortex lattice (VL) in the mixed phase of Type II superconductors, where it is possible to quantitatively extract the London penetration depth λ [23, 37–39]. The internal
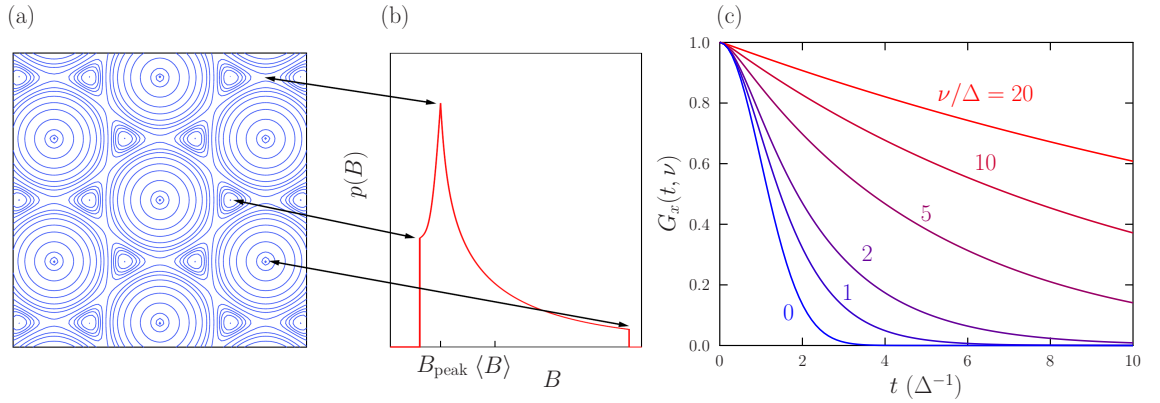
Figure 2.6: (a) A contour plot of magnetic field distribution of a hexagonal vortex (or Abrikosov) lattice arising in the mixed state of a Type II superconductor. (b) The corresponding magnetic field strength PDF $p(B)$, showing how distinctive features in the distribution map onto the spatial distribution in (a). (c) The dynamic TF envelope function Eq. 2.24, plotted for various muon hopping rates ν. Figs. (a) and (b) are adapted from Ref. [40].

magnetic field distribution for this state of affairs is shown in Fig. 2.6(b), where notable features in $p(B)$ such as the maximum, minimum and most probable fields intuitively map onto the contour plot of internal magnetic field strengths in Fig. 2.6(a). This experimental principle forms the basis of the TF μSR study of the skyrmion lattice phase of Cu_2OSeO_3 presented in Chap. 6.

Application of a strong TF $\boldsymbol{B}_0 = B_0\hat{\boldsymbol{x}}$, with $B_0 \gg \Delta/\gamma_\mu$, serves to orientate the total field $\boldsymbol{B} = \boldsymbol{B}_0 + \boldsymbol{B}_{\text{int}}$ almost parallel to $\hat{\boldsymbol{x}}$. Hence the magnitude of the total field is effectively $B_0 \pm |B_{\text{int}(x)}|$. Therefore, the polarisation (again for a Gaussian PDF) is given by

$$D_x^{\text{G}}(t) = e^{-\Delta^2 t^2/2}\cos(\omega_0 t) = G_x(t)\cos(\omega_0 t), \tag{2.21}$$

i.e., a single frequency oscillation modulated by a Gaussian relaxing envelope function $G_x(t)$ due to the narrow range of actual precession frequencies [36].

2.4.4 Dynamics

So far, spin relaxation due to static field distributions alone has been considered, but in reality distributions of fields also vary temporally. One approach to account for these dynamics is the strong collision approximation (SCA) [36, 41]. Here, one assumes that the local field may suddenly change direction after a time t with

probability distribution $\rho(t) \propto \exp(-\nu t)$ [collision lifetime $\tau \equiv (1/\nu)$], with the ensuing field entirely uncorrelated with the preceding field. For a Gaussian field distribution in the LF case each collision serves to 'reset' the KT function at the time t_i with new initial polarisation given by $D_z(t - t_i)$. The resulting relaxation function $D_z(t, \nu)$ may be obtained via Laplace transforms (for details see Ref. [36]) and is an envelope of many static functions. $D_z(t, \nu)$ is plotted in Fig. 2.7(a) for various collision rates ν. It may be shown [23] that in the fast fluctuation (narrowing) limit, $\nu/\Delta \geq 5$, the envelope transforms the early Gaussian shape of the KT function into an exponential decay

$$D_z(t, \nu) = \exp(-2\Delta^2 t/\nu) = \exp(-\lambda_z t), \tag{2.22}$$

where the longitudinal relaxation rate $\lambda_z = 2\Delta^2 \tau$. One key observation is *motional narrowing*; relaxation is *slower* for *faster* collision rates (larger ν) since precession barely rotates spins between each collision, and so asymmetry is not lost. This scenario is illustrated schematically in Fig. 2.7(b), where the term 'narrowing' derives from the narrower lineshape in the frequency domain. μSR is also able to probe very slow dynamic processes, since in the limit of slow fluctuations the $\frac{1}{3}$-tail will decay as $D_z(t, \nu) = \frac{1}{3} \exp(-\frac{2}{3}\nu t)$. This sensitivity to slow dynamics explains why perfect KT functions are rarely seen in real experimental data.

Another approach to modelling dynamics is to treat local field modulations via a Gaussian-Markov process, where fluctuating magnetic fields follow an exponential auto-correlation function $\langle B_i(t + \tau) B_i(t) \rangle \propto e^{-\nu\tau}$. It may be shown [42] that in the LF case the relaxation function in the narrowing limit $\nu \gg \Delta$ is given by

$$D_z(t, \nu) = \exp\left(-\frac{2\Delta^2 \nu t}{\omega_0^2 + \nu^2}\right). \tag{2.23}$$

Typically 'fast' collision frequencies ν are much larger than ω_0 for applied fields, and so this relaxation response is only weakly dependent on B_0. Repolarisation in this dynamic regime requires an external field of magnitude $\gamma_\mu B_0 \approx \nu$, in marked contrast to the effect of static field distributions considered in Sec. 2.4.3, where $\gamma_\mu B_0 \approx \Delta$ is sufficient [Fig. 2.5(b)]. Therefore, the application of a longitudinal magnetic field serves as a sensitive method to distinguish between static and dynamic causes of
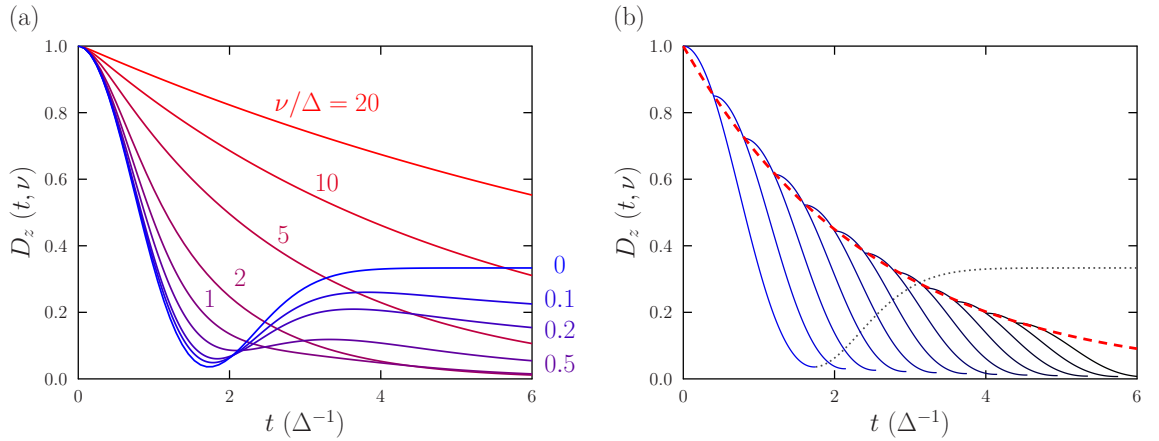
Figure 2.7: (a) The dynamic ZF relaxation function for a Gaussian distribution of fields $D_z(t, \nu)$, plotted for various collision rates ν. The static KT function is recovered for $\nu \to 0$, as expected, and motional narrowing is evident in the fast fluctuation regime (large ν) where the relaxation function is given by Eq. 2.22. (b) A schematic view of the SCA in the fast fluctuation regime, where the KT relaxation function 'resets' after a time $\tau = 1/\nu$, resulting in an exponentially decaying envelope.

relaxation. In the ZF limit ($\omega_0 \to 0$) Eq. 2.23 reduces straightforwardly to Eq. 2.22, as expected.

In the TF geometry this treatment yields the Abragam formula for relaxation [27, 43]

$$D_x(t, \nu) = \exp\left[-\frac{\Delta^2}{\nu^2}(\nu t - 1 + e^{-\nu t})\right]\cos(\omega_0 t) = G_x(t, \nu)\cos(\omega_0 t), \qquad (2.24)$$

where the decaying envelope function $G_x(t, \nu)$ is plotted for various hopping rates ν in Fig. 2.6(c). In the slow fluctuation limit Eq. 2.24 simply reduces to the Gaussian form of Eq. 2.21, but instead results in an exponential decay $G_x(t, \nu) = \exp(-\Delta^2 t/\nu)$ in the fast fluctuation limit, where motional narrowing is again apparent.

2.5 Muon-Fluorine Entangled States

Ordinarily an implanted muon may be viewed as a magnetic dipole which interacts with the local magnetic field through the Hamiltonian $\hat{\mathcal{H}} = -\boldsymbol{\mu} \cdot \boldsymbol{B}$. In this approach (the local magnetic field approximation) all of the muon's interactions with local spin centres are contained within the mean field $\boldsymbol{B}$. In certain circumstances the muon is dipole coupled to very few spin centres, and the quantum mechanical nature of the
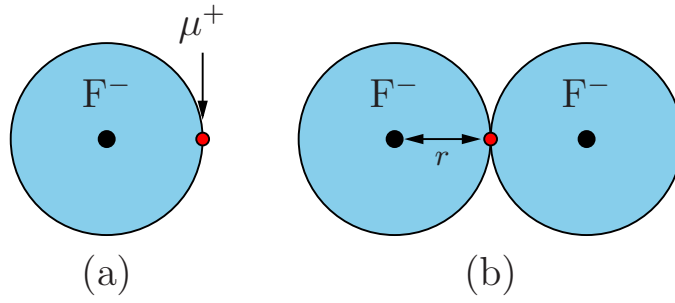
Figure 2.8: A schematic of the structure of the (a) Fμ and (b) FμF molecular complexes.

interactions cannot be neglected. A common situation where this is the case is when muons are implanted in materials containing fluorine, due to two of its properties:

- fluorine is the most electronegative element. This means that it will create a region of very high electron density which in turn attracts the positively charged μ^+.

- fluorine exists as one isotope only, ^{19}F, which has nuclear spin $I = 1/2$. Consequently all muon-fluorine interactions are identical and the resultant effects are not diluted.

In this situation, muons occupying diamagnetic sites dipole couple to fluorine nuclei (there is negligible spatial overlap between muon and nuclear wavefunctions, and therefore no hyperfine coupling). In analogy to classical electromagnetism, dipole-dipole coupling within a system of spins $\boldsymbol{S}_i$ (with gyromagnetic ratios γ_i) may be described through the Hamiltonian

$$\hat{\mathcal{H}} = \sum_{i<j} \frac{\mu_0 \gamma_i \gamma_j \hbar^2}{4\pi |\boldsymbol{r}|^3} [\hat{\boldsymbol{S}}_i \cdot \hat{\boldsymbol{S}}_j - 3(\hat{\boldsymbol{S}}_i \cdot \hat{\boldsymbol{r}})(\hat{\boldsymbol{S}}_j \cdot \hat{\boldsymbol{r}})] \ , \tag{2.25}$$

where $\hat{\boldsymbol{r}}$ is the unit vector connecting spin sites i and j, with separation $|\boldsymbol{r}|$. Extending the formulation of Eq. 2.10 to include multiple interacting spins, the longitudinal polarisation is given by

$$D_z(t) = \frac{1}{N} \left\langle \sum_{m,n} |\langle m|\hat{\sigma}_q|n\rangle|^2 \cos(\omega_{mn}t) \right\rangle_q , \tag{2.26}$$

where $N = \prod_i (2S_i + 1)$ normalises over possible spin permutations and $|m\rangle$ are the energy eigenstates of the Hamiltonian Eq. 2.25 [32]. For a powdered sample $\langle \ \rangle_q$

$|2\rangle = \frac{1}{\sqrt{2}} (|\uparrow\downarrow\rangle + |\downarrow\uparrow\rangle)$ $M = 0$ $E_2 = A$

$|1\rangle = \frac{1}{\sqrt{2}} (|\uparrow\downarrow\rangle - |\downarrow\uparrow\rangle)$ 0 $E_1 = 0$

$|0\rangle = |\uparrow\uparrow\rangle, |\downarrow\downarrow\rangle$ ± 1 $E_0 = -\frac{A}{2}$
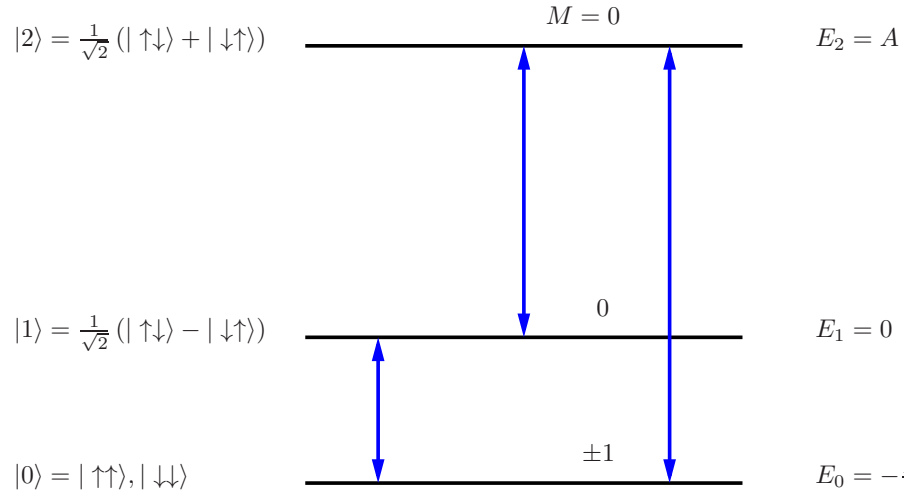
Figure 2.9: Energy levels of dipole coupled μF system, with arrows indicating transitions corresponding to observed oscillation frequencies.

signifies a geometrically weighted average over possible orientations, which may be summarised for the LF geometry as $q = z$ contributes $1/3$ while $q = x$ contributes $2/3$.

2.5.1   Muon Coupling with a Single Fluorine Nucleus

The simplest interaction to consider is that between a muon and a single fluorine nucleus. Choosing the vector linking the two spins, $\boldsymbol{r}$, to be along the z-axis, then projecting out the spin vectors in the second term of Eq. 2.25 yields the Hamiltonian

$$\hat{\mathcal{H}} = A \left(\hat{\boldsymbol{I}} \cdot \hat{\boldsymbol{S}} - 3\hat{I}_z\hat{S}_z \right), \tag{2.27}$$

where $A = (\mu_0 \gamma_i \gamma_j \hbar^2)/(4\pi|\boldsymbol{r}|^3)$ and $\hat{\boldsymbol{I}}$ and $\hat{\boldsymbol{S}}$ relate to the fluorine's nuclear moment and the muon spin, respectively. To proceed we choose a basis $\{|\chi_i\rangle\}$ for the two spins:

$$|\uparrow\uparrow\rangle, \ |\downarrow\downarrow\rangle, \ |\uparrow\downarrow\rangle, \ |\downarrow\uparrow\rangle, \tag{2.28}$$

where the first (second) arrow represents the z-component of the fluorine nucleus (muon) spin. Using the raising and lowering operators $\hat{L}_\pm \equiv \hat{L}_x \pm i\hat{L}_y$ [33], the Hamiltonian may be rewritten

$$\hat{\mathcal{H}} = A \left[\frac{1}{2}(\hat{I}_+\hat{S}_- + \hat{I}_-\hat{S}_+) - 2\hat{I}_z\hat{S}_z \right], \tag{2.29}$$

where operators relating to $\hat{\boldsymbol{I}}$ and $\hat{\boldsymbol{S}}$ act upon their relevant spin only, leaving the other spin unchanged. The Hamiltonian can then be expressed as a matrix in our choice of basis, since $\{|\chi_i\rangle\}$ are eigenkets of all of the operators present in $\hat{\mathcal{H}}$, using $\hat{\mathcal{H}}_{ij} = \langle\chi_i|\hat{\mathcal{H}}|\chi_j\rangle$ to give

$$\hat{\mathcal{H}}_{ij} = \frac{A}{2}\begin{pmatrix} -1 & 0 & 0 & 0 \\ 0 & 1 & 1 & 0 \\ 0 & 1 & 1 & 0 \\ 0 & 0 & 0 & -1 \end{pmatrix}. \tag{2.30}$$

Diagonalisation yields the eigenvectors $|n\rangle$ and corresponding eigenenergies E_n of the system, displayed in Fig. 2.9. We are now equipped with the eigenkets to insert into Eq. 2.26, together with the energies that will supply the mixing frequencies ω_{mn}.

The Pauli spin operator $\hat{\sigma}_q$ in Eq. 2.26 acts upon the muon spin only, and so the matrix elements are evaluated for $q = x$ and $q = z$ by expanding the energy eigenkets $|n\rangle$ in terms of the spin basis $|\chi_i\rangle$. The mixing frequencies arise from the fact that the spin state of the muon is well defined by its polarisation upon implantation, however this state does not correspond to an eigenket of the entangled muon and ^{19}F nucleus Hamiltonian.

The matrix element calculations are fairly laborious and are not displayed here, although computation may be reduced by using the Hermitian nature of the Pauli spin matrices to note that $\langle m|\hat{\sigma}_q|n\rangle = \langle n|\hat{\sigma}_q|m\rangle$. The application of selection rules also reduces the number of $\{mn\}$ combinations under consideration. They are: $\Delta M = 0$ for $q = z$ and $\Delta M = \pm 1$ for $q = x$, where $M = m_S^\mu + m_S^F$ is the total z-component of the spins [32].

The outcome (including appropriate powder average weighting) is

$$D_z(t) = \frac{1}{6}\left[1 + 2\cos\left(\frac{A}{2\hbar}t\right) + \cos\left(\frac{A}{\hbar}t\right) + 2\cos\left(\frac{3A}{2\hbar}t\right)\right], \tag{2.31}$$

which contains three oscillation frequencies depending solely upon the $\mu-^{19}$F separation r and known constants. The transitions with energies $E_{mn} = \hbar\omega_{mn}$ corresponding to these observed frequencies are illustrated in Fig. 2.9.

$|3\rangle = \frac{1}{(6+2\sqrt{3})^{1/2}} \left[|\uparrow\uparrow\downarrow\rangle + (1+\sqrt{3})|\uparrow\downarrow\uparrow\rangle + |\downarrow\uparrow\uparrow\rangle \right]$ $M = 1/2$ $E_3 = A\left(\frac{1+\sqrt{3}}{2}\right)$

$|2\rangle = \frac{1}{\sqrt{2}} \left(|\uparrow\uparrow\downarrow\rangle - |\downarrow\uparrow\uparrow\rangle \right)$ $1/2$ $E_2 = 0$

$|1\rangle = \frac{1}{(6-2\sqrt{3})^{1/2}} \left[|\uparrow\uparrow\downarrow\rangle + (1-\sqrt{3})|\uparrow\downarrow\uparrow\rangle + |\downarrow\uparrow\uparrow\rangle \right]$ $1/2$ $E_1 = A\left(\frac{1-\sqrt{3}}{2}\right)$

$|0\rangle = |\uparrow\uparrow\uparrow\rangle$ $3/2$ $E_0 = -A$
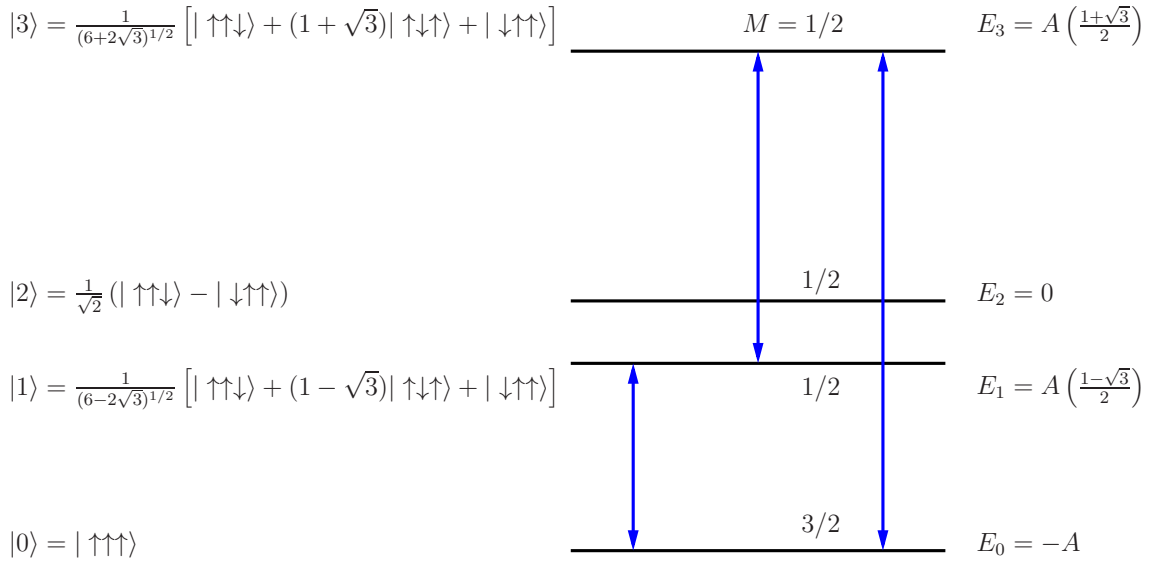
Figure 2.10: Energy levels and observed transitions for linear FμF system. Each energy level is doubly degenerate; the degenerate state may be obtained by reversing all of the spins in the shown expression for $|n\rangle$, and changing the sign of M.

2.5.2 Muon Coupling with Two Fluorine Nuclei

A more common occurrence is the case when the implanted muon interacts strongly with two F$^-$ ions and forms an FμF complex which may be treated as an exotic molecule-in-a-crystal defect [44]. In the simplest linear arrangement, this complex consists of two fluorine ions with nuclei separated by approximately two ionic radii, with the muon situated midway between the two (Fig. 2.8). The host material may undergo significant structural distortions to achieve this geometry, although in some instances the arrangement forms a crooked non-linear shape [45].

As a first approximation it is sufficient to consider only interactions between the muon and the two F nuclei, justified by the r^{-3} dependence of A which, together with $\gamma_\mu \sim 3\gamma_F$, implies that $A_{F-F} \ll A_{\mu-F}$. Proceeding as outlined in the previous section, one may find the eigenstates and their corresponding eigenenergies, which are displayed in Fig. 2.10. These eigenstates are then inserted into Eq. 2.26 to obtain
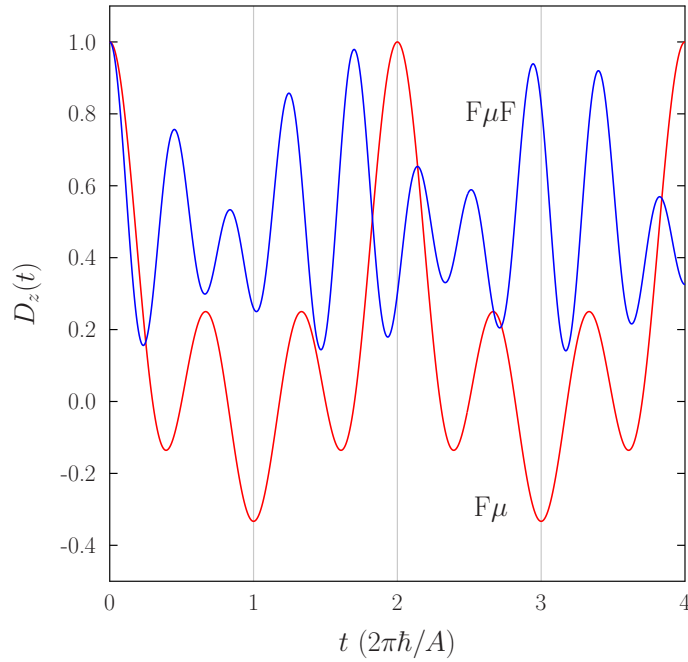
Figure 2.11: A comparison of $D_z(t)$ for $F\mu$ and $F\mu F$ (Eqs. 2.31 and 2.32, respectively), with $r_{\mu-F}$ and hence A identical for both cases.

the resulting polarisation [46]:

$$D_z(t) = \frac{1}{6}\left\{3 + \cos\left[\sqrt{3}\frac{At}{\hbar}\right] + \left(1 - \frac{1}{\sqrt{3}}\right)\cos\left[\left(\frac{3-\sqrt{3}}{2}\right)\frac{At}{\hbar}\right]\right.$$
$$\left. + \left(1 + \frac{1}{\sqrt{3}}\right)\cos\left[\left(\frac{3+\sqrt{3}}{2}\right)\frac{At}{\hbar}\right]\right\}, \quad (2.32)$$

where, once again, the oscillatory frequencies depend on r alone. Using the approximate ionic radius of $^{19}F^-$, so that $r = 1.2$ Å, then the frequency time scale is $\omega = A/\hbar = 1.3$ μs^{-1}, which is readily observable in a typical μSR experiment.

$D_z(t)$ is plotted in Fig. 2.11 for both the $F\mu$ and $F\mu F$ complexes. The calculation of the $\mu-F$ separation distance is a useful device to help identify the muon stopping sited within the unit cell of a material containing fluorine [45], and identifying the level of distortion of the crystal structure due to the implantation of the muon [44]. This information may then be valuable in the analysis of any muon spectra measured in the magnetically ordered state.

2.6 Molecular Magnetism and a μSR Study of CuF$_2$(pyz)

Following the introduction to the basic theoretical principles underlying the μSR technique and idealised polarisation functions, a short case study shall be presented illustrating how these results are applied in practice. The results of μSR measurements made on the molecular magnet CuF$_2$(pyz) will be used to demonstrate how electronic and nuclear magnetic effects may be identified in actual datasets, where idealised models must be adapted to account for 'real world' complications. This shall be useful in highlighting data analysis themes and strategies that will recur throughout the results chapters of this thesis. Most data analysis within this thesis was performed using the WiMDA data analysis programme [47], written by Francis Pratt.

2.6.1 Molecular Magnets

Molecular magnets, comprising spin centres (typically transition metal ions) linked via superexchange pathways mediated by ligands, have shown great applicability in producing highly tunable magnetic structures [48, 49]. The wide variety of architectures achievable through selections of ligands, spin centres and intercalating molecules permits vast numbers of potential systems, and a large level of control over geometries and exchange interaction strengths. Through the manipulation of these coupling strengths, it is possible to synthesise materials displaying quasi-low-dimensional magnetic behaviour; where certain exchange pathways dominate to an extent where the effective dimensionality is reduced. Much research (both experimental and theoretical) has been devoted to further understanding the behaviour of these reduced dimensionality systems [50, 51]. Chemical methods have been demonstrated which allow dimensionality selection between a quasi-one dimensional (Q1D) and quasi-two dimensional (Q2D) system while preserving nearest-neighbour coupling strengths [52] and the application of pressure has also been utilised to change the effective dimensionality of such systems [53]

A Q1D system may be considered to be a linear chain of strongly interacting

spin centres, whereas a system composed of a layered, planar lattice arrangement of spins would be Q2D, where inter-chain (plane) exchange strengths are weak. In both instances the Heisenberg Hamiltonian for isotropic spins is given by

$$\hat{\mathcal{H}} = J \sum_{\langle ij \rangle} \hat{\boldsymbol{S}}_i \cdot \hat{\boldsymbol{S}}_j + J' \sum_{\langle ij' \rangle} \hat{\boldsymbol{S}}_i \cdot \hat{\boldsymbol{S}}_{j'}, \tag{2.33}$$

where i and j label spins within the same chain (plane), j' indicates the spin centres located on the four (two) adjacent chains (planes) and the sums are taken over unique nearest-neighbours [54] (here, the single-J convention has been used). The intra-chain (plane) exchange coupling J alone cannot lead to long range magnetic order (LRO) for non-zero temperature; the Mermin-Wagner theorem dictates that $\langle S_z \rangle = 0$ above $T = 0$ for isotropic spins in 1D and 2D [55]. However, the presence of the weak inter-chain (plane) exchange interaction J' permits the formation of LRO, albeit at a reduced Néel (transition) temperature T_N relative to the 3D mean-field result [7]. The value of the ratio T_N/J is a useful indicator of the extent to which Q1D (Q2D) has been accomplished, and hence a measure of dimensionality.

An advantage of molecular magnet systems over transition metal oxides is that dominant exchange interaction magnitudes are comparable to Zeeman energies for experimentally accessible magnetic fields, i.e., $J \approx g\mu_\mathrm{B}B$ where B is of order Tesla. This allows magnetic field driven effects to be directly observed, and permits the experimental determination of J via pulsed-field and magnetic susceptibility measurements. However, this implies that for highly anisotropic materials J' is necessarily very small and difficult to probe directly. Quantum Monte Carlo simulations have yielded empirical relations between J' and T_N, so that an experimental determination of the ordering temperature allows one to quantitatively assess the degree to which low-dimensionality has been achieved.

Muon spectroscopy has proved to be uniquely successful in the study of such molecular magnet systems [56,57]. Ordinarily, phase transitions may also detected through discontinuities in specific heat measurements due to abrupt entropic changes at the transition temperature. However, non-zero correlation lengths in the disordered $T > T_\mathrm{N}$ state of Q2D systems serve to reduce the entropy change upon ordering, and hence decrease the size of any specific-heat anomalies [58–60]. Neutron studies

of these organic molecular magnets provide further insight into their magnetic structure, however, as discussed in Sec. 2.1, the sample must first be deuterated. This demanding requirement may also be undesirable since it has been demonstrated that the strength of superexchange pathways involving hydrogen-bonds is influenced by isotopic substitution [61].

2.6.2 CuF$_2$(pyz)

The isostructural series CuX_2(pyz), where $X = $ Br, Cl, F, share a Q2D rectangular lattice structure composed of $S = 1/2$ Heisenberg Cu^{2+} ions. The Cu^{2+} ions are linked into chains by bridging pyrazine molecules, which are themselves cross-linked via dihalide bridges to create 2D layers containing the rectangular magnetic lattice of Cu^{2+} ions. Magnetic superexchange pathways are therefore provided by pyrazine and dihalide bridges, and interlayer magnetic coupling is very small. Susceptibility measurements on the $X = $ Br, Cl compounds have provided estimates of the in-plane exchange strengths [62]. Previous μSR investigations have determined transition temperatures for these two compounds [63], yielding low values of T_{N}/J and J'/J for these materials which suggest that they may in fact be approximated as Q1D chains, although not particularly well isolated.

This coordination polymer family has recently been extended to include the $X = $ F system, CuF$_2$(pyz) [64], and ZF μSR data measured in a sorption cryostat using the MuSR instrument at ISIS are shown in Fig. 2.12(a). Samples were grown by J. A. Schlueter. At low temperatures oscillations are visible in the asymmetry data for $t \lesssim 0.1$ μs, corresponding to coherent Larmor precession of the muon ensemble in quasi-static magnetic fields (Sec. 2.4.1). This is indicative of long-range magnetic order of the Cu^{2+} ions, and also implies the existence of two magnetically inequivalent muon stopping sites. The temperature-dependence of the two resolvable precession frequencies are shown in Fig. 2.12(b), where their relative magnitudes were held in fixed proportion. Fitted relaxation rates increase as T approaches T_{N} as correlation times diverge (in the fast fluctuation limit $\lambda \propto \langle B^2 \rangle \tau$, as discussed in Sec. 2.4.4). This effect means that frequencies cannot be reliably fitted close to T_{N}. Instead, data were binned heavily (in order to smooth over the oscillations) and fitted to a
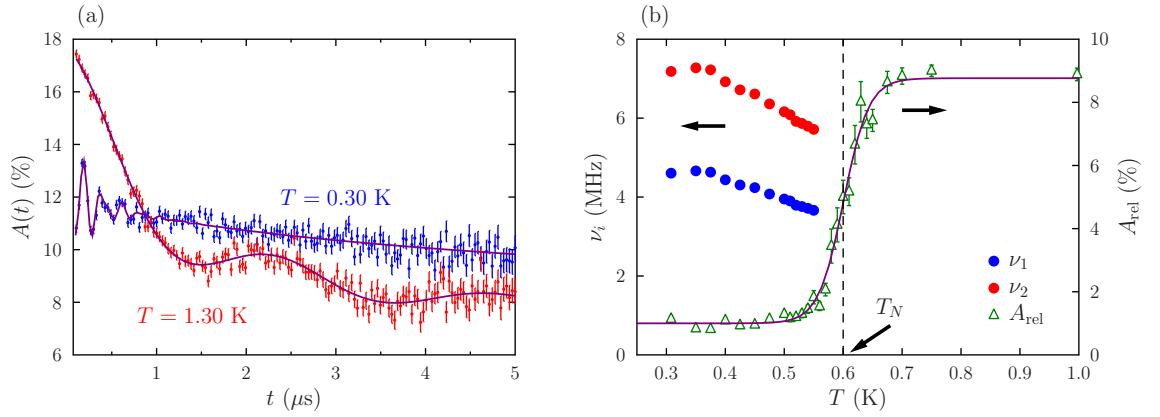
Figure 2.12: (a) Asymmetry data for CuF$_2$(pyz). Spontaneous oscillations are visible below T_N, where the rise in the non-relaxing baseline (relative to higher temperature data) corresponds to the '1/3-tail'. Above the ordering temperature low-frequency oscillations characteristic of the Fμ bound state may be seen, with solid line a fit to Eq. 2.34. (b) Temperature-dependence of the precession frequencies, and dramatic change in relaxing asymmetry A_{rel} used to determine $T_N = 0.60(2)$ K.

purely decaying asymmetry relaxation function. An abrupt change is visible in the relaxing amplitude A_{rel}, as shown in Fig. 2.12(b), which allowed $T_N = 0.60(2)$ K to be extracted. This step change in relaxing amplitude corresponds to 'lost' asymmetry within the ordered state, where large, static or slowly fluctuating internal magnetic fields lead to rapid precession outside of the instrument's time window (Sec. 2.2.3).

Well above T_N the characteristic oscillations of muon-fluorine entangled states were clearly visible [see Fig. 2.12(a)]. The $T = 1.3$ K data were found to best described by the oscillations characteristic of the bound state of a μ^+ and a single F$^-$ ion, and were therefore fitted to

$$A(t) = A_{\mathrm{F}\mu}D_z(t)e^{-(\lambda_{\mathrm{F}\mu}t)} + A_{\mathrm{G}}e^{-(\sigma t)^2} + A_{\mathrm{bg}}e^{-\lambda_{\mathrm{bg}}t}, \tag{2.34}$$

where $D_z(t)$ is the polarization function given by Eq. 2.31, with additional phenomenological broadening included using an exponentially decaying envelope. The Gaussian term serves as an approximation to the KT function, which is commonly observed due to nuclear dipole moments as discussed in Sec. 2.4.2. The fitted value of $\omega = A/\hbar = 1.74(2)$ μs^{-1} corresponds to a muon-fluorine separation of $r_{\mathrm{F}\mu} = 1.09$ Å. This value represents a time-averaged bond length, since the frequencies of vibrational modes exceed those accessible by μSR.

3

Muon-Spin Relaxation Study of the Double Perovskite Compounds Sr_2BOsO_6 $(B = \mathrm{Co, Fe, Y, In})$

This chapter shall present the results of zero-field muon-spin relaxation (ZF μSR) measurements made on the double perovskite materials Sr_2BOsO_6 $(B = \mathrm{Co, Fe, Y, In})$.

The μSR results for the compound Sr_2CoOsO_6 complement those of neutron powder diffraction and AC susceptibility measurements and help reveal exotic lattice-site-specific spin dynamics and ordering within this system. Here, two antiferromagnetic phases are encountered upon cooling. Firstly, upon cooling below $T_{N1} = 108$ K, one encounters a phase in which the averaged components of dynamically fluctuating (partially frozen) Co and Os spins establish long range antiferromagnetic order within the ab-plane. Below a secondary, lower transition temperature $T_{N2} = 67$ K, Co

moments freeze entirely to assume a canted noncollinear antiferromagnetic spin arrangement, while the behaviour of Os moments remains unchanged. Finally, below around 5 K the Os moments freeze into a randomly canted state, reminiscent of a spin glass.

Spontaneous muon-spin precession indicative of quasistatic long range magnetic ordering is observed in Sr_2FeOsO_6 within the AF1 antiferromagnetic phase for temperatures below $T_N = 135(2)$ K. Upon cooling below $T_2 \approx 67$ K the oscillations cease to be resolvable owing to the coexistence of the AF1 and AF2 phases, which leads to a broader range of internal magnetic fields. The results of density functional calculations are discussed that identify a candidate muon stopping site within the unit cell, which complementary dipole field simulations show to be consistent with the proposed magnetic structure. The possibility of incommensurate magnetic ordering is discussed for temperatures below $T_N = 53$ K and 25 K for the frustrated quasi-face-centred-cubic systems Sr_2YOsO_6 and Sr_2InOsO_6, respectively.

This chapter is based on work published in Refs. [65] and [66].

3.1 Introduction

Compounds exhibiting a perovskite structure are among the most intensively studied materials in condensed matter physics. The ABO_3 structure comprises corner-sharing BO_6 octahedra and a large alkali, rare earth or alkali earth metal cation A. The complex interplay between spin, orbital, charge and lattice degrees of freedom leads to a rich variety of physical phenomena including multiferroicity [67–69], superconductivity [70] and topological insulators [71]. Further scope for tunability and the engineering of magnetic properties is provided by partial cation substitution, including the realisation of the ordered double perovskite (DP) structure $A_2BB'O_6$, with interpenetrating quasi-face-centred-cubic (fcc) sublattices [72].

In magnetic systems, geometric frustration arises when the lattice geometry precludes the simultaneous satisfaction of competing spin interactions. The prototypical building block of such frustration comprises three Ising spins decorating the points of a triangle, with antiferromagnetic (AFM) exchange interactions between all three.
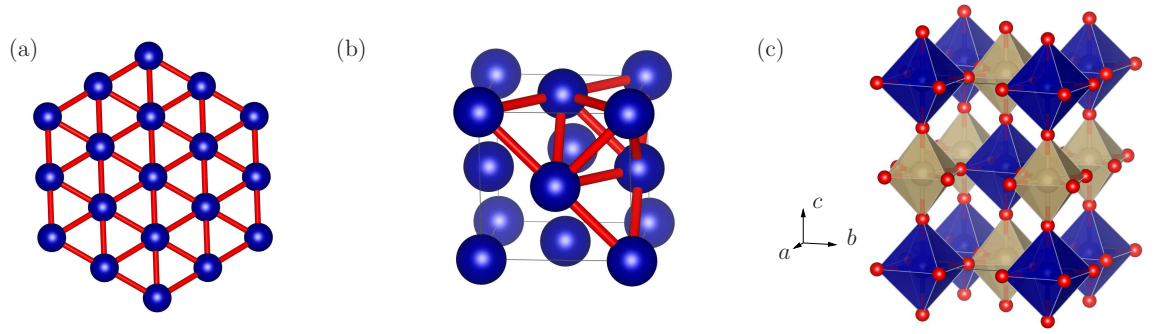
Figure 3.1: (a) The extended 2D triangular lattice. (b) The fcc conventional unit cell, with selected nn bonds shown to highlight their triangular arrangement. The fcc lattice may be considered as an extended array of edge-sharing tetrahedra, and a single tetrahedron is highlighted. (c) The double perovskite structure comprising two interpenetrating fcc sublattices. The octahedral oxygen environment is shown for the B and B' anions. The A anions have been omitted for clarity. Crystal structures throughout this thesis are visualised using VESTA [78, 79].

It is not possible to satisfy all spin interactions in this instance, and there is not a unique ground state. Extending this picture to an infinite 2D triangular lattice [Fig. 3.1(a)] does not alleviate the frustration, and Ising spins on this lattice in the presence of AFM nearest-neighbour (nn) interactions do not order, but instead are believed to form a spin liquid with considerable ground-state entropy arising due to the energy degeneracy [73, 74]. Moving on to 3D, it may be seen that nearest-neighbours within the fcc lattice are still arranged in triangles, as an fcc lattice can be pictured as an extended network of edge-sharing tetrahedra [Fig. 3.1(b)], and geometric frustration is still present [75, 76]. The DP structure comprises two interpenetrating fcc sublattices [Fig. 3.1(c)], where interlattice interactions further complicate matters, in addition to the intralattice frustration, and in some instances leads to spin glass behaviour [77].

Within the DP family $A_2BB'O_6$, choosing a combination of $3d$ and $5d$ transition metals (TMs) for the cations B and B' makes a plethora of exotic physical properties possible: for example the half metals Sr_2FeMoO_6 and Sr_2FeReO_6 which display colossal magnetoresistance [80] and room-temperature tunneling magnetoresistance [81], respectively. Half metallicity is an avenue for the generation of spin-polarised electrical currents, which is of great importance for potential spintronic applications.
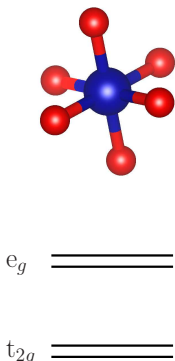
The insulating compound Sr_2CrOsO_6, for example, displays ferrimagnetism below the critical temperature [82] $T_c \approx 725$ K and strong magneto-optical coupling [83], with continuing debate over the underlying mechanism behind the remarkably high value of T_c [84, 85]. Recently, a theoretical study has predicted moderate doping on the Sr site in Sr_2CrOsO_6 should result in half metallicity with T_c remaining high [86].

In these systems the relative occupancy, symmetry and energy scales of the d-orbitals on the B and B' sites determine the nature of the magnetic interactions, through a competition between on-site Coulomb repulsion (which can be described by the Hubbard U and Hund's rules), which would favour a superexchange mechanism between localised spins, and kinetic energy reduction via electron delocalisation which favours double exchange (DE) [87–89]. The impact of the large spatial extent of $5d$ orbitals is further complicated by the role of spin-orbit (SO) interactions, which have been shown to produce interesting states including an unconventional Mott insulator phase in TM oxides [90, 91]. Taken together, these complications mean that a straightforward application of the Goodenough Kanamori Anderson (GKA) rules for superexchange [92–94] is not possible.

This chapter shall present the results of μSR studies of the four DP compounds Sr_2CoOsO_6, Sr_2FeOsO_6, Sr_2YOsO_6 and Sr_2InOsO_6 (hereafter SCOO, SFOO, SYOO and SIOO, respectively). An overview of properties of the B and B' ions which feature in these materials is provided in Fig. 3.2. In all instances the cations are in the high-spin state.

3.2   Experimental Procedure

Zero-field μSR measurements of the double perovskite compounds SCOO, SFOO, SYOO and SIOO were carried out on powder samples (synthesised by M. Jansen and colleagues in Dresden and Stuttgart) using the GPS spectrometer at SμS. The samples were packed in Ag envelopes (foil thickness 25 μm) and taped to a silver fork in the so-called 'fly-past' configuration, in order to minimise the background contribution from muons that do not stop in the sample. Ag is used to contain the sample since its small nuclear magnetic moment causes only a very small background

Compound	Ion	Configuration	S
SCOO	Co^{2+}	$3d^7$	3/2
SCOO	Os^{6+}	$5d^2$	1
SFOO	Fe^{3+}	$3d^5$	5/2
SFOO, SYOO, SIOO	Os^{5+}	$5d^3$	3/2
SYOO	Y^{3+}	$4d^0$	0
SIOO	In^{3+}	$4d^{10}$	0

e$_g$

t$_{2g}$

Figure 3.2: The octahedral oxygen environment for a transition metal ion, and the ensuing crystal field splitting of the d orbitals. Table of charge states, d-shell electron configurations and resultant spin quantum number S for the B and B' sites in Sr$_2$$BOsO_6$ (B = Co, Fe, Y, In).

signal.

3.3 Sr$_2$CoOsO$_6$

Previous characterisation [95] of SCOO using X-ray absorption spectroscopy revealed the valence states as Co^{2+} and Os^{6+} (listed in Fig. 3.2). DC magnetic susceptibility χ and heat capacity C_P detect AFM order upon cooling through $T_{\mathrm{N1}} = 108$ K, from the high temperature paramagnetic phase. In addition, upon further cooling below a secondary transition temperature $T_{\mathrm{N2}} = 67$ K, a second, distinct AFM spin structure is encountered. X-ray powder diffraction also identifies a structural transition coinciding with the onset of magnetic order at T_{N1} from a high-temperature tetragonal phase ($I4/m$) to a low-temperature monoclinic one ($I2/m$) [95].

In order to elucidate the nature of the two AFM phases, our collaborators at the Max-Planck-Institut für Chemische Physik fester Stoffe, Dresden performed neutron powder diffraction (NPD) experiments on SCOO for $2 \leq T \leq 122$ K [65]. The provisional magnetic behaviour encountered upon cooling from the high-temperature paramagnetic phase is summarised below.

- $T_{\mathrm{N2}} \leq T \leq T_{\mathrm{N1}}$: Within the first AFM phase below $T_{\mathrm{N1}} = 108$ K (labelled AF1) both Co and Os moments are partially ordered within the ab-plane. The refined moment sizes within this phase are much smaller than their theoretical

Figure 3.3: Spin structures for the various AFM phases in SCOO, depicted in the pseudo-cubic unit cell of the monoclinic space group $B2/n$. Magnetic structure of the (a) AF1, (b) AF2′, (c) AF2 = AF1+AF2′ and (d) AF2″ phases, where Os spins are canted randomly in AF2″. Black and blue spheres (arrows) represent Co atoms (corresponding moments) with dynamical and frozen spins, respectively. Similarly, gray and yellow spheres (arrows) represent Os atoms (corresponding moments) with dynamical and frozen spins, respectively. Figure taken from Ref. [65].

values, indicating that both Co and Os moments are dynamically fluctuating, and neutrons are sensitive to their *average* ordered moments. The AF1 spin arrangement is shown in Fig. 3.3(a), where the average ordered moments are aligned almost (anti)parallel to the [110] direction (where the notation of the pseudo-cubic unit cell is used for convenience and simplicity).

- 5 K $\lesssim T \leq T_{\mathrm{N2}}$: A second set of magnetic reflections appear as T drops below $T_{\mathrm{N2}} = 67$ K, corresponding to a pseudomagnetic phase labelled AF2′. The overall magnetic structure in this temperature range is labelled AF2 and is given by the superposition of AF1 and AF2′ (i.e., the vector addition of the two phases). The spin structure described by AF2′ is shown in Fig. 3.3(b) and comprises an AFM arrangement of Co moments aligned (anti)parallel to the crystallographic c-axis, while no additional ordering of the Os is present. As temperatures are lowered within this phase the Co spins start to become frozen and become totally static for $T < 20$ K (as indicated by a saturation in the refined moment value). In contrast, the Os ordered moment value

does not change in this temperature region, showing that the Os sublattice is still fluctuating dynamically, with average moments still described by the AF1 structure. The resulting noncollinear magnetic structure AF2 is shown in Fig. 3.3(c).

- $T \lesssim 5$ K: Finally, as temperature is decreased below around 5 K the Os freeze into a randomly canted state, in a manner reminiscent of a spin glass. The (spatially) average Os moments still preserving the ordered AF1 state within the *ab*-plane. This overall magnetic state is labelled AF2″ and is shown in Fig. 3.3(d).

The glassy behaviour of the magnetism below around 5 K is consistent with AC susceptibility measurements, where a characteristic cusp is seen in the temperature dependence of the real component χ' at a freezing temperature T_f [65]. The value of $T_f(\omega)$ shifts to higher temperatures in the expected manner as the AC frequency is increased and a resultant fit yields a zero-frequency freezing temperature $T_{f,0} = 5$ K and a characteristic spin relaxation time scale $\tau_0 = 4$ μs [96].

3.3.1 μSR Measurements

The results of muon-spin relaxation (μSR) measurements, presented below, support the picture deduced via NPD and AC susceptibility results. Typical asymmetry spectra are shown in Fig. 3.4. For $T \gg 110$ K only a slow relaxation is observed [Fig. 3.4(c)], typical of a paramagnet. On cooling below $T \approx 110$ K a fast-relaxing component is resolved [Fig. 3.4(b)] with a sizeable relaxation rate, resulting from the muon ensemble experiencing a broad distribution of large, slowly fluctuating magnetic fields (see Sec. 2.4.4). Its development coincides with a loss of asymmetry in the amplitude of a non-relaxing (or, more likely, very slowly relaxing) component A_s. (However, the total observed asymmetry is reduced compared to its value in the paramagnetic regime.) The data were fitted to a relaxation function of the form

$$A(t) = A_f e^{-\Lambda t} + A_m e^{-\lambda t} + A_s, \tag{3.1}$$

with fixed parameters $A_m = 4.5\%$, $\lambda = 0.35$ MHz and $\Lambda = 30$ MHz, determined from an initial fit of the data where all parameters were allowed to vary. The component

Figure 3.4: Sample asymmetry spectra for SCOO. In the region $65 \lesssim T \lesssim 110$ K a fast relaxing component is observed at early times which vanishes as the temperature is lowered. *Left inset:* Below 65 K oscillations are observed consistent with a uniform magnetic field distribution resulting from the ordered Co sublattice only. *Right inset:* Cooling below 2 K results in a sharp increase in non-relaxing amplitude and additional relaxation becoming resolvable.

with amplitude A_m therefore represents a temperature independent contribution to the signal. The amplitude A_f peaks below 100 K (Fig. 3.5) and then smoothly decreases as temperature is lowered further. The disappearance of this fast-relaxing component is accompanied by the smooth increase in A_s. Below a temperature of $T \approx 65$ K one may also begin to resolve spontaneous oscillations in the asymmetry spectra at very early times [inset, Fig. 3.4(a)], consistent with the existence of a quasistatic field distribution at the muon sites, with a narrow width, involving smaller and more uniform fields than that giving rise to the high temperature behaviour. Fitting these to a cosinusoidal function allows the estimation of the oscillation frequency as $\nu_\mu \approx 90$ MHz.

It is likely that the muon is sensitive to the field distribution resulting from both Co and Os moments, although the time scale of the muon measurement differs from that of NPD. Compared to muons, whose time-scale is determined by the gyromagnetic ratio $\gamma_\mu = 2\pi \times 135.5$ MHz T^{-1}, neutrons effectively take a 'snapshot' of the spin distribution (see Sec. 2.2.3), so will see magnetic order in cases where the muon response reflects slow fluctuations of the moments on the nanosecond or microsecond time scale. As a result, the fast relaxation with amplitude A_f most probably reflects the slowing down and freezing of the Co moments. Although these

Figure 3.5: Fitted parameters from Eq. 3.1 to SCOO data. The amplitude of the fast relaxing component A_f is seen to peak around 100 K and decrease as temperature is lowered (red line is a guide to the eye). The amplitude of the slowly relaxing component A_s drops upon cooling through T_{N1} and subsequently increases gradually as temperature is decreased further.

moments undergo a transition to become (partially) ordered on the neutron time scale below 108 K, slow fluctuations appear to prevent a discontinuous response of the muon probe at this temperature. Instead an increase in A_f is visible below 110 K, which probably corresponds to partial order of the Co moments developing on cooling until around 100 K. Below that temperature, there exists partial order of the Co ions on the muon time scale, coexisting with the fluctuations along the z-direction which themselves slow down on cooling, freezing out relatively smoothly and causing a decrease in A_f. In the fast fluctuation limit it is expected that the muon relaxation rate is given by $\lambda \propto \gamma_\mu^2 \langle B^2 \rangle \tau$ [36]. Given an oscillation frequency ($\nu_\mu = \gamma_\mu B / 2\pi$) at low temperature of roughly 90 MHz, one may estimate $B \approx 0.6$ T. Using $\Lambda = 30$ MHz in the region $65 \lesssim T \lesssim 110$ K an approximate characteristic time scale for the Co moment fluctuations is $\tau \approx 0.1$ ns.
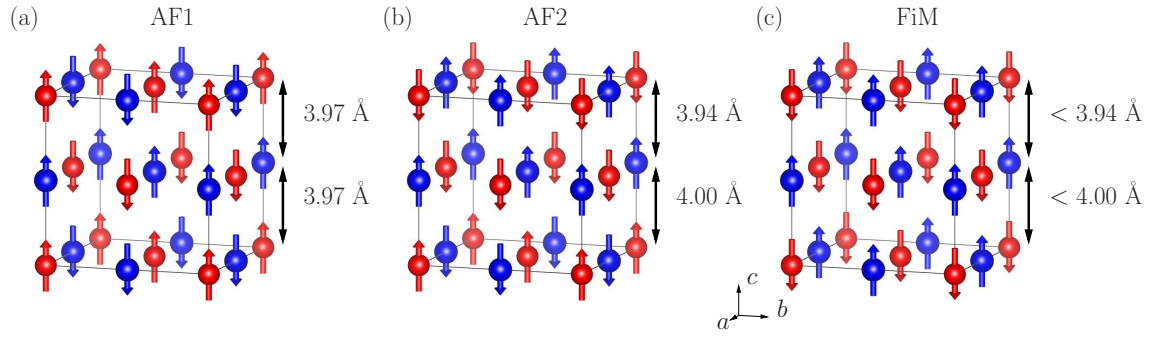
Below 65 K the more uniform distribution of internal magnetic fields that arise from the well-ordered Co-sublattice allows oscillations in the muon spectra to be resolved. The increase in the non-relaxing component A_s on cooling below 100 K might then result from the freezing out of relaxation channels reflecting dynamic

fluctuations of the partially ordered, fluctuating Os spins.

Finally, on cooling below 2 K [inset, Fig. 3.4(b)] additional relaxation is observed together with, most notably, a sharp increase in the non-relaxing amplitude of the signal. In a powder sample it may be expected that 1/3 of muon spins will lie along the direction of any static local fields and, in the absence of dynamics, not experience any relaxation (see Sec. 2.4.1). The transition from a dynamic to static regime may then be identified by an upward shift in the non-relaxing amplitude of the signal. The observed jump in the non-relaxing amplitude and additional relaxation therefore reflects a freezing of the Os moments on the muon time scale, which also allows further relaxation processes to enter the muon time window.

Taken together, these experimental results indicate exotic lattice-site-specific spin dynamics, which lead to distinct freezing processes and ground states for the Co and Os sublattices. In order to better understand the mechanisms underlying this unusual behaviour collaborators performed *ab initio* calculations to investigate the electronic structure within SCOO. These calculations reveal there is very little energetic overlap between Co-3d and Os-5d orbitals, which leads to weak *interlattice* magnetic superexchange interactions (despite these being the shortest, nn exchange pathways) and explains the relatively decoupled magnetic behaviour of the Co and Os spin sites. In contrast, greater overlap between *intralattice* orbitals leads to dominant exchange interactions acting between spins of the same species. Considerations of density of states and projections of calculated wavefunctions onto Wannier orbitals reach these same conclusions. The exchange interactions within the fcc-like Os sublattice were found to promote much stronger magnetic frustration than those in the Co sublattice, which explains the persistence of Os spin dynamics to temperatures well below T_{N2} (where the Co spins freeze) and the glassy behaviour of the Os sublattice in the AF2″ state.

A separate study [97] drew the same conclusions regarding the presence of strong intra and weak intersublattice exchange interactions being responsible for the site-specific magnetic ordering observed in SCOO. However, in contrast to the magnetic spin structures detailed above, the conclusion drawn in Ref. [97] was that only the Os sublattice orders upon cooling below T_{N1}, and that the Co sublattice independently

Figure 3.6: Spin structures for the various magnetic phases in SFOO, shown in the unit cell of the pseudocubic space group $Fm\bar{3}m$. Magnetic structure of the (a) AF1, (b) AF2 and (c) ferrimagnetic (FiM) phases, the FiM phase is achieved via the application of hydrostatic pressure. Red and blue spheres (arrows) represent Fe and Os atoms (corresponding moments), respectively. The bifurcation of Fe-Os distances along the c-axis within the AF2 phase is shown.

orders upon cooling below T_{N2}. In this scenario, the fully ordered AFM state proposed below T_{N2} would not be consistent with the additional glassy magnetic behaviour observed below around 5 K discussed in this section.

3.4   Sr$_2$FeOsO$_6$

The related compound SFOO, also exhibits some intriguing magnetic phenomena. Physical and magnetic characterisation of SFOO shows that it is a narrow gap semiconductor where the crystal assumes the tetragonal $I4/m$ space group [98], as predicted by first principles calculations [99]. The system assumes an antiferro-magnetically ordered state [labelled AF1, Fig. 3.6(a)] below the Néel temperature $T_N \approx 140$ K, which precedes a magneto-structural transition upon further cooling at $T_2 = 67$ K [labelled AF2, Fig. 3.6(b)] [100]. The ordered magnetic spin structure in this low-T phase adopts a different sequence of spin orientations along the tetrago-nal c-axis due to a lattice instability which supports a bifurcation of iron-osmium distances [Fig. 3.6(b)], reflecting the subtle balance between degrees of freedom and competing exchange interactions in this system [101]. Detailed first principles studies revealed the importance of AFM out of plane next-nearest-neighbour (nnn) interactions between the extended Os $5d$ orbitals, which compete with ferromagnetic

Figure 3.7: A schematic showing (a) the AFM superexchange interaction between neighbouring $t_{2\mathrm{g}}$ orbitals and (b) the FM DE interaction acting between e_{g} orbitals. Both exchange mechanisms are mediated along the c-axis by oxygen p orbitals. Figure taken from Ref. [103].

(FM) nn Fe-Os DE interactions and introduce strong frustration [102]. This is believed to be the dominant factor in driving the system to the AF2 spin structure, where spins along the crystallographic c-axis order in an alternating ↑↑↓↓ sequence.

The fragility of the FM DE interaction in SFOO has been demonstrated using the application of external pressure, where compression leads to a reversal in sign of the Fe-Os exchange interaction along the c-axis as the AFM superexchange interaction between t_{2g} orbitals overcomes the FM DE interaction between e_g orbitals to induce an overall ferrimagnetic (FiM) ground state [Fig. 3.6(c)], with considerable remanent magnetisation and coercivity [103].

The large spatial extent of the Os $5d$ orbitals leads to a large crystal field splitting at this site (denoted $10Dq_{,\mathrm{Os}}$) but only a small splitting due to Hund's exchange ($J_{\mathrm{Hund,Os}}$). The kinetic energy saving due to electron delocalisation via DE is proportional to $J_{\mathrm{Hund,Os}}$ and is highly sensitive to the degree of collinearity, as visualised through the arrangement of orbitals shown in Fig. 3.7(b). In contrast, the

Figure 3.8: SFOO ZF μSR asymmetry data measured for (a) $T = 20$ K, (b) 65 K and (c) 145 K. Inset to (b): typical oscillations visible at early times in the intermediate temperature region. Solid lines are fits described in the main text.

superexchange mechanism in Fig. 3.7(a) is affected much less by nonlinearity. The buckled arrangement of octahedra within the ab-plane therefore diminishes the role of the DE interaction, resulting in the robust AFM spin structure within this plane; only the spin sequence along the c-axis varies between the different phases [Fig. 3.6(a)-(c)]. The application of pressure compresses both the Os and Fe octahedra, however the very different spatial extents of the $3d$ and $5d$ orbitals means this compression leads to an unequal response in the crystal field splitting at the two sites, which suppresses the FM DE interaction and leads to the alternating ↑↓↑↓ sequence of spins along the c-axis in the FiM phase [Fig. 3.6(c)].

3.4.1 μSR Measurements

Example μSR asymmetry data for SFOO are shown in Fig. 3.8. Oscillations in the measured asymmetry are resolvable for early times ($t \lesssim 0.1$ μs) in the temperature range $60 \lesssim T \lesssim 135$ K [see Fig. 3.8(b) inset], which is unambiguous evidence for LRO of magnetic moments. Asymmetry averaged over early-times, i.e., $\overline{A}_0 \equiv \langle A(t \leq 0.1$ μs)$\rangle$, is shown in Fig. 3.9(d). For low temperatures the initial asymmetry is approximately constant. However, around 120 K it increases dramatically upon warming across the transition region around T_N. This recovery of initial asymmetry reflects the gradual destruction of LRO. There are no marked features in $\overline{A}_0$ around

the secondary transition at T_2. The broadened step-function

$$\overline{A}_0(T) = A_2 + \frac{A_1 - A_2}{e^{(T-T_{\mathrm{mid}})/w}} \qquad (3.2)$$

may be used to parametrise the smooth transition between high- (low-) temperature asymmetry values A_2 (A_1) with midpoint T_{mid} and width w [104]. The resultant fit for $T \geq 65$ K data sets yielded $T_{\mathrm{N}} = T_{\mathrm{mid}} \pm w = 134(6)$ K.

Below T_{N} the presence of large quasistatic, or slowly fluctuating, magnetic fields at the muon stopping sites (with components perpendicular to the muon polarisation direction) leads to a rapid dephasing of spin coherence. In the fast fluctuation limit, relaxation rates vary as $\lambda \propto \langle B^2 \rangle \tau$, where $1/\tau$ is representative of a fluctuation rate associated with dynamics [36], and the second moment of the field distribution $\langle B^2 \rangle$ is expected to be large for an ordered magnetic system comprising two magnetic species. Components with relaxation rates of several hundred μs^{-1} will not be resolved and so are 'lost' from the asymmetry data [Fig. 3.8(b) and (c)]. The component of asymmetry which is lost upon cooling through T_{N} is $A_{\mathrm{lost}} = A_2 - A_1 = 12.8(4)\%$.

In order to parametrise the behaviour across all available temperatures, data for all times ($t \leq 9.7$ μs) were heavily binned (such that the histogram interval width was $\Delta t = 14.6$ ns) and fitted to the relaxation function

$$A(t) = A_{\mathrm{s}}e^{-\lambda_{\mathrm{s}}t} + A_{\mathrm{f}}e^{-\lambda_{\mathrm{f}}t} + A_{\mathrm{bg}}. \qquad (3.3)$$

Here, s and f denote slow (small λ) and fast (large λ) relaxation components, respectively, and A_{bg} is a time-independent baseline contribution arising from muons which stop in the silver sample holder, or whose spin lies parallel to a static magnetic field and therefore do not depolarise. The fitted relaxation rates $\lambda_{\mathrm{s,f}}$ were found to be approximately constant across the temperature range, to within uncertainties, and so were fixed to their average values of 0.46 MHz and 5.4 MHz, respectively.

The fitted values of the component amplitudes are displayed in Fig. 3.9(a)–(c). All three components undergo large changes of amplitude around $T_{\mathrm{N}} \approx 140$ K consistent with magnetic ordering. The width of the transition region (approximately 10 K) indicates a degree of static or dynamic disorder in the ordered moments. The baseline and slow relaxation amplitudes A_{bg} and A_{s} both sharply decrease from their high temperature values at around T_{N}. Whilst A_{s} does not undergo any further changes,

Figure 3.9: Fitted values of (a) fast relaxation, (b) slow relaxation and (c) baseline component amplitudes from Eq. 3.3. The dashed grey lines indicate the Néel temperature $T_N = 135$ K and the secondary transition temperature $T_2 = 67$ K. (d) Fitted precession frequencies obtained by fitting asymmetry data to Eq. 3.4 with red line a fit to the phenomenological expression Eq. 3.5, and early time average asymmetry with dashed green line a fit to the broadened step function Eq. 3.2.

the baseline amplitude A_{bg} starts to increase upon cooling below around $T_2 = 60$ K. The increase in the non-relaxing amplitude is indicative of a greater static component of the magnetism as temperatures are lowered, since, in the absence of dynamics, a muon whose spin lies parallel to the local field at its stopping site will not be depolarised.

The behaviour of the fast relaxation component is somewhat different; its amplitude displays an asymmetric peak, with a sudden increase upon cooling through T_N followed immediately by a gradual decrease as temperature is reduced further. The peak in the fast relaxation amplitude may indicate the freezing of dynamics accompanying the transition to magnetic LRO.

We now turn to the oscillations in the measured asymmetry within the temperature range $60 \lesssim T \lesssim 135$ K [Fig. 3.8(b) inset]. In a quasistatic magnetic field, with magnitude B, a muon will undergo Larmor precession with frequency ν given by $2\pi\nu = \gamma_\mu B$ where $\gamma_\mu = 2\pi \times 135.5$ MHz/T is the muon gyromagnetic ratio. This intermediate temperature range is approximately bounded by the Néel temperature T_N and secondary ordering temperature T_2 as reported in previous magnetic measurements [98]. Data in this temperature range were fitted to the damped oscillatory relaxation function

$$A(t) = A_{\mathrm{osc}}e^{-\lambda_{\mathrm{osc}}t} \cos\left(2\pi\nu t + \phi\right) + A_{\mathrm{rel}}e^{-\lambda_{\mathrm{rel}}t} + A_{\mathrm{bg}}, \qquad (3.4)$$

for $t \leq 1$ μs. For the detector geometry used there should be zero phase offset, and indeed the data were fitted well with ϕ set to zero (significantly, this was not the case for $B = \mathrm{Y}, \mathrm{In}$ as discussed below in Sec. 3.5.1). The fitted oscillatory amplitudes were found not to vary significantly with temperature, and so were fixed to the average value $A_{\mathrm{osc}} = 3.2\%$. The total transverse component of the asymmetry data is therefore $A_\perp = A_{\mathrm{lost}} + A_{\mathrm{osc}} \approx 16\%$, which is approximately two-thirds of the high-temperature total asymmetry $A_2 = 23.3(3)\%$ (from Eq. 3.2), as expected for a powder sample. The single precession frequency is ascribed to the presence of one class of muon stopping site which gives rise to a single oscillatory component in the asymmetry data (see Sec. 3.6).

The fitted precession frequency ν drops steadily upon warming from 65 K towards T_N, which coincides with the recovery of initial asymmetry as LRO is destroyed, in a typical fashion for an ordered system [Fig. 3.9(d)]. The fitted frequency values are an effective order parameter, so for $T \geq 65$ K they were in turn fitted to the phenomenological expression

$$\nu(T) = \nu_0 \left[1 - \left(\frac{T}{T_N} \right)^\alpha \right]^\beta, \qquad (3.5)$$

yielding a Néel temperature $T_N = 135(2)$ K and a zero-temperature frequency $\nu_0 = 50(1)$ MHz for $\alpha = 4.2(9)$ and $\beta = 0.42(7)$, as shown in Fig. 3.9(d). Here, the fitted value of β is slightly larger than that expected for the critical exponent of a 3D Heisenberg antiferromagnet (where the critical exponent $\beta = 0.367$ [7]). Very

heavily damped oscillations were also visible in asymmetry data for temperatures just below T_2, where the fitting function was able to capture an initial increase in asymmetry at very early times, but not to extract a reliable value of ν. Oscillations cease to be resolvable altogether as temperatures are lowered further, indicating a broad range of internal magnetic fields experienced by the muon ensemble resulting in loss of coherent spin precession. This is evidence that supports the coexistence of the AF1 and AF2 phases proposed in reference [101]; if magnetic spin directions simply reoriented to adopt the AF2 configuration, then one would expect to continue to resolve oscillations in the μSR data, albeit with different precession frequencies.

These results may be contrasted to those of SCOO, from Sec. 3.3. In SFOO, the presence of muon-spin precession oscillations in the AF1 phase (for intermediate temperatures $T_2 \leq T \leq T_N$) is consistent with simultaneous quasistatic magnetic ordering on both the Fe and Os sublattices. This is in contrast to the dynamical partial order observed just below T_{N1} in SCOO, which precludes the appearance of coherent muon-spin precession. The absence of oscillations in SFOO below T_2 is further evidence for phase coexistence for this low temperature regime. These μSR results show no evidence of any further spin freezing in SFOO for temperatures down to 5 K, in contrast to those for SCOO.

3.5 Sr$_2$YOsO$_6$ and Sr$_2$InOsO$_6$

In the systems SYOO and SIOO B is a non-magnetic $4d$ ion ($4d^0$ and $4d^{10}$ for Y^{3+} and In^{3+}, respectively), leaving just a fcc-like lattice of magnetic Os^{5+} ($5d^3$) ions [105]. AFM nn interactions (J_{nn}) within this structure are expected to create strong geometric frustration which precludes long range magnetic ordering (LRO). However, the degeneracy of ground state spin structures may be alleviated through either long ranged nnn interactions (J_{nnn}) or magnetic anisotropy [106], leading to magnetic ordering below suppressed onset temperatures of $T_N = 53$ K and 26 K for SYOO and SIOO, respectively [105]. The presence of frustration may be inferred from the large ratio between the Weiss constant and ordering temperature $|\theta|/T_N$ for these compounds.

3.5.1 μSR Measurements

Example μSR asymmetry spectra for SYOO and SIOO measured at several temperatures are shown in Fig. 3.10(a) and (b). Little change is observed in the asymmetry spectra at temperatures above T_N for each compound, where the data are well described by a Gaussian relaxation function (not shown). This is expected for the paramagnetic phase where rapidly fluctuating electronic dipole moments centred on the Os ions are motionally narrowed from the signal, and the muon response is dominated by quasistatic magnetic fields due to the nuclear dipole moments.

The temperature dependence of the time-averaged asymmetry $\overline{A} \equiv \langle A(t \leq 9.69\ \mu\mathrm{s})\rangle$ [Fig. 3.10(c) and (d)] provides a means of determining the transition temperature. The broadened step function, Eq. 3.2, was again used to parametrise the drop of asymmetry upon cooling and the resultant fit yielded $T_\mathrm{N} = 53.0(2)$ K for SYOO and $T_\mathrm{N} = 25.4(5)$ K for SIOO, in good agreement with previous characterisation [105].

For temperatures below the transition at T_N magnetic moments order and oscillations become visible in the spectra, which indicates quasistatic LRO. The asymmetry spectra $A(t)$ within the ordered regime could be fitted to a function comprising a damped oscillatory component and a slowly relaxing exponential term Eq. 3.4. However, a non-zero phase ϕ was found to be necessary to fit data for both SYOO and SIOO, with temperature-averaged values of $-47(2)°$ and $-44(4)°$, respectively.

A damped cosinusoidal oscillation with phase $\phi \approx -45°$ closely resembles a zeroth order Bessel function of the first kind, which is indicative of incommensurate (IC) magnetic order [107, 108]. If the local magnetic field strength B varies sinusoidally in space within a material as $B(\boldsymbol{r}) = B_\mathrm{max} \sin{(\boldsymbol{k} \cdot \boldsymbol{r})}$, where the wavevector $\boldsymbol{k}$ is IC with the crystal lattice, then this will give rise to a magnetic field probability density function

$$p(B) = \frac{2}{\pi}\frac{1}{\sqrt{B_\mathrm{max}^2 - B^2}}, \tag{3.6}$$

for fields $B < B_\mathrm{max}$ (and zero otherwise) [107, 109], plotted in Fig. 3.11(a). The time evolution of the muon polarization component which is transverse to the local

Figure 3.10: Example spectra for (a) SYOO and (b) SIOO at selected temperatures, showing oscillations for $T \lesssim 53$ and 25 K, respectively. (c) and (d) Temperature dependence of the fitted characteristic oscillatory frequency ν, and the time-averaged asymmetry $\overline{A}$. Solid lines are fits described in the text and dashed lines indicate T_N.

magnetic field is given by

$$G(t) = \int_{-\infty}^{\infty} dB \; p(B) \cos{(\gamma_\mu B t)}. \tag{3.7}$$

Combining Eq. 3.6 and Eq. 3.7 yields

$$G(t) = \int_{0}^{\pi/2} \mathrm{d}\theta \; \cos{(\gamma_\mu B_{\max} t \sin \theta)} = J_0(2\pi\nu t), \tag{3.8}$$

where $J_0(x)$ is the zeroth order Bessel function of the first kind [plotted in red in Fig. 3.11(b)], and the characteristic frequency ν is given by $2\pi\nu = \gamma_\mu B_{\max}$. Strictly speaking, the use of this function assumes that the magnitude of the magnetic field strength at the muon site varies sinusoidally in space about an average of zero along with the wavelength determined by the magnetic wavevector being sufficiently

Figure 3.11: (a) The probability density function $p(B)$ for a magnetic field distribution that varies cosinusoidally in space, with maxima B_{max}. (b) Comparison of oscillatory relaxation functions.

large, relative to the crystallographic unit cell, that the implanted muons thoroughly sample the magnetic order, particularly in the regions close to the nodes. For large x, corresponding to $t \gg (\gamma_\mu B_{\text{max}})^{-1}$ for our purposes, it may be shown that $J_0(x) \approx (1/\sqrt{x}) \cos(x - 45°)$ [plotted in green in Fig. 3.11(b)].

The fitting procedure was therefore repeated for both the Y and In compounds (for $t \leq 9.69$ μs) with an exponentially damped Bessel function $J_0(2\pi\nu t)$, plus a slowly relaxing exponential term:

$$A(t) = A_{\text{osc}}e^{-\lambda_{\text{osc}}t}J_0(2\pi\nu t) + A_{\text{rel}}e^{-\lambda_{\text{rel}}t} + A_{\text{bg}}, \tag{3.9}$$

where $\nu = (1/2\pi)\gamma_\mu B_{\text{max}}$ now represents a characteristic precession frequency and B_{max} is the maximum local magnetic field magnitude. The oscillatory amplitude A_{osc} was fixed to the value of 11.6% for SYOO, obtained via a global fit to the data measured for $T \leq 45$ K, and left free to vary for SIOO [in both cases $A_{\text{osc}} \approx (2/3)A(t = 0)$, as expected for a powder sample]. Typical fits are presented in Fig. 3.10(a) and (b) and the temperature dependence of the parameter ν is shown in Fig. 3.10(c) and (d).

Figure 3.11(b) shows there are subtle differences between an exponentially damped cosine function and the Bessel function J_0. The quality of fit (given by χ^2) is extremely similar for the two fitting procedures, employing cosinusoidal Eq. 3.4 and Bessel Eq. 3.9 relaxation functions. However, a close inspection of early-time data shows
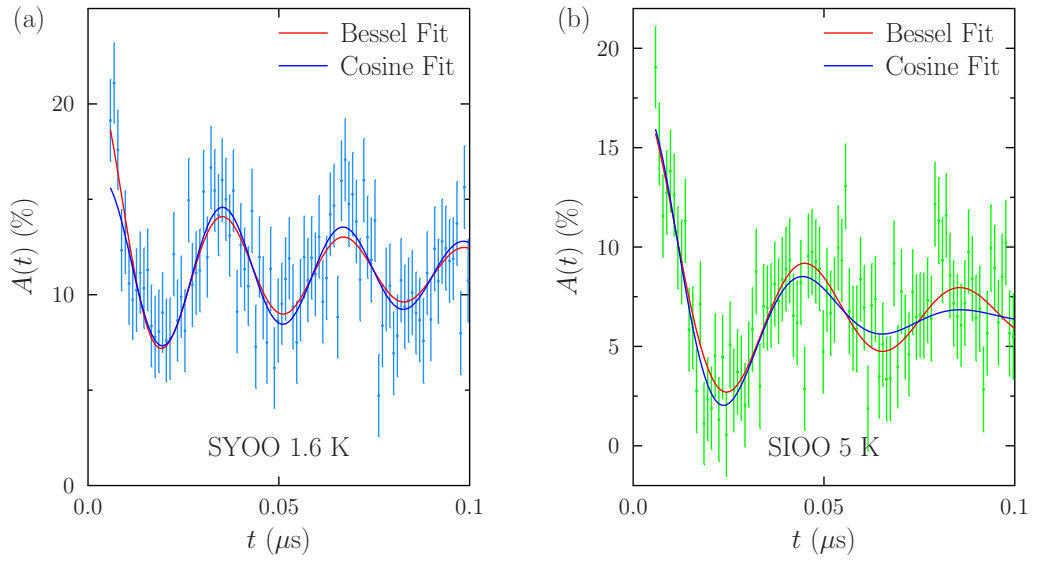
that the Bessel function better captures the features present in certain datasets, as shown in Fig. 3.12. It appears that whereas the Bessel function is able to provide a satisfactory fit to datasets within both SYOO and SIOO, the exponentially damped cosinusoidal function prioritises either the fast relaxation feature at very early times at the expense of successive oscillatory extrema [shown in Fig. 3.12(b), where the blue cosine function seems overdamped relative to the SIOO data], or vice versa [as for the SYOO data shown in Fig. 3.12(a), where the cosine function misses the first few data points]. Data with greater statistics would be required to conclusively select either fitting function on the basis of fit quality alone.

Recently, IC magnetic order has been discovered in the related fcc DPs La_2NaRuO_6 ($4d^3$) and La_2NaOsO_6 ($5d^3$) on the basis of μSR, NPD and inelastic neutron scattering [110, 111], where non-magnetic Na ions occupy the B site, and $S = 3/2$ $(Ru/Os)^{5+}$ ions occupy the B' site. A suggested explanation for this is that a delicate balance between the relative signs and magnitudes of J_{nn} and J_{nnn} leads to the system lying on a boundary between AFM phases in the mean field theory J_{nn}- J_{nnn} phase diagram, where only commensurate magnetic ordering is predicted [112].

The fitted initial asymmetry $A(t = 0)$ is found to be temperature independent for both systems; no asymmetry is lost in these compounds, unlike for SCOO and SFOO. The major difference between these systems is that SYOO and SIOO only contain one magnetic species, so internal magnetic field distributions are expected to comprise smaller, more spatially uniform fields, and the spin structures may promote less complicated spin dynamics relative to SFOO. Together these factors all engender smaller relaxation rates.

The characteristic precession frequency ν acts as an effective order parameter for the LRO phase, and its temperature dependence was therefore fitted to the phenomenological expression Eq. 3.5. For SYOO the resultant fit yields a value of the Néel temperature $T_N = 52.7(0.1)$ K [with $\alpha = 6.2(4)$ and $\beta = 0.36(3)$] and the fitted zero-temperature oscillatory frequency $\nu_0 = 30.8(1)$ MHz equates to a maximum quasistatic magnetic field strength of $B_{max} = 0.227(1)$ T. For SIOO the paucity of data sets near the transition required the Néel temperature to be fixed to $T_N = 25.4$ K, as obtained from the $\overline{A}$ fitting procedure. The fit yielded $\alpha = 2.4(6)$, $\beta = 0.39(6)$ and

Figure 3.12: A comparison of typical early-time fits of the cosinusoidal (Eq. 3.4) and Bessel (Eq. 3.9) relaxation functions to low temperature data measured for (a) SYOO at $T = 1.6$ K and (b) SIOO at $T = 5$ K.

the zero-temperature oscillatory frequency $\nu_0 = 25.0(2)$ MHz, indicating a maximum quasistatic magnetic field strength of $B_{\max} = 0.185(2)$ T at the muon stopping sites. The fitted values of β for these two systems are close to that expected for a 3D Heisenberg antiferromagnet.

The ratio of the fitted zero-temperature characteristic precession frequencies ν_0 should be indicative of the relative sizes of the ordered moments of the $S = 3/2$ Os^{5+} ions for the two compounds. This ratio is given by

$$\frac{\nu_0(\text{Y})}{\nu_0(\text{In})} = \frac{30.8}{25.0} = 1.23(1). \tag{3.10}$$

In comparison, Rietveld refinement of NPD data reveals ordered moment sizes of $1.91\mu_B$ and $1.77\mu_B$ for the Y and In compounds, respectively, yielding a ratio of 1.08(4) [105]. These ratio values are in reasonable agreement; a possible cause of the difference between the two ratios is any extra hyperfine interaction between the muon and spin-polarised electron density in the Y compound. In addition, the difference in the unit cell dimensions between the two compounds [105] might lead to a slight relocation (in fractional coordinates) of the muon stopping site in each system. In Sec. 3.6 candidate muon stopping sites are identified for these compounds that occupy regions where the local magnetic dipole field strengths are varying

rapidly. These factors could explain why muon-spin precession frequencies do not scale straightforwardly with moment size or unit cell volume.

3.6   DFT and Dipole Simulations

Further information regarding the stopping site of implanted muons within the crystal unit cell plus the ensuing perturbation to its neighbouring environment allows a greater understanding of μSR results [113]. To this end, density functional theory (DFT) calculations have proved to be a valuable and powerful tool in the characterisation of muon states in host materials [44, 113–115].

In order to locate the muon stopping site in SFOO, collaborators in Durham and York performed ensemble density functional theory (DFT) calculations [116] using the CASTEP *ab initio* package [117, 118] (details may be found in Ref. [66]). Optimised lattice parameters were found by relaxing the unit cell geometry without an implanted muon, yielding $c = 7.810$ Å and $a = b = 5.501$ Å, in close agreement with those values previously reported for this compound [98, 101]. These parameters were fixed for subsequent calculations with a muon present. A muon was placed at random within the first octant of each unit cell subject to the constraint that it not be located within 0.2 Å of an ion. The unit cell geometry and lattice parameters were then optimised; this was repeated 101 times with different starting positions so that the optimal location of the muon, i.e., the location with the lowest energy, could be found. The optimal location of the muon was found to be $\boldsymbol{r}_\mu = (0.314, 0.130, 0.499)$ in fractional co-ordinates, 1.003(1) Å from the nearest O ion. The presence of the muon distorts the cell geometry, as can be seen in Fig. 3.13(b) and (c). In the following discussion it is assumed that all long range magnetic spin structures are robust enough that the presence of the muon and the subsequent lattice distortions do not perturb the local magnetic moments.

The consistency of the muon calculation performed in a single unit cell was checked by repeating the geometry relaxation for the optimal location in a $2 \times 2 \times 1$ supercell. The muon location was found to be (0.308, 0.116, 0.499), which is consistent with the results of the single cell (there is a 2% change in the value of the a co-ordinate and a

Figure 3.13: (a) Heat map showing the magnitude of the magnetic field $|\boldsymbol{B}|$ across the ab-plane (cross section taken at $c = 1/2$) from dipole field simulations using the AF1 spin configuration within the undistorted unit cell, and magnetic moment magnitudes μ_{eff} refined at $T = 75$ K from reference [101]. The muon site determined by DFT calculations ($p1$) is shown as a white cross, and contours corresponding to experimentally observed magnetic field strengths $B_{\mu,\text{exp}}$ are indicated (see main text). (b) and (c) chemical unit cell of SFOO following insertion of the muon (original positions of ions are translucent). Data are visualised using Jmol [119]. The cross-section in (b) is through the $c = 1/2$ plane, containing the muon. Blue represents Os ions, red O ions, grey Fe ions and black the muon (Sr ions are omitted for clarity). (d)–(f) Heat maps for SYOO, for various trial moment orientations within the ab-plane. The second class of muon site $p2$ is shown as a green cross. Plots for SIOO are very similar (not shown).

10% change in the value of the b co-ordinate). Similar distortions of the Fe–O–Os bonds in the same ab layer as the muon to those in the single cell case were observed. In addition, it was also found that in the $2 \times 2 \times 1$ supercell the Fe–O–Os bonds in the neighbouring layer are distorted to a similar degree in the opposite direction. However, the magnetic ions are not significantly displaced and so this should not severely impact the dipole field at the candidate muon stopping site.

Having identified a candidate muon stopping site using DFT, I. O. Thomas performed dipole field simulations which enable comparisons to be drawn between

theoretical and experimentally observed magnetic field strengths experienced by the muon ensemble. The magnitude of the magnetic dipole field at a muon stopping site may be calculated for a given spin structure using

$$B^\alpha(\boldsymbol{r}) = \frac{\mu_0}{4\pi} \sum_{i,\beta} \frac{\mu_{\text{eff},i} m_i^\beta}{R_i^3} \left(\frac{3 R_i^\alpha R_i^\beta}{R_i^2} - \delta^{\alpha\beta} \right), \tag{3.11}$$

where α and β run over x, y and z directions, i labels a magnetic ion located at $\boldsymbol{r}_i$ within a Lorentz sphere centred at $\boldsymbol{r}$, $\boldsymbol{R}_i = \boldsymbol{r} - \boldsymbol{r}_i$ with $R_i = |\boldsymbol{R}_i|$, $\mu_{\text{eff},i}$ is the effective magnetic moment of the ion i and m_i^α is the direction cosine of that moment along direction α [26, 120]. The Lorentz radius was chosen to be at least $50c$ since this produced results at the muon stopping site which converged to within 0.01 T of those obtained using $100c$ and $150c$.

In general, two further terms may contribute to the total magnetic field due to the presence of the magnetic sample outside of the Lorentz sphere (see Sec. 2.3). Firstly, the Lorentz field $\boldsymbol{B}_{\text{L}} = \mu_0 \boldsymbol{M}/3$ (where $\boldsymbol{M}$ is the bulk magnetisation) is the field at the site of interest due to the magnetic dipole moments lying outside of the Lorentz sphere. Secondly, the demagnetising field $\boldsymbol{B}_{\text{dem}} = -\mu_0 \sum_j \text{N}_{ij} M_j$ (where N_{ij} is the demagnetising tensor) arises from magnetisation induced at the surfaces of the sample [7]. Since an AFM structure has no net magnetisation $\boldsymbol{M}$, neither of these terms need to be considered here.

This procedure allows the calculation of $B_\mu \equiv |\boldsymbol{B}(\boldsymbol{r}_\mu)|$, the magnitude of the magnetic field at the muon stopping site in SFOO, using spin orientations and moment sizes from reference [101], for the AF1 phase with the $T = 75$ K values of the magnetic moments [$\mu(\text{Fe}) = 1.83\mu_{\text{B}}$, $\mu(\text{Os}) = 0.48\mu_{\text{B}}$]. Within the AF1 phase, moments residing on nn ions within the ab-plane are aligned antiparallel to one another, and the spin sequence along the c-axis is ↑↑↑↑. This calculation yields $B_\mu = 0.21$ T for the undistorted unit cell, where no perturbations owing to the presence of the muon have been included, and $B_\mu = 0.16$ T for the distorted crystal structure, where muon induced perturbations from the DFT relaxation procedure are included. The experimentally observed value of B_μ may be deduced using the fitting function, Eq. 3.5, which yields $\nu(T = 75 \text{ K}) = 49(1)$ MHz, or equivalently $B_{\mu,\text{exp}} = 0.36(1)$ T. Figure 3.13(a) shows the simulated values of $|\boldsymbol{B}|$ within the

ab-plane (for the $c = 1/2$ cross section of the undistorted unit cell) containing the calculated muon stopping site, indicated by the white cross, plus the contours corresponding to the experimentally observed value $B_{\mu,\mathrm{exp}}$. Although the agreement between $B_{\mu,\mathrm{exp}}$ and B_μ shows a discrepancy, it is clear from Fig. 3.13(a) that the proposed muon stopping site r_μ lies in a region where $|B(r)|$ is rapidly changing with r, and that the proposed muon site sits very close to the indicated contours corresponding to $B_{\mu,\mathrm{exp}} = 0.36(1)$ T for the undistorted unit cell.

It is therefore concluded that the proposed muon site is plausible for SFOO. The discrepancy between the simulated B_μ and $B_{\mu,\mathrm{exp}}$ is larger for the simulated dipole fields within the distorted unit cell configuration. However, a potential pitfall of this calculation is that all unit cells within the Lorentz sphere will also be distorted, whereas in reality it is expected that the degree of distortion should decay rapidly with distance from the muon site. The long ranged nature of dipole fields means this could have a significant impact on the simulated value of B_μ, particularly since r_μ sits in a region of rapidly changing field strength, as discussed above. It is also noted that this approach assumes the magnetic field at the muon site is entirely dipolar, and neglects any hyperfine field coupling arising from spin-polarised electron density overlapping with the muon's wavefunction (this contribution is expected to be small for insulating systems such as these [23, 25–27, 107]). Uncertainty in the moment sizes of each magnetic species adds further scope for discrepancy between simulated and observed magnetic field strengths.

Magnetic dipole fields within SYOO and SIOO were also calculated using the AFM spin configuration previously determined via NPD measurements [105]. Magnetic moments are currently understood to assume a type I AFM arrangement, comprising alternating layers of ferromagnetically aligned spins, with adjacent layers along the crystallographic *c*-axis having opposite directions of spin polarisation. NPD data have constrained the directions of the Os magnetic moments to lie within the *ab*-plane, but have not resolved their exact orientations since the monoclinic distortion is small, and a and b are very nearly equal [105] (the same situation is encountered in the related compound Sr_2ScOsO_6 where the B site is occupied by the $3d^0$ Sc^{3+} ion [105, 121]). In order to approximate candidate muon stopping sites in these compounds, which

Compound	$\boldsymbol{m}$	Site	$|\boldsymbol{B}(\boldsymbol{r}_\mu)|$ (T)
Fe	AF1	$p1$ (undistorted)	0.21
($B_{\mu,\mathrm{exp}} = 0.35(1)$ T)	AF1	$p1$ (distorted)	0.16
	[010]	$p1$	0.29
	[010]	$p2$	0.13
	[100]	$p1$	0.13
Y	[100]	$p2$	0.29
($B_{\mu,\mathrm{exp}} = 0.227(1)$ T)	[110]	$p1$	0.28
	[110]	$p2$	0.28
	[1$\bar{1}$0]	$p1$	0.15
	[1$\bar{1}$0]	$p2$	0.15
	[010]	$p1$	0.28
	[010]	$p2$	0.12
	[100]	$p1$	0.12
In	[100]	$p2$	0.29
($B_{\mu,\mathrm{exp}} = 0.185(2)$ T)	[110]	$p1$	0.28
	[110]	$p2$	0.28
	[1$\bar{1}$0]	$p1$	0.14
	[1$\bar{1}$0]	$p2$	0.14

Table 3.1: Table of simulated B_μ values for SFOO within the distorted and undistorted unit cell. The results of simulations are also provided for SYOO and SIOO, for various orientations of the magnetic moments $\boldsymbol{m}$ within the ab-plane, calculated at the two candidate muon stopping sites $p1$ and $p2$. Experimentally determined magnetic field strengths $B_{\mu,\mathrm{exp}}$ (see main text) are also provided for comparison.

both crystallise in the monoclinic space group $P2_1/n$, two positions are considered. These are $p1 = (0.314, 0.130, 0.499)$ and $p2 = (0.130, 0.314, 0.499)$, i.e., the fractional co-ordinates of $\boldsymbol{r}_\mu$ determined for SFOO, plus the position obtained by exchanging the a and b co-ordinates. For these simulations the type I AFM spin structure was used, with moments oriented along various high symmetry directions within the ab-plane. Table 3.1 summarises the results, where effective magnetic moments and unit cell dimensions refined at low temperature were used for SYOO and SIOO

[$\mu(\text{Os}) = 1.91\mu_B$ and $\mu(\text{Os}) = 1.77\mu_B$, and $(5.78, 5.81, 8.18)$ Å and $(5.69, 5.70, 8.05)$ Å, respectively], as reported in reference [105].

For magnetic moment orientations along either the a or b axes (the [010] orientation is proposed in reference [105]) these simulations predict the muon ensemble would experience two distinct magnitudes of local magnetic field B_μ [Fig. 3.13(f) and Table 3.1]. This situation would give rise to two resolvable oscillatory components in the muon data. However, as discussed in Sec. 3.5.1, the data are well described by a single oscillatory component. In contrast, B_μ at the sites $p1$ and $p2$ have essentially identical dipole field strengths when the moments are oriented along diagonal directions within the ab-plane [Fig. 3.13(d) and (e)].

The μSR data lead to the consideration of the possibility of IC magnetic ordering within SYOO and SIOO. A muon ensemble residing at magnetically equivalent sites within a commensurate magnetic field texture would be expected to sample a field distribution comprising a narrow peak (as for the SFOO case). In contrast, a sinusoidally varying magnetic field strength (with IC wavevector) leads to muons sampling a magnetic field distribution $p_{\text{IC}}(B) \propto (B_{\max}^2 - B^2)^{-1/2}$ for fields $B < B_{\max}$ (and zero otherwise). Since $p_{\text{IC}}(B)$ is peaked towards $B_{\max}$ [Fig. 3.11(a)], and at long times the Bessel function $J_0(\gamma_\mu B_{\max} t) \approx (1/\sqrt{x})\cos(\gamma_\mu B_{\max} t - \pi/4)$, comparison to the simulated B_μ values for commensurate ordering is physically justifiable. The absolute agreement between simulated values of [110] and [1$\bar{1}$0] B_μ and the observed value $B_{\mu,\text{exp}}$, calculated using the zero-temperature oscillatory frequency ν_0 from the Bessel function fitting procedure (0.227(1) T and 0.185(2) T for SYOO and SIOO, respectively), is reasonable. For instance, Fig. 3.13(d) shows that the candidate muon sites lie in very close proximity to the contours corresponding to $B_{\mu,\text{exp}}$ for the case where magnetic moments lie (anti)parallel to the [110] or $\boldsymbol{a} + \boldsymbol{b}$ direction within SYOO.

3.7 Conclusion and Further Work

In conclusion, the results of this μSR study have helped elucidate the intriguing magnetic behaviour within the double perovskites Sr_2CoOsO_6 and Sr_2FeOsO_6, and

suggest the possibility of incommensurate ordering within Sr_2YOsO_6 and Sr_2InOsO_6.

In conjunction with neutron diffraction and AC susceptibility, μSR has revealed two antiferromagnetic phases in SCOO upon cooling from room temperature. Below T_{N1} the average moments of dynamically fluctuating Co and Os spins order within the ab-plane, which leads to a fast relaxation component within the μSR asymmetry spectra, but precludes the observation of coherent muon-spin precession. Below T_{N2} the Co moments freeze into a noncollinear arrangement, while the Os moments continue to fluctuate. A sharp increase in the non-relaxing asymmetry amplitude upon cooling through $T \approx 5$ K reflects a greater static component within the magnetism, and supports a picture where the Os moments freeze into a randomly canted state.

In addition, this work has confirmed the magnetic ordering temperature $T_N = 135(2)$ K for SFOO, where the disappearance of oscillations in the muon asymmetry data for $T \leq T_2$ reveals a broader internal magnetic field distribution indicating coexistence of the antiferromagnetic phases AF1 and AF2, rather than a straightforward transition between the two phases. DFT calculations provide a candidate muon stopping site which dipole field simulations show to be consistent with the experimental results.

The Néel temperatures determined using μSR data for SYOO and SIOO are in excellent agreement with those previously obtained using molar magnetic susceptibility $\chi_m(T)$ and specific heat capacity $C_p(T)$ data [105]. However, within both the SYOO and SIOO systems these μSR measurements produce evidence for an incommensurate component to the magnetism, which was not observed in previous neutron powder diffraction experiments.

Another crystal structure where geometric frustration is fundamental to the magnetic behaviour is the pyrochlore lattice (a 3D extension of the 2D kagome lattice), which in some instances may exhibit a spin liquid state [73, 122]. Certain members of the pyrochlore family have been shown to possess a novel spin ice state [123, 124], with a macroscopically degenerate ground state analogous to the behaviour of protons in water ice. The spin ice state hosts exotic excitations which behave as emergent magnetic monopoles [125, 126] and undergo a liquid–gas phase

transition under applied magnetic fields. A μSR study of these excitations was able to directly observe the motion of these monopoles (so called 'magnetricity') and derive the elementary unit of magnetic charge [127].

4

Local Magnetism and Magnetostructural Behaviour in CsCoO$_2$

This chapter shall present the results of ZF muon-spin relaxation measurements investigating the structural and magnetic transitions in the tetrahedral spin-chain oxide CsCoO$_2$. This system exhibits strongly coupled long-range antiferromagnetic order at temperatures below the remarkably high Néel temperature $T_\mathrm{N} = 424$ K, comprising an antiferromagnetic arrangement of ferromagnetically ordered Co-Co spin dimers. The μSR data complement neutron powder diffraction and density functional theory studies, and help elucidate the nature of the magnetostructural coupling in the vicinity of a structural phase transition around $T^* = 100$ K. The importance of a bifurcation of corner-shared Co–O–Co bond angles is discussed, which causes a weakening of the superexchange interaction for one set of bonds along the chains, and consequently induces a complex freezing out of relaxation

processes upon cooling. Through a combination of magnetic dipole field simulations and Bayesian analysis probability density functions are generated for the ordered magnetic moment size (using observed muon-spin precession frequencies) and are able to confirm that the muon data are fully consistent with reported magnetic spin arrangements and ordered magnetic moment sizes. This chapter is based on work published in Ref. [128].

4.1 Introduction

4.1.1 Oxocobaltates

Layered oxocobaltates continue to attract significant research interest due to the rich variety of magnetic and electronic properties that they display, which in turn may be exploited within useful applications. For instance, $LiCoO_2$ has been used extensively as a cathode material within rechargeable Li ion batteries [129–131], thanks to its high energy density. The thermoelectric $NaCo_2O_2$ has a large Seebeck coefficient [132–135], enhanced by the spin entropy contribution to the Peltier effect [136]. More recently, unconventional superconductivity has been observed in $Na_xCoO_2 \cdot y(H_2O)$, for the first time in a non-cuprate layered $3d$ transition metal oxide [137–140]. This is a particularly exciting development since the superconductivity arises as the system is doped away from a Mott insulating ground state within the CoO_2 layers, in analogy to the cuprates, despite the triangular lattice geometry.

Complex phase diagrams arise in oxocobaltates due to the interplay between charge, spin and orbital degrees of freedom. A delicate energetic balance between Hund's rule exchange energy (favouring high-spin states) and crystal field splitting (inducing low-spin states) determines the electronic configuration of Co ions within oxide materials, providing scope for tunability of magnetic properties. There is a relative paucity of Co(III) oxocobaltates, as the absence of a pure and stable Co(III) oxide hinders sample synthesis. Historically, an octahedral geometry for compounds containing $3d^6$ Co^{3+} ions is most commonly realised, where strong crystal field splitting leads to the low-spin $(t_{2g}^6 e_g^0)$ $S = 0$ configuration, shown in Fig. 4.1 (a) [141]. This explains the observation of a diamagnetic ground state in $LiCoO_2$ [129]
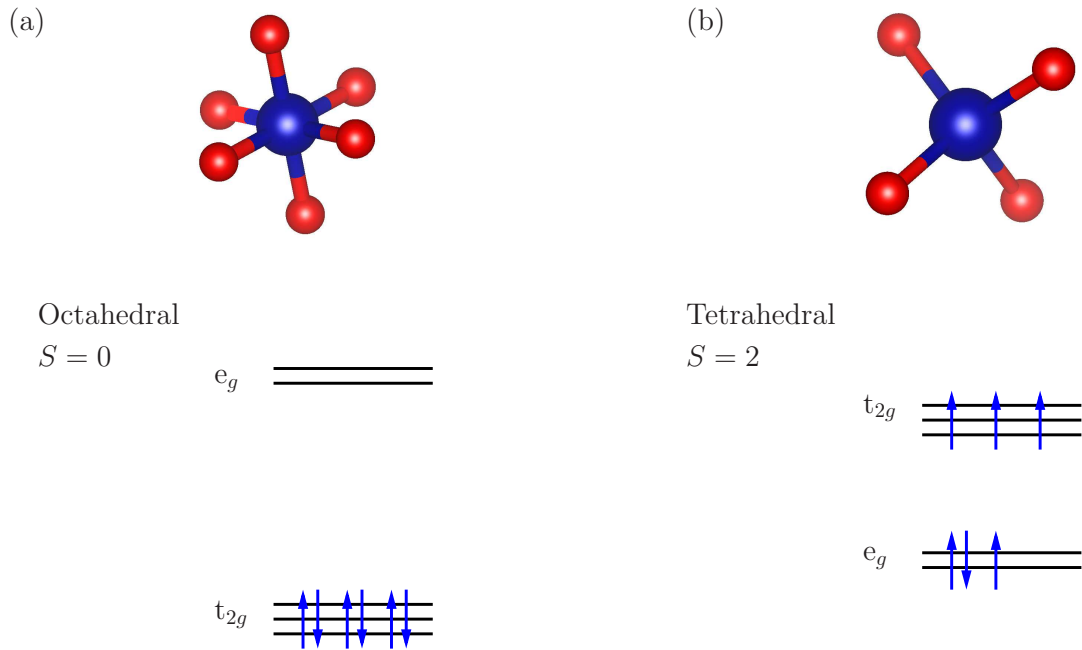
Figure 4.1: $3d^6$ electronic configuration and resulting spin state for Co^{3+} ions (blue) coordinated in two oxygen ion (red) environments. (a) Strong crystal field splitting in the octahedral case leads to the low-spin state $S = 0$, whereas (b) weak crystal field splitting in the tetrahedral case leads to the high-spin state $S = 2$.

and temperature-independent paramagnetism in $M\text{CoO}_2$ for $M = \text{Na}, \text{Ag}$ [132, 142], where the Co layers comprise networks of edge-sharing distorted octahedra.

In contrast, a tetrahedral environment with weaker crystal field splitting favours the high-spin $(t_{2g}^3 e_g^3)$ $S = 2$ configuration [see Fig. 4.1 (b)] for Co^{3+} [143]. These tetrahedra may be magnetically isolated [144, 145], or share a common edge to form the anion Co_2O_6^-. In this latter case $S = 2$ Co ions align ferromagnetically within each dimer, which themselves order antiferromagnetically below 30 K [145]. The novel oligomer $\text{Co}_4\text{O}_{10}^{10-}$ may be formed by attaching a planar CoO_3 triangle (containing $S = 3/2$ Co^{2+} ions) to either end of the Co_2O_6^- dimer, fostering unusual magnetic exchange interactions [146, 147].

4.1.2 CsCoO₂ and Previous Characterisation

The oxocobaltate CsCoO_2 has recently been synthesised with a unique crystal structure, containing tetrahedrally coordinated Co^{3+} ions. Here, extended buckled CoO_2 layers comprise dimers of edge-sharing CoO_6 tetrahedra which are then connected in
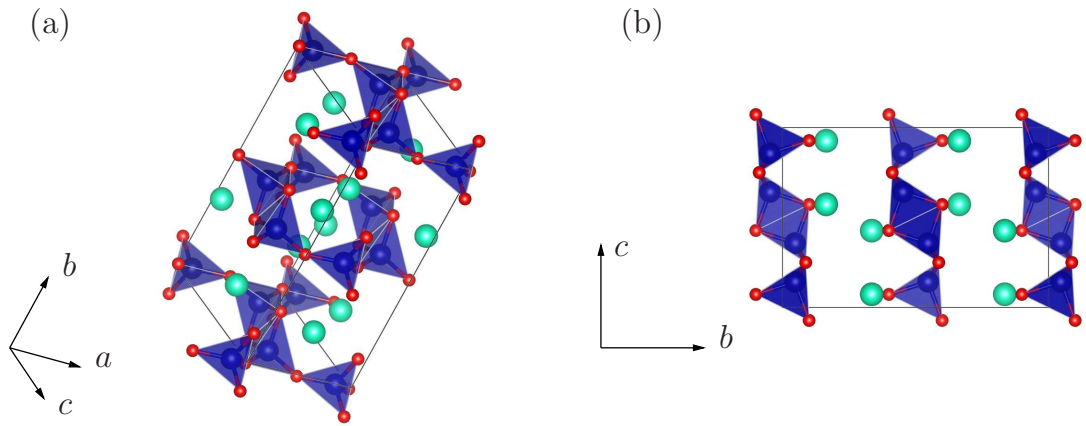
Figure 4.2: Illustration of the chemical structure of $CsCoO_2$ depicting the high-temperature orthorhombic β phase refined at 300 K [128, 148]. Co (blue), O (red) and Cs (green) ions are shown. Orientations highlighting (a) the arrangement of tetrahedra within the CoO_2 layers, and (b) the separation of the layers along the b-axis.

corner-sharing chains along the crystallographic a-axis, as shown in Fig. 4.2. This structure was previously believed to be precluded for oxides due to repulsion of the cations across the shared edge [149]. Charge neutrality is provided by caesium ions lying between the cobalt layers, whose structure repeats in neighbouring layers, albeit offset by a $(0.5, 0.5, 0)$ translation.

Single crystals were grown (by M. Jansen and colleagues in Dresden and Stuttgart) using the azide/nitrate route [150] and were subsequently characterised by single crystal x-ray diffraction [148], the results of which reveal a structural transition at $T^\star \approx 100$ K. This observation explains the appearance of anomalous features within heat capacity data, indicative of a transition with little associated entropy change. Upon cooling below $T^\star$ a displacive structural phase transition occurs, where tilting of the tetrahedra drives a transition from the high-temperature orthorhombic $Cmca$ space group (denoted the β phase) to the lower symmetry, monoclinic $C2/c$ space group (α phase). This is a second order displacive transition, accompanied by a sharp but continuous variation in the monoclinic angle β [128].

The interesting superexchange pathway network within the CoO_2 layers afforded by the crystal structure features two categories of Co–Co spin coupling mechanisms. The Goodenough Kanamori Anderson (GKA) rules [92–94] predict *interdimer* coupling for Co spins between neighbouring tetrahedra to be antiferromagnetic. This

superexchange pathway is mediated via corner-shared oxygen ions (denoted O2), with a Co–O2–Co bond angle comparable to the linear arrangement of 180°. In contrast, the *intradimer* pair of Co ions are coupled via the two oxygen ions occupying the shared edge (denoted O1), with Co–O1–Co bond angles of nearly 90°. This arrangement of orbital overlap between Co 3d and O 2p orbitals would be expected to give rise to a ferromagnetic exchange coupling between cobalt spins.

Bulk magnetic characterisation has identified the onset of antiferromagnetic ordering below the notably high Néel temperature $T_{\mathrm{N}} \approx 420$ K, [128, 148] which is indicative of unusually large exchange interactions present in the system. The magnetic transition is visible as a pronounced feature in magnetic susceptibility measurements, which may be emphasised by deriving the magnetic heat capacity via $C_{\mathrm{m}} \propto A\frac{d(\chi T)}{dT}$ where $\chi(T)$ is the magnetic susceptibility and A is only weakly temperature dependent (the 'Fisher heat capacity method' [151]). The susceptibility is seen to be temperature independent above the ordering temperature, which reflects persisting strong exchange coupling between Co spins. Differential scanning calorimetry (DSC) measurements reveal an enthalpy change ΔH indicating an endothermic transition occuring around T_{N}, consistent with AFM ordering. All of these measurements display hysteresis effects: the ordering temperature is shifted downwards in data taken upon cooling relative to data taken upon warming ($\Delta T \approx$ 15 K). The rest of this discussion shall focus on data taken on warming. Susceptibility measurements also display anomalous behaviour around the structural transition temperature $T^{\star} \approx 100$ K (together with strong hysteresis in this temperature region).

Neutron Powder Diffraction (NPD) measurements shed some light on the relationship between crystal and magnetic spin structures around $T^{\star}$ [128]. Rietveld refinement of NPD data is able to elucidate the magnetic spin structure in both the α and β phases. It should be noted that the time scales probed by elastic neutron diffraction techniques are typically of order 10^{-11} s, which will be discussed in greater detail below. The results indicate that the same magnetic spin arrangement is present in the magnetic long range order (LRO) above and below $T^{\star}$. Diffraction peaks corresponding to the magnetic ordering of Co spins split in the same manner as the nuclear intensities as the system's symmetry is lowered upon cooling into the
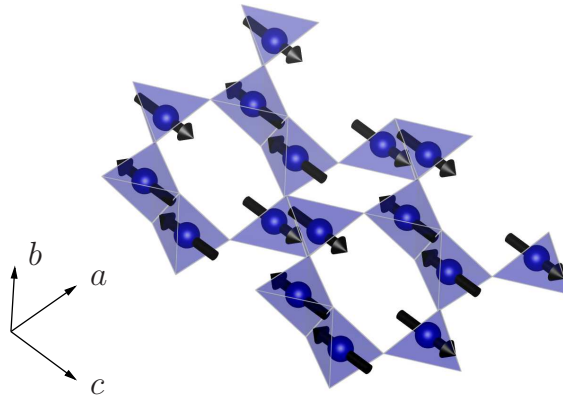
Figure 4.3: Experimentally determined magnetic structure of a single CoO_2 layer within β-$CsCoO_2$ (O and Cs ions have been omitted for clarity). This ground state spin structure, comprising ferromagnetically aligned dimers themselves arranged antiferromagnetically within the ac-plane, is believed to remain unchanged across the structural transition observed at $T^\star$.

monoclinic α phase.

The inferred magnetic spin structure is shown in Fig. 4.3. The structure is most readily understood as ferromagnetically ordered Co-Co dimers (occupying edge-sharing tetrahedra) which are tiled in an antiferromagnetic arrangement within each CoO_2 layer. 'Nearest-neighbour' dimers within the ac-planes (along the diagonal $\boldsymbol{a}+\boldsymbol{c}$ and $\boldsymbol{a}-\boldsymbol{c}$ directions) are polarised antiparallel to one another. This magnetic ordering is present in each cobalt layer, where adjacent layers are simply offset by the same $(0.5, 0.5, 0)$ translation as the crystal unit cell. Symmetry considerations concluded that magnetic moments are orientated along the crystallographic c-axis, with relatively low magnitudes for the ordered magnetic moments of $3.089\mu_B$ (2 K) and $2.628\mu_B$ (300 K) per Co^{3+} for α- and β-$CsCoO_2$, respectively. The suppression of the Co^{3+} magnetic moment, with respect to the spin-only value of $4\mu_B$, was attributed to strong $Co(3d)$–$O(2p)$ hybridisation [128].

4.2 μSR Measurements

4.2.1 Experimental Procedure

Muons are a sensitive local probe of both static and dynamic magnetism and therefore allow the study of the critical behaviour near T_N, dynamics of magnetic fluctuations
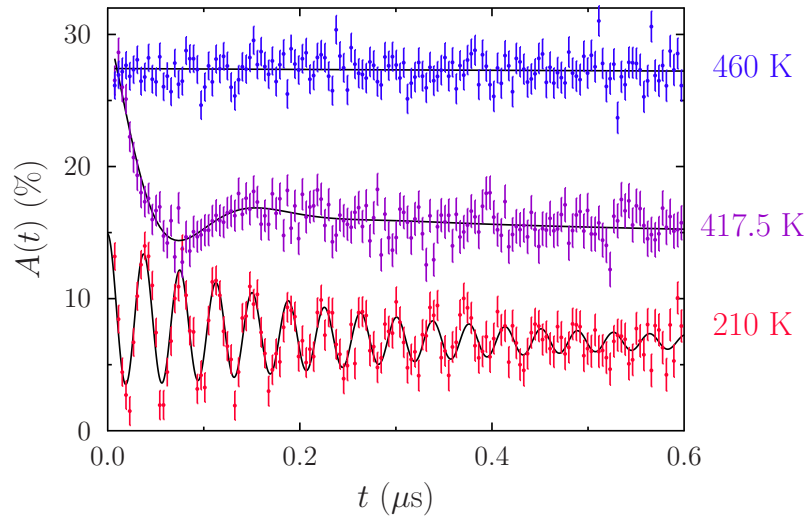
Figure 4.4: $A(t)$ spectra, showing single-frequency oscillations in the ordered regime with a fit to Eq. 4.2, as described in the text (the 210 K data are offset by -10% for clarity).

and interplay between the magnetic and crystallographic structures around $T^\star$. In order to probe the local magnetism on a time scale distinct from that measured by NPD, μSR measurements were made on a polycrystalline $CsCoO_2$ sample. Zero-field (ZF) μSR measurements were made using the GPS instrument at the Swiss Muon Source (SμS). The $CsCoO_2$ powder was loaded into a bespoke titanium sample holder (manufactured in the Durham physics mechanical workshop) in an argon-filled glovebox, covered with 25 μm Ti foil and made air-tight with a knife edge seal. Data were collected on heating between 10 and 460 K using a Janis closed cycle refrigerator (CCR) with a Sumitomo Heavy Industries cold-head. Temperature control is achieved through ^{4}He exchange gas for $T \leq 300$ K and a 'hot-finger' arrangement for $T \geq 300$ K.

4.2.2   Results

Spontaneous oscillations in the asymmetry spectra measured in zero-field are clearly visible for temperatures below around 420 K, as shown in Fig. 4.4. This constitutes unambiguous evidence of quasi-static magnetic LRO throughout the bulk of the material.

A clear indication of the transition temperature is given by considering the time-averaged asymmetry $\overline{A} \equiv \langle A(t \leq 9.5 \ \mu s) \rangle$, which drops abruptly upon cooling,
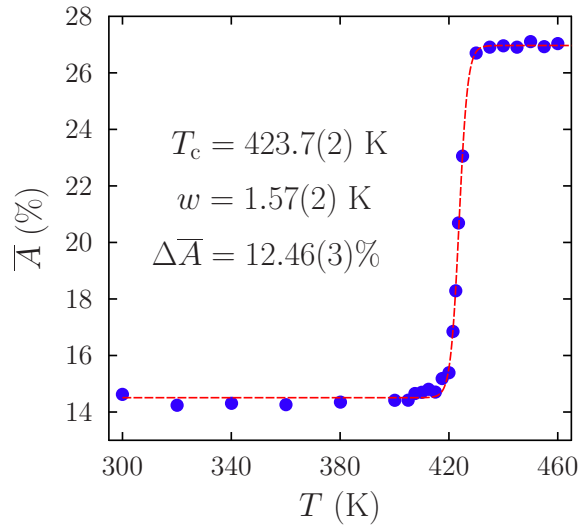
Figure 4.5: Time-averaged asymmetry near the critical region, displaying an abrupt drop in average asymmetry $\Delta\overline{A} \equiv A_2 - A_1$. The dashed line is the fit to Eq. 4.1.

where asymmetry is lost as the material enters the magnetically ordered state. Asymmetry data measured above T_N show very little relaxation, consistent with 'motional narrowing' of rapidly fluctuating electronic magnetic moments from the signal, leaving only weak depolarisation due to weak nuclear dipole fields. Within the ordered state, however, large quasi-static magnetic fields lead to rapid depolarisation of the muon ensemble. Fig. 4.5 shows this drop in average asymmetry, which may be fitted with a Fermi-like step function

$$\overline{A}(T) = A_2 + \frac{A_1 - A_2}{e^{(T-T_c)/w} + 1}, \tag{4.1}$$

providing a method for extracting the transition temperature by parametrising the continuous step from high- (low-) T asymmetry A_2 (A_1) with mid-point T_c and width w [104]. The fit yielded values of $T_c = 423.7(2)$ K and $w = 1.57(2)$ K, giving $T_N = T_c \pm w = 424(2)$ K in agreement with the value previously obtained by other methods.

Asymmetry spectra below T_N were best fitted with the single-frequency oscillatory relaxation function

$$A(t) = A_{\text{osc}} \cos(2\pi\nu t)e^{-\lambda_{\text{osc}}t} + A_{\text{rel}}e^{-\lambda_{\text{rel}}t} + A_{\text{b}}, \tag{4.2}$$

where the oscillating amplitude A_{osc} was fixed to its average value of 5.7%. The non-relaxing baseline contribution A_{b} is attributable to muons which stop in the Ti

sample holder, and, more importantly, to the non-precessing component of muon spins which lie parallel to the local magnetic field. Parameters resulting from this fit are displayed in Fig. 4.6.

Upon cooling below T_N, the precession frequency ν increases in the expected manner [Fig. 4.6(a)], and the relaxation rates $\lambda_{osc,rel}$ peak, as is typical for an AFM phase transition [Fig. 4.6(c,d)]. The Larmor precession frequency of the muon ensemble is related to the average magnitude of the magnetic field B at the muon site via $2\pi\nu = \gamma_\mu B$. Here B, and hence ν serves as an effective order parameter for the LRO. Frequencies in the critical region 400 K $\leq T < T_N$ were therefore fitted to

$$\nu(T) = \nu_0 \left(1 - T/T_N\right)^\beta, \tag{4.3}$$

where $T_N = 424$ K was fixed, and $\nu_0 \equiv \nu(T = 0$ K$)$ [3,7]. The fit yielded a value for the critical exponent $\beta = 0.35(2)$, which is consistent with that expected for a 3D Heisenberg antiferromagnet. The value of the critical parameter β for a given set of fitted frequencies ν was found to be sensitive to the time range over which the asymmetry spectra were fitted, the quoted value was obtained for fits to asymmetry data from early times ($t \leq 1$ μs), which are most sensitive to the behaviour of the oscillations. Values of β and T_N remained unchanged (to within uncertainties) when the critical temperature was also allowed to vary within the fit. It is beneficial to present the outcome of this fitting procedure in a logarithmic plot, since taking the logarithm of Eq. 4.3 yields

$$\log \nu = \log \nu_0 + \beta \log \left(1 - T/T_N\right), \tag{4.4}$$

which is simply a linear fit, with gradient given by the critical exponent. This plot is shown in Fig. 4.7, where the good linearity of the fitted data points (shown in solid blue) vindicates the choice of the critical temperature range and the fixed value of T_N.

4.3 Discussion

In addition to the behaviour observed around T_N described above, which is quite typical for an AFM transition, it is apparent that on cooling though the region
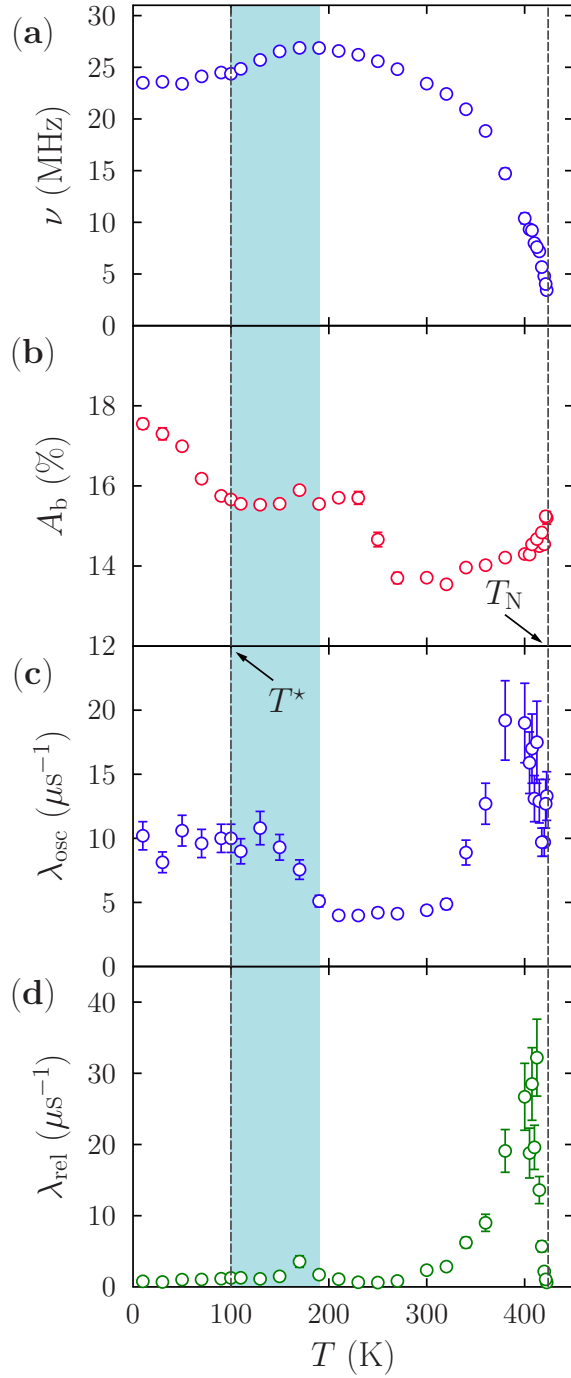
Figure 4.6: Fitted parameters to the oscillatory relaxation function Eq. 4.2 for all asymmetry data ($t \leq 9.5~\mu$s) for temperatures $T < T_N$. (a) Frequency ν, (b) baseline asymmetry A_b, (c) transverse and (d) longitudinal relaxation rates λ_{osc} and λ_{rel}, respectively. Dashed lines indicate the Néel temperature $T_N = 424$ K and the structural phase transition temperature $T^\star \approx 100$ K. The anomalous temperature region $T^\star \lesssim T \lesssim 190$ K is shaded.
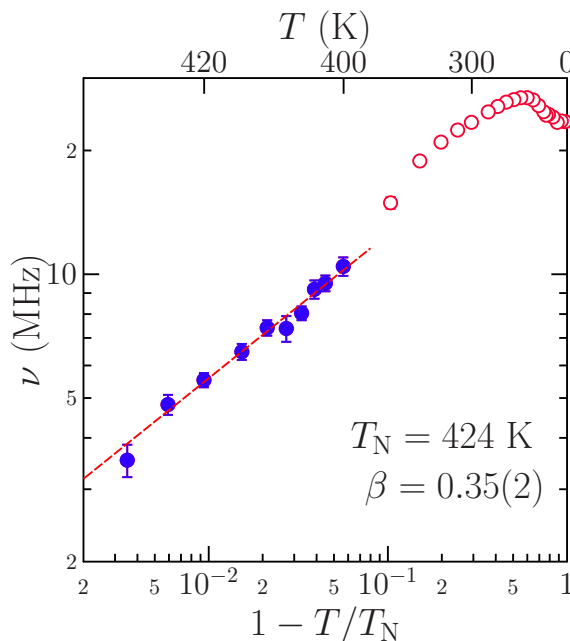
Figure 4.7: Scaling plot for the order parameter ν. The dashed red line shows the fit to Eq. 4.3 for the data points displayed with solid blue circles.

$T < T_{\rm N}$, there are a number of additional, notable features in the μSR data. On cooling below ≈ 190 K the muon precession frequency ν is smoothly suppressed [Fig. 4.6(a)]. No discontinuities are observed in the fitted parameters around this temperature, consistent with the picture of a broad, virtually second order structural transition. This is accompanied by a steady increase in $\lambda_{\rm osc}$, such that $\lambda_{\rm osc}$ is larger by a factor of about 2 below $T^{\star}$ than in the region 200 K $\lesssim T \lesssim$ 300 K [Fig. 4.6(c)]. Below $T^{\star} \approx 100$ K, $\lambda_{\rm osc}$ and ν both level off at constant values. The decrease of ν below 200 K indicates a reduced value of average magnetic field strength experienced at the muon stopping sites. In the fast fluctuation limit it is expected that the relaxation rate $\lambda \propto \langle (B - \langle B \rangle)^2 \rangle \tau$ (i.e., the second moment of the magnetic field distribution multiplied by the correlation time τ [36]) and so the additional dephasing indicates a broadening of the distribution of static magnetic field strengths experienced by the muon ensemble, or an increased correlation time as relaxation channels freeze out on the muon time scale (see Sec. 2.4.4). It is possible that this behaviour reflects the system exploring some of the energetically similar magnetic states predicted by the DFT calculations described in Sec. 4.3.1, below. These states are realised by flipping the overall spin of a dimer, while preserving their FM

intradimer spin configuration [Fig. 4.8(b)]. Although this could conceivably lead the muon ensemble to experience a broader static magnetic field distribution, with a lower mean field strength, one would expect this to occur below $T^\star$ rather than above it. Moreover, the refined cobalt moment sizes from NPD data [128] do not show this suppression below 200 K, suggesting that the effect could be dynamic and related to the issue of time scale. Such effects are therefore not seen in the neutron measurements as these effectively take a 'snapshot' of the spin distribution, when compared to the muon GHz time scale (determined by the muon gyromagnetic ratio γ_μ, see Sec. 2.2.3).

Additional evidence for the influence of dynamics comes from the baseline asymmetry A_b, which increases abruptly at around 250 K and upon further cooling below $T^\star$ gradually increases further [Fig. 4.6(b)]. Since relaxation of those muon spins that initially point along the direction of the local magnetic field can only be achieved by dynamic relaxation precesses, the increase of such a non-relaxing signal is usually indicative of a freezing of relaxation processes. There is therefore have evidence for an initial, abrupt freezing of some relaxation channels around 250 K, prefiguring the suppression of the precession frequency ν, with a further, smooth increase below 100 K that seems to track the size of the monoclinic distortion as indicated by both the change in unit cell angle β and the splitting of the corner-shared bond angle Co–O2–Co (obtained via crystal structure refinements of NPD datasets [128]). This monoclinic distortion leads to a disproportionation of the corner-shared oxygen Co–O2–Co bond angles: above $T^\star$ there is one unique value of about 150°, whereas below there appear two distinct classes of bond with angles of around 140° and 155°. These values lie within the linear GKA rule regime, but not particularly close to the fully linear angle of 180° (which leads to strong AFM coupling), and so suggest a relatively weak AFM interdimer exchange interaction strength.

In contrast, the edge-shared Co–O1–Co intradimer bond angle only slightly deviates from 90° both above and below $T^\star$ (88° and 86°, respectively [128]) and therefore displays a strong FM superexchange interaction as expected from GKA. There are also no significant changes in the Co–O average bond distance. It is possible that this temperature independence of the average Co–O bond distances and

of the Co–O1–Co bond angles via the edge-shared oxygen atoms is what makes the magnetic ordering so robust with respect to the structural phase transition occurring at $T^\star$. The weaker AFM interdimer coupling drives the transition to LRO, and so the system would be sensitive to the bifurcation of the corner-shared oxygen bond angle below $T^\star$, where the AFM exchange interaction strength J' would also split into two unequal values. When these superexchange pathways become inequivalent in the monoclinic phase it is possible that this allows some relaxation channels to freeze out, leading to a greater static component of the magnetic field, and hence the increase in non-relaxing asymmetry A_b observed.

4.3.1 Density Function Theory Calculations

In order to further resolve a microscopic picture of the possible static magnetic structures, derive a low energy model of superexchange spin interactions and elucidate any magnetic changes accompanying the structural transition, density functional theory (DFT) calculations were performed by Stewart Clark, Durham University [128]. Total energy calculations using the CASTEP code [117,118] enabled a systematic search to be performed to categorise the possible AFM structures. In agreement with the NPD results, the lowest energy configuration for both the α and β phases was found to have strongly ferromagnetically aligned Co-Co dimers, with weaker antiferromagnetic order along the Co chains parallel to the crystallographic a-axis [Fig. 4.8(a)]. The weak AFM interdimer interaction can be easily flipped, as illustrated in Fig. 4.8(b), at an energy cost of $\Delta E \approx 0.034$ eV/"bond" (for the low-T, α phase). This energy cost may be related to the exchange interaction strength J within the Heisenberg Hamiltonian term for a single exchange bond $\hat{\mathcal{H}} = -J\hat{\boldsymbol{S}}_1 \cdot \hat{\boldsymbol{S}}_2$ (employing the single-J convention) via $\Delta E = (1/2)JS_{\uparrow\uparrow}(S_{\uparrow\uparrow} + 1)$, where $S_{\uparrow\uparrow} = 2S$ is the spin quantum number of the dimer triplet state. For Co^{3+} in the high-spin state, $S = 2$ and therefore $J = \Delta E/10$. Hence the exchange constant for the weak AFM pathway along the corner-shared O^{2-} ion is predicted to be $J' = -39(1)$ K. The ferromagnetic intradimer coupling (via the edge-shared oxygen superexchange pathway) is far stronger. The triplet-singlet energy difference between these Co spins was found to be $\Delta E \approx 0.44$ eV, corresponding to an exchange strength of $J = 511(1)$ K
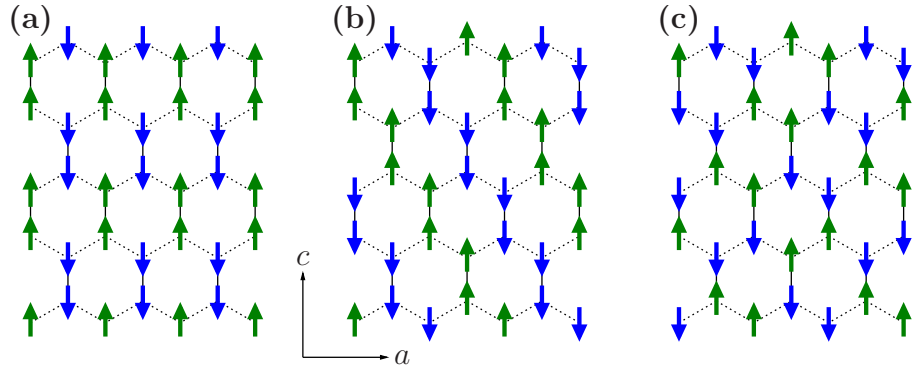
Figure 4.8: (a) Experimentally observed spin structure formed by the Co ions. (b,c) Example higher energy spin structures. The Co ions interact via edge-shared oxygen intradimer (solid line) and corner-shared interdimer (dashed line) superexchange pathways.

[Fig. 4.8(c)]. There are a number of possible AFM states analogous to Fig. 4.8(b) (which preserve the FM intradimer spin configuration) that are close in energy and likely to be populated via thermal fluctuations. Ordered moment sizes (constrained to be collinear) were found to be $3.25\mu_B$ per Co ion, with some spin density transferred onto the edge-shared oxygen ions ($1.2\mu_B$ per ion), in good agreement with the low-T value obtained through NPD refinements.

Additional insight into the unusually large intradimer exchange coupling was provided by Mulliken analysis, where valence electron wave functions are projected onto an atomic orbital basis set. This analysis found that, although the corner-shared oxygen O2 sites carry no net spin, the edge-shared oxygens (O1, which link Co ions within a dimer) are significantly spin polarised. This is indicative of an enhanced superexchange coupling within the dimers.

4.4   Muon Site Analysis

4.4.1   Dipole Field Calculations

Dipole field calculations were performed in order to gain insight into the internal magnetic field distributions in $CsCoO_2$, and investigate potential muon stopping sites within its crystal unit cell. By considering both the α and β phases, it may be possible to determine whether the structural transition at $T^\star$ leads to a relocation

of the muon with respect to the Co magnetic moments, and whether this could be a plausible explanation for the observed suppression of the order parameter in Fig. 4.6(a).

The magnetic dipole field $\boldsymbol{B}_{\mathrm{dip}}(\boldsymbol{r}_\mu)$ at a muon stopping site $\boldsymbol{r}_\mu$ due to the coupling with localised magnetic moments $\boldsymbol{m}_i$ located at positions $\boldsymbol{r}_i$ is given by

$$\boldsymbol{B}_{\mathrm{dip}}(\boldsymbol{r}_\mu) = \frac{\mu_0}{4\pi} \sum_i \frac{3(\boldsymbol{m}_i \cdot \hat{\boldsymbol{r}}_{i\mu})\hat{\boldsymbol{r}}_{i\mu} - \boldsymbol{m}_i}{|\boldsymbol{r}_\mu - \boldsymbol{r}_i|^3}, \tag{4.5}$$

where μ_0 is the vacuum permeability, $\hat{\boldsymbol{r}}_{i\mu}$ the normalised vector between the muon and the moment $\boldsymbol{m}_i$ [26,120]. The dipolar interaction may be evaluated for an infinite sample by calculating the magnetic field given by Eq. 4.5 within a Lorentz sphere of finite radius r_{L}. The Lorentz sphere needs to be sufficiently large to reach satisfactory convergence of the calculated field. For the following calculations $r_{\mathrm{L}} = 42$ Å. For AFM spin configurations one does not need to consider additional contributions arising due to Lorentz or demagnetising fields, since there is no net magnetisation, as discussed in Sec. 3.6.

The calculation of dipole fields using Eq. 4.5 treats the magnetic moments of ions as dipoles which are localised at a point in space. In reality, the delocalised nature of electron wavefunctions implies that magnetic moments are in fact spread over finite regions of space, as evidenced by the transfer of spin density onto oxygen ions predicted by the DFT calculations in Sec. 4.3.1. One consequence of this effect is the possibility of contact hyperfine fields: an effective magnetic field arising from direct overlap between the muon wavefunction and electron spin density at the muon position $\boldsymbol{r}_\mu$, given by

$$B_{\mathrm{hyper}}(\boldsymbol{r}_\mu) = \frac{2\mu_0}{3\mu_{\mathrm{B}}} \left[n^\uparrow(\boldsymbol{r}_\mu) - n^\downarrow(\boldsymbol{r}_\mu) \right], \tag{4.6}$$

where $n^{\uparrow,\downarrow}(\boldsymbol{r}_\mu)$ are the electron densities corresponding to spin up and spin down wavefunctions, respectively [152]. The magnitude of this contribution is extremely difficult to predict since one would need to have prior knowledge of the muon site, and the ensuing perturbation the presence of the (positively charged) muon induces upon the electron density functional. Since $CsCoO_2$ is an insulator, with positively charged magnetic Co^{3+} ions of relatively small spatial extent, one might expect any hyperfine contact fields to be small in this instance.
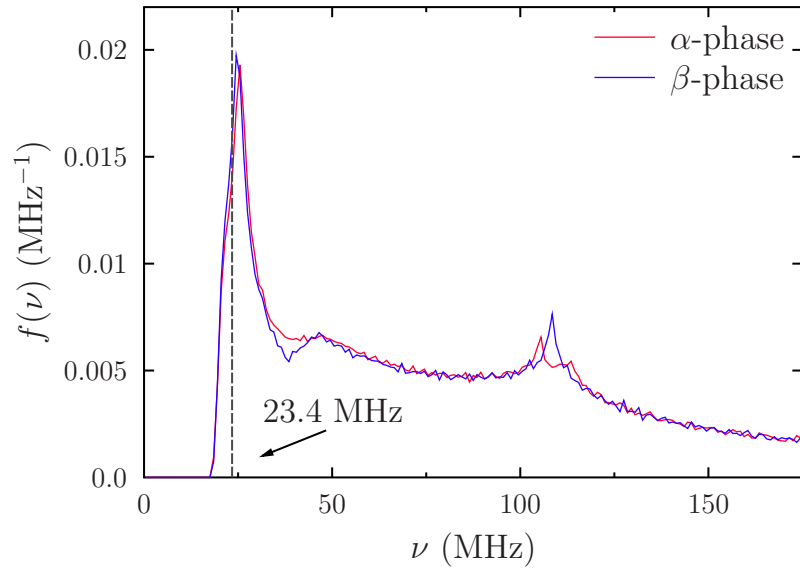
Figure 4.9: Precession frequency PDF (scaled for an ordered moment size $\mu = 2.63\mu_B$). Data are constrained to a limited volume fraction of the unit cell, as described in the text.

Dipole field simulations were performed on $CsCoO_2$ using the proposed magnetic spin structure and crystal parameters obtained from x-ray diffraction at 50 K and 296 K [148] (calculations were carried out using mμcalc [153]). If the magnetic field experienced by the muon is entirely dipolar (i.e., neglecting the contact hyperfine field) then the magnetic field calculated at any given site is proportional to the precession frequency of a muon situated there (via $2\pi\nu = \gamma_\mu B$). Therefore one may obtain the frequency (per unit moment size) probability density function (PDF) $f(\nu/\mu)$, both for the entire unit cell, and for a reduced volume fraction satisfying physically justified constraints on muon sites. The constraints applied were that a muon typically lies 1 Å away from an oxygen ion [154] ($0.9 \leq r_1 \leq 1.1$ Å) and won't come to rest too close a positively charged ion ($r_2 \geq 1$ Å), which together limit the calculations to a volume fraction of 5.93% of the entire unit cell. Dipole field magnitudes were evaluated on this subset of points decorating a regular grid of $N = 211^3$ points within the unit cell (a prime number of points in each direction is chosen since this helps reduce the risk of sampling artefacts). The magnitude of the magnetic field at all of the points are binned to produce a histogram, which is normalised by the number of points sampled N so that the histogram may be taken to be a PDF which is normalised to unity.

The observed precession frequency [Fig. 4.6(a)] at both 50 K (α phase) and 300 K (β phase) was 23.4 MHz. Neutron data indicates that the ordered moment size is $2.63\mu_{\rm B}$ at 296 K [148], and hence this value was used to scale both of the frequency PDFs shown in Fig. 4.9. The observed frequency $\nu = 23.4$ MHz is labelled, and the PDF has a clear peak lying very close to this value. Using this value of ordered moment size, a candidate muon site was located which lies approximately 1 Å from the corner-sharing oxygen ions, on the outside of the Co-O2-Co angle, which would give rise to the observed muon precession frequency (within both phases). The sharpness of the peak at $\nu \approx 25$ MHz (for both the α and β phases) suggests that it is a Van Hove singularity [155], corresponding to a point of high symmetry. Both PDFs also feature a characteristic ν^{-2} tail at high ν, which arises due to sites lying very close to a magnetic moment [since $f(\nu)\,d\nu \propto 4\pi r^2\,dr$ for a separation r from a single magnetic dipole, which taken together with $\nu(r) \propto r^{-3}$ yields $f(\nu) \propto \nu^{-2}$].

The close proximity of the peak in the simulated frequency PDFs, Fig. 4.9, to the experimentally observed muon-spin precession frequency (at both 50 K and 300 K) demonstrates good consistency between the muon data and the magnetic spin structure determined via NPD measurements and DFT calculations. The similarity between the simulated PDFs generated for both the α and β phase crystal structures also suggests there is no dramatic change in local magnetic field at the muon stopping site due to the structural transition around $T^\star$. However, in contrast to the observed muon-spin precession frequency [Fig. 4.6(a)], NPD measurements indicate that the ordered moment size μ increases monotonically upon cooling, with Rietveld refinement yielding a moment size $\mu = 3.2\mu_{\rm B}$ at 50 K [128]. In order to further scrutinise the implications of the simulated and observed data with respect to Co^{3+} moment sizes, we now turn to Bayesian analysis.

4.4.2 Bayesian Analysis of Precession Frequencies and Ordered Magnetic Moments

Bayesian inference is a method of inverting conditional probabilities [156, 157], allowing one to use experimental observations to quantitatively test a hypothesis. The application of Bayesian analysis to the field of μSR was developed by Blundell *et*

al. [158], and has previously only been applied to a select number of cases [104,159,160]. Before applying Bayesian analysis to the magnetic properties of $CsCoO_2$ it is useful to recap some basic principles of probability and consider the underlying mechanisms and assumptions behind this approach.

Conditional probability is denoted $P(A \mid B)$ and is the probability of some event A occurring, given that another event B has already occurred. In general, an observer may be able to employ a computational simulation in order to predict the probability of a particular experimental outcome O for a given hypothesis H, which may be expressed $P(O \mid H)$. For the case of a μSR experiment, one such experimental outcome could be the observed precession frequency ν (or set of frequencies ν_i) [158]. This seems a natural choice since frequencies are the most unambiguous parameter able to be extracted from zero-field μSR data, and may be directly related to local magnetic field strengths. The dipole field calculations presented in Sec. 4.4.1 are therefore a means of simulating an outcome from a μSR experiment using a computational approach, for a given hypothesis H. In this instance, the hypothesis H contains a multitude of assumptions, including the underlying spin configuration in the magnetic material, magnitudes of the ordered magnetic moments μ_i, the site(s) occupied by the implanted muon ensemble within the unit cell and the presence or magnitude of any other contributions to the local magnetic field at the stopping site. Once an observer has performed an experiment, and determined an empirical outcome O, then they may wish to evaluate how this new information should affect the probability of a given hypothesis H being true, i.e., they seek $P(H \mid O)$. Bayesian analysis provides a method of combining experimental evidence O and simulation $P(O \mid H)$ to evaluate confidence in one or more hypotheses H.

The *joint probability* $P(A \cap B)$ is the probability of events A and B both occurring, which may be calculated via

$$P(A \cap B) = P(A \mid B)P(B), \tag{4.7}$$

i.e., the probability of B occurring $P(B)$ multiplied by the conditional probability that A occurs given B already has. The choice of conditional probability on the

RHS of Eq. 4.7 is not unique, and so

$$P(A \cap B) = P(B \mid A)P(A), \tag{4.8}$$

is equally valid. Combining Eqs. 4.7 and 4.8 to eliminate the joint probability is all that is required to derive Bayes' theorem, usually expressed as

$$P(A \mid B) = \frac{P(B \mid A)P(A)}{P(B)}. \tag{4.9}$$

Here, $P(A)$ is called the *prior* probability, since it represents the probability of A occurring without any knowledge regarding the outcome of event B. The quantity to be calculated $P(A \mid B)$ is called the *posterior* probability.

For an exhaustive set of mutually exclusive events A_i, normalisation requires

$$\sum_i P(A_i) = 1, \tag{4.10}$$

i.e., some (non-specific) outcome is guaranteed. This permits the probability of some other event X to be expressed as

$$P(X) = \sum_i P(X \cap A_i) = \sum_i P(X \mid A_i)P(A_i), \tag{4.11}$$

since $P(X)$ is the sum of the joint probabilities of X and each possible outcome A_i occurring, and Eq. 4.7 has been used.

Thus far, only discrete random variables have been considered, however many physical parameters are continuous, for instance magnetic field strengths $|\boldsymbol{B}|$ (and therefore muon precession frequencies ν_i), and magnetic moment sizes μ_i. It is therefore useful to extend the above discussion to include continuous random variables. The normalisation condition Eq. 4.10 may be generalised to give

$$\int P(A') \, dA' = 1, \tag{4.12}$$

and one can therefore define the probability of some other (continuous) event X occurring as

$$P(X) = \int P(X \mid A')P(A') \, dA', \tag{4.13}$$

in analogy to Eq. 4.11. For the continuous variables ν and μ Bayes' theorem is therefore given by

$$P(\mu \mid \nu) = \frac{P(\mu)P(\nu \mid \mu)}{\int P(\nu \mid \mu')P(\mu') \, d\mu'}, \tag{4.14}$$

where ν is the observed precession frequency from the μSR experiment.

The prior in Eq. 4.14 is $P(\mu)$, the assumed PDF for the moment size before any information was deduced from the μSR experiment. A minimum assumption model is a uniform distribution from zero up to a cutoff value μ_{max}, which is taken to be larger than any physical possibility (normalisation therefore implies $P(\mu) = \mu_{\mathrm{max}}^{-1}$, which merely cancels from Eq. 4.14). Even if there is information available (such as bulk magnetisation or neutron diffraction data) which may influence the observers' predictions for the moment size μ, a uniform PDF is the most common choice for $P(\mu)$, since any corroboration between the information inferred from μSR $P(\mu \mid \nu)$ and other experimental techniques will serve as a more robust consistency check, and it is less likely that a physically reasonable discrepancy between the outcomes of these results (e.g., due to the very different time scales that they probe) will be overlooked.

Finally, since the frequency per unit moment size $f(\nu/\mu)$ PDF was calculated in Sec. 4.4.1, this must be related to $P(\nu \mid \mu)$ via

$$P(\nu \mid \mu) = \frac{1}{\mu} f(\nu/\mu), \tag{4.15}$$

where the factor of μ^{-1} arises to ensure that $\int P(\nu \mid \mu)\, d\nu = 1$ [generated PDFs are normalised such that $\int f(\nu/\mu)\, d(\nu/\mu) = 1$]. One may therefore obtain an expression for the ordered moment PDF *given* the experimentally observed precession frequency ν

$$g(\mu \mid \nu) = \frac{\frac{1}{\mu} f(\nu/\mu)}{\int_0^{\mu_{\mathrm{max}}} \frac{1}{\mu'} f(\nu/\mu')\, \mathrm{d}\mu'}, \tag{4.16}$$

where it is clear that this function is normalised to unity between the limits $\mu = 0, \mu_{\mathrm{max}}$.

Having calculated the frequency PDFs $f(\nu/\mu)$ shown in Fig. 4.9, Bayesian analysis may be therefore be employed in order to find the PDF for the ordered moment size using the observed precession frequency [$\nu = 23.4$ MHz at both 50 K and 300 K, shown in Fig. 4.6(a)]. Calculations were found to be insensitive to the value chosen of μ_{max} as long as it exceeds any conceivable value deduced by prior reasoning, which here was taken to be $10\mu_{\mathrm{B}}$.

The calculated ordered moment size PDFs $g(\mu \mid \nu)$ are displayed in Fig. 4.10, and
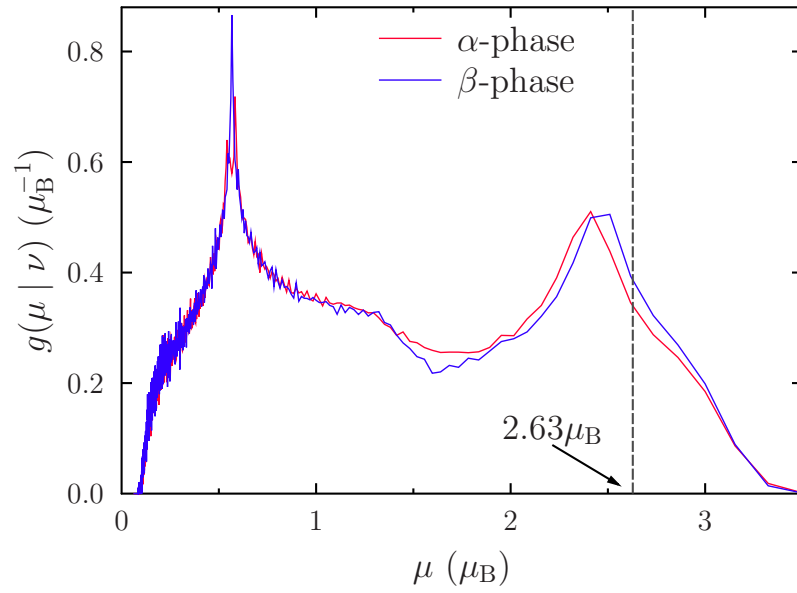
Figure 4.10: Ordered moment size PDF, obtained using the observed precession frequency $\nu = 23.4$ MHz.

there are peaks positioned very close to the indicated moment size of $2.63\mu_B$ within both the α and β phases. This agreement again demonstrates good consistency between muon data and magnetic structures determined by NPD. Secondary peaks at around $0.6\mu_B$ arise due to the PDF weight in $f(\nu)$ at around 110 MHz, and are emphasised due to the μ^{-1} factor in Eq. 4.14.

Returning to the question posed at the beginning of Sec. 4.4.1, the fact that all PDFs (Figs. 4.9 and 4.10) generated are remarkably similar for the monoclinic α and orthorhombic β phases suggests that the impact of the structural transition on the muon stopping site location (and hence local magnetic field strength) is not severe, and is therefore unlikely to be the sole cause of the suppression of the order parameter observed around $T^\star$. Instead, the apparent discrepancy between the Co^{3+} moment sizes as determined by NPD and μSR may be ascribed to the disparate time scales probed by the two experimental techniques. It is therefore concluded that the apparent suppression of the order parameter ν below $T \approx 200$ K [Fig. 4.6(a)] is most probably symptomatic of the complex freezing of spin dynamics on the muon time scale, discussed in Sec. 4.3.

4.5   Conclusion

In conclusion, μSR measurements allowed the critical behaviour near the remarkably high Néel temperature, determined to be $T_{\mathrm{N}} = 424(2)$ K, to be examined. The temperature dependence of the muon precession frequency (an effective order parameter for the antiferromagnetic LRO state) yields a value for the critical exponent $\beta = 0.35(2)$, which is consistent with the theoretical value predicted for a 3D Heisenberg antiferromagnet. In addition, our results have shed light upon the system's magnetic behaviour accompanying the structural phase transition around $T^{\star} \approx 100$ K. The bifurcation of bond angles, and hence superexchange pathway interaction strengths pertaining to the weaker AFM interdimer interactions, result in a complicated freezing of relaxation processes on the muon time scale. Dipole field simulations together with Bayesian analysis, within both the high- and low-temperature phases, has shown that the observed precession frequencies are consistent with the proposed magnetic spin structure (comprising FM ordered dimers, themselves arranged antiferromagnetically within the ac-plane, Fig. 4.3) deduced from NPD measurements. In the high-temperature β phase there is excellent quantitative agreement between the observed muon-spin precession frequency and the ordered cobalt moment size of $\mu = 2.63\mu_{\mathrm{B}}$ obtained via Rietveld refinement of NPD data. However, unlike the refined moment sizes obtained from NPD, the μSR order parameter is suppressed for temperatures below $T \approx 200$ K. This discrepancy further indicates the importance of the disparate time scales probed by the two techniques, and the role of dynamics on the muon time scale within $CsCoO_2$.

5

Magnetic Phase Diagram of La$_{2-x}$Sr$_x$CoO$_4$ Revised Using Muon-Spin Relaxation

This chapter shall present the results of a muon-spin relaxation (μSR) investigation of La$_{2-x}$Sr$_x$CoO$_4$, an antiferromagnetic insulating series which has been shown to support charge ordered and magnetic stripe phases and an hourglass magnetic excitation spectrum. A revised magnetic phase diagram is derived, which shows that the suppression of the magnetic ordering temperature is highly sensitive to small concentrations of holes. Distinct behaviour within an intermediate x range ($0.2 \leq x \lesssim 0.6$) suggests that the putative stripe ordered phase extends to lower x than previously thought. Further charge doping ($0.67 \leq x \leq 0.9$) prevents magnetic ordering for $T \gtrsim 1.5$ K. This chapter is based on work published in Ref. [161].

5.1 Introduction

5.1.1 Charge Ordering in Doped Mott Insulators

There has been intense theoretical and experimental interest in the physics of doped Mott insulators in the last few decades, driven in no small part by its relevance to the high-temperature superconductivity (HTSC) problem [162]. It shall be useful to briefly recap the basic theoretical principles that lead to the formation of the Mott insulator state, before introducing some of the main outcomes of doping charge carriers into this parent state and their relation to the complex phase diagrams of high-temperature superconductors.

The tight binding model shows how kinetic energy savings due to electron delocalisation may be achieved in a lattice via the process of 'hopping' from site so site (without changing spin state). This process favours metallic behaviour. However, this model neglects any on-site Coulomb repulsion between electrons, which are of great importance in correlated electron systems. The Hubbard model provides one way to parametrise an additional zero-ranged interaction, where the effective Hamiltonian may be expressed in the notation of second quantisation as

$$\hat{\mathcal{H}}_{\mathrm{HM}} = -t \sum_{\langle i,j \rangle, \sigma} \left(\hat{c}_{i\sigma}^{\dagger} \hat{c}_{j\sigma} + \hat{c}_{j\sigma}^{\dagger} \hat{c}_{i\sigma} \right) + U \sum_{i=1}^{N} \hat{n}_{i\uparrow} \hat{n}_{i\downarrow}, \tag{5.1}$$

for a system with N sites, and N electrons. Here, t is the transfer integral, the first sum is conducted over both spin states $\sigma = \uparrow, \downarrow$ and unique nearest-neighbour sites, $\hat{c}_{i\sigma}^{\dagger}$ ($\hat{c}_{i\sigma}$) is the creation (annihilation) operator, U determines the extent of on-site repulsion and $\hat{n}_{i\sigma} = \hat{c}_{i\sigma}^{\dagger} \hat{c}_{i\sigma}$ is the number operator on site i.

The relative magnitudes of the tight-binding bandwidth $W \propto t$ and the energy penalty U for double occupancy of a site (the first and second terms in Eq. 5.1, respectively) captures the competition between metallic and localised electron behaviour. For $U \gg t$ the on-site repulsion wins out, and there will be one electron per site and no hopping. The effective Hamiltonian for this strong-coupling limit is

given by the t–J model:

$$\hat{\mathcal{H}}_{t-J} = \hat{P}\left[-t\sum_{\langle i,j\rangle,\sigma}\left(\hat{c}_{i\sigma}^\dagger\hat{c}_{j\sigma} + \hat{c}_{j\sigma}^\dagger\hat{c}_{i\sigma}\right) + J\sum_{\langle i,j\rangle}\left(\hat{\boldsymbol{S}}_i\cdot\hat{\boldsymbol{S}}_j - \frac{\hat{n}_i\hat{n}_j}{4}\right)\right]\hat{P}, \qquad (5.2)$$

where $J = 4t^2/U$ is the exchange constant, $\hat{P} = \prod_i\left(1 - \hat{n}_{i\uparrow}\hat{n}_{i\downarrow}\right)$ is the projection operator that projects out all doubly occupied states and $\hat{n}_i = \sum_\sigma\hat{c}_{i\sigma}^\dagger\hat{c}_{i\sigma}$ is the spin-independent number operator on site i [2]. In this way, a material that should be a metal according to band theory may in fact be an electrical insulator. This state of affairs is called a *Mott insulator*. Within this scenario, an energy saving is achieved by virtual hopping events between nearest neighbours for antiferromagnetic (AFM) spin order, but is forbidden by the Pauli exclusion principle if neighbours are in the same spin state (ferromagnetism, FM). This explains the positive sign of J in the second term of Eq. 5.2.

Additional charges (electrons or holes) doped into a Mott insulating state have a strong inherent propensity to phase separate [163]. Kinetic energy reduction via delocalisation and long-ranged Coulomb repulsion between the doped charges compete with this tendency, and the result can be the self-organisation of charges into periodic regions of localised charge, called 'stripes' in 2D [164, 165]. These segregated regions may be considered to be unidirectional charge density waves, and break the rotational symmetry of the lattice in a manner analogous to the anisotropic nematic phase of a liquid-crystal. The charge ordered (CO) stripes may be 'site-centred' (as opposed to bond-centred), in which case they behave as an antiphase domain wall for the underlying AFM state, i.e., there is a phase shift of π between spin correlations on either side of the stripe.

Thirty years after the initial discovery of HTSC by Bednorz and Müller [166], the role of multiple order parameters in the cuprates continues to be a topic of intense research, with the nature of the interplay between correlations of CO, AFM spin order (SO) and superconductivity the topic of much investigation [167–170]. Many of the prototypical HTSC systems comprise 2D square CuO_2 planes, with AFM Mott insulating behaviour for the undoped compounds. Initially, the presence of CO in such systems was considered to be a material-specific effect and little more than a curious distraction which served to hinder the search for the underlying microscopic

HTSC pairing mechanism. However, more recent experimental advances have found CO to be quite ubiquitous among different cuprate systems. In particular, fluctuating charge density waves have been observed in various regions of the cuprate phase diagram, including the mysterious pseudogap phase [171–173]. Further evidence for the intertwined relationship between CO and the superconducting state was provided by the discovery that the anomalous suppression in the superconducting transition temperature T_c at the dopant concentration $x = 1/8$ in $La_{2-x}Ba_xCuO_4$ coincides with the most robust CO found in this system [174, 175]. In this instance it appears that the two order parameters are competing, since the application of magnetic fields below T_c enhances the CO whilst simultaneously suppressing the superconducting state [176].

Although a detailed comparison of specific systems has been found to be problematical, in order to elucidate the details of the physics at play in a different context, it is illuminating to study isostructural non-superconducting $3d$ transition metal oxides. For instance the systems $La_{2-x}Sr_xMO_4$ (M = Co, Ni, Mn) are isostructural to the '214' lanthanide cuprate (M = Cu) and all exhibit CO upon doping away from the Mott insulating AFM parent state [12].

5.1.2 $La_{2-x}Sr_xCoO_4$

This study is concerned with the M = Co AFM series $La_{2-x}Sr_xCoO_4$ (LSCO hereafter), the crystal structure of which is shown in Fig. 5.1. The perovskite structure comprises isolated 2D CoO_2 layers in the ab-plane, with La/Sr ions separating adjacent layers along the crystallographic c-axis and serving as charge reservoirs. The crystal symmetry of the ideal tetragonal unit cell is $I4/mmm$, however in certain regions of the phase diagram cooperative tilting of the CoO_6 octahedra lowers the crystal symmetry and results in an orthorhombic unit cell (discussed in more detail in Sec. 5.2.2).

Controlled doping of holes into the two dimensional CoO_2 layers is achieved via substitution of Sr^{2+} for La^{3+}. The lower valency of Sr relative to La results in the formation of Co^{3+} ions within the cobalt planes. One novel aspect of LSCO is the spin degree of freedom; whilst the octahedral crystal field environment leads to the
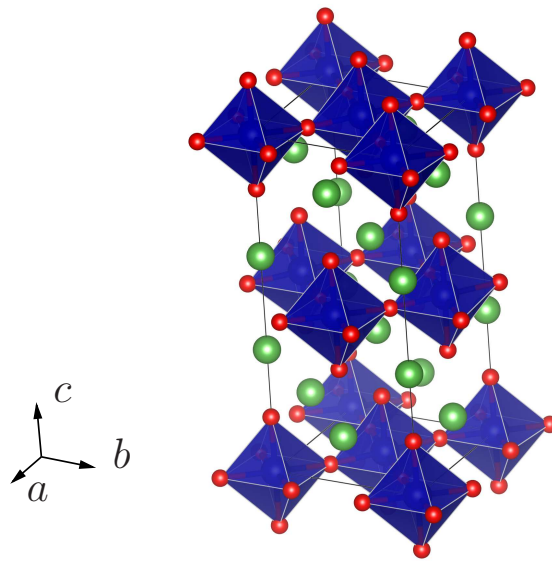
Figure 5.1: Illustration of the chemical structure of $La_{2-x}Sr_xCoO_4$ in the orthorhombic *Cmca* space group. Co (blue), O (red) and La/Sr (green) ions are shown. The octahedral coordination of the Co ions are shown, and these CoO_6 octahedra form an extended corner-sharing network in the *ab*-plane. Successive CoO_2 planes are staggered by $(0, 1/2, 1/2)$.

high-spin (HS) state ($S = 3/2$) for Co^{2+} ions [Fig. 5.2(b)], for the Co^{3+} ions the high-, intermediate- (IS) and low-spin (LS) states are energetically similar. For the doping x and temperature T ranges relevant to this study, it has been demonstrated that the Co^{3+} ions adopt the non-magnetic LS ($S = 0$) state shown in Fig. 5.2(c) [177–180]. Together with the crystal field, spin-orbit coupling constrains the Co^{2+} magnetic moments to lie within the *ab*-plane.

In contrast to the cuprates, the LSCO series remains an insulator for $x \leq 1$, with electrons well localised via a *spin-blockade* mechanism [179]. This mechanism may be understood by considering the electronic configurations of the HS Co^{2+} and LS Co^{3+} ions, shown in Figs. 5.2(b) and (c), respectively. It may be seen that a charge carrier hopping between neighbouring $Co^{2,3+}$ ions would result in new ion electron configurations that are not simply the original states swapped; instead such an event would result in a final state comprising an IS Co^{3+} ($S = 1$) and an energetically unfavourable LS Co^{2+} ($S = 1/2$). There is a significant energy cost accompanying such a hopping event, and they are therefore suppressed, resulting in large activation energies for the electrical conductivity.
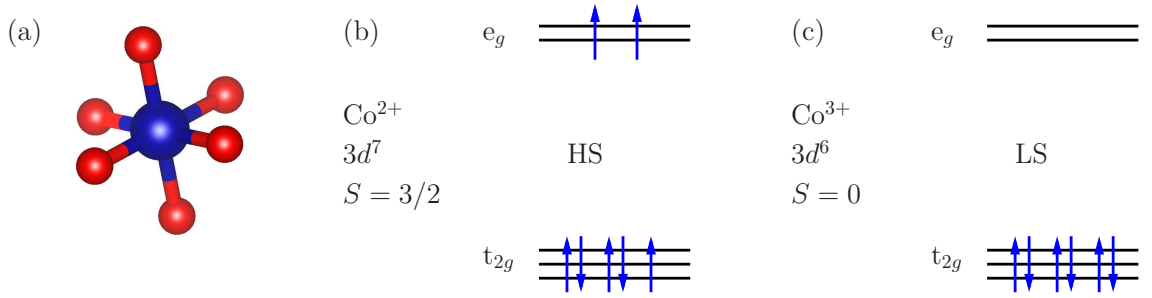
Figure 5.2: (a) The octahedral coordination of O (red) ligands around a Co (blue) ion. The resultant (b) high-spin (HS) electronic configuration for a Co^{2+} ion and (c) low-spin (LS) electronic configuration for a Co^{3+} ion.

The pristine parent compound La_2CoO_4 ($x = 0$) is a Mott insulator with nearest-neighbour antiferromagnetism (nnAFM) below the Néel temperature $T_N = 275$ K [181]. An inelastic neutron scattering (INS) study revealed the CoO_2 layers in La_2CoO_4 are well isolated (i.e., intraplane exchange couplings are strongly dominant) leading to quasi-two-dimensional behaviour with strong XY-like anisotropy [182]. The magnetic ground state for this state of affairs is illustrated in Fig. 5.3(a). The previously reported phase diagram of LSCO, determined by neutron scattering [183], shows this region of nnAFM persists for low dopant concentrations ($x \lesssim 0.3$), before an incommensurate (IC) magnetic phase consistent with stripe-like CO and SOs is encountered for an intermediate doping range $0.3 \lesssim x \lesssim 0.6$.

The excitation spectrum of the $x = 1/3$ compound was studied by Boothroyd *et al.* [184], who discovered that this compound exhibits the distinctive 'hourglass' magnetic excitation spectrum previously observed in the superconducting cuprates [185–189]. Subsequently, a similar (though broader) spectrum was observed in the $x = 0.25$ compound, which was shown to be consistent with the presence of (disordered) period-4 stripes [190], suggesting this IC regime extends to lower dopant concentrations that previously believed. The putative ordering in this regime (discussed in more detail in Sec. 5.2.4) is shown in Fig. 5.3(b), for the case of perfect stripe ordering for $x = 1/3$ case. Here, site-centred stripes composed of chains of non-magnetic Co^{3+} ions extend along the symmetrically equivalent [110] and [1$\bar{1}$0] directions and serve as antiphase domain walls. Ideal checkerboard ordering at half-doped case is shown in 5.3(c), which has been identified in the $x = 0.5$ compound [191, 192], with dominant
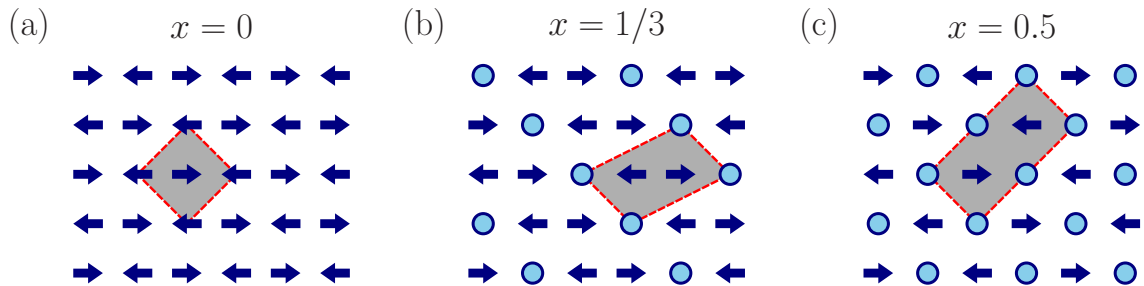
Figure 5.3: Perfect ordered spin structures within the 2D CoO_2 planes of $La_{2-x}Sr_xCoO_4$. Blue arrows depict HS Co^{2+} spin orientations, while open circles correspond to the non-magnetic LS Co^{3+} ions and magnetic unit cells are shown as the dashed red rectangles. (a) Nearest-neighbour antiferromagnetic order in $x = 0$. (b) Perfect period-3 stripe ordering in the $x = 1/3$ compound. (c) Checkerboard charge ordering hosting antiferromagnetic spin order in the $x = 0.5$ compound.

180° superexchange interactions between Co^{2+} spins mediated by the non-magnetic Co^{3+} ions [180].

As shown in Fig. 5.3, the magnetic unit cell is larger for the CO magnetic phases. Consequently, evidence for the stripe picture is provided by the incommensurate magnetic diffraction peaks observed at $\boldsymbol{Q}_m = \boldsymbol{Q}_{AFM} \pm (\zeta, \pm\zeta)$, where $\boldsymbol{Q}_{AFM} = (0.5, 0.5)$ is the peak position for the nnAFM order of the parent compound (using the reciprocal lattice vector notation for a square 2D lattice). Experimentally it has been found that the IC splitting ζ, which is determined by the stripe periodicity, scales closely with the level of charge doping as $\zeta = x + 2\delta$, where δ corresponds to the oxygen non-stoichiometry [12], i.e., more precisely the system LSCO is $La_{2-x}Sr_xCoO_{4+\delta}$. This relation between ζ and the density of doped holes has also been observed in the $M = Cu, Ni$ cases, and would not be expected for a charge/spin density wave scenario arising from nesting instabilities in the Fermi surface, and therefore lends weight to the stripe picture in these materials.

Recently, μSR and NMR measurements made on the stripe ordered $x = 1/3$ compound revealed the importance of a range of time scales in the magnetic ordering of the material [193], with μSR showing both the onset of static magnetic order and the freezing of dynamical processes at temperatures significantly lower than the ordering temperature previously identified using neutrons. This is because μSR is sensitive to fluctuations on the microsecond time scale (a scale set by the muon

gyromagnetic ratio $\gamma_\mu = 2\pi \times 135.5$ MHz T^{-1}). Such slow fluctuations appear static in neutron scattering measurements where the energy resolution $\Delta E \approx 1$ meV constrains the sensitivity of the technique to fluctuations with a much faster time scale $\hbar/\Delta E \approx 10^{-11}$ s.

The magnetic behaviour in this intermediate doping range in LSCO is evidently distinct to the nnAFM present in the undoped parent compound. However, there have currently been no comprehensive studies examining the evolution of the magnetism in this series as a function of x for small doping concentrations, so the location and character of the crossover between these magnetic regimes is not at all clear. Together with the μSR results for the $x = 1/3$ case, this has motivated the present study across a broad dopant range ($0 \leq x \leq 0.9$) to probe the influence of slow fluctuations on the low-temperature magnetism across this series and further elucidate a revised phase diagram.

5.2 μSR Measurements

5.2.1 Experimental Procedure

Crystals of LSCO were grown using the floating-zone method by D. Prabhakaran, University of Oxford, with varying sintering conditions depending on the Sr content x. Such crystals have a tendency for excess oxygen when $x \lesssim 0.3$, similar to the La$_{2-x}$Sr$_x$NiO$_{4+\delta}$ system [194–197]. On this basis it is expected that the lowest doped samples have $\delta > 0$, but approach oxygen stoichiometry by $x \approx 0.3$.

Zero-field μSR measurements were made using the EMU spectrometer at ISIS, and the GPS and DOLLY instruments at SμS. In all instances the initial muon polarisation was directed along the c-axis of each crystallite, perpendicular to the planes containing the CoO$_2$ layers. (A small fraction of the data collected for this study was measured prior to the start of this PhD project. In particular, the $x = 0.33$ data has been previously published in Ref. [193] and the $x = 0.5$ data has appeared in the PhD thesis in Ref. [198]. All data analysis presented in this chapter, including the re-analysis of historic data, was performed by the author.)
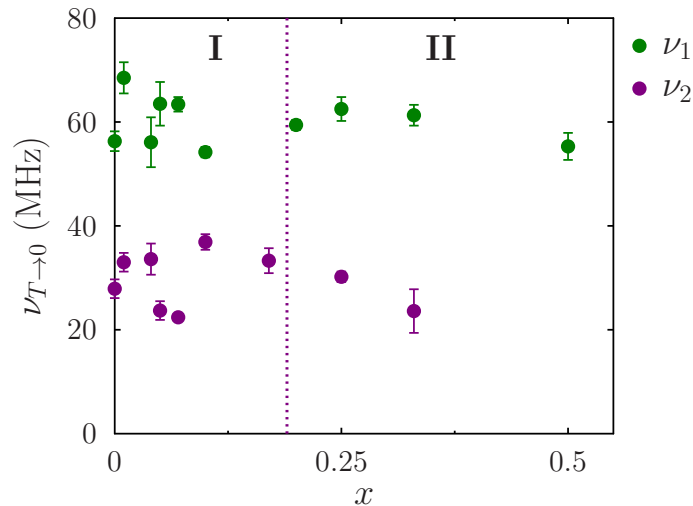
Figure 5.4: Fitted low-temperature ($T < 10$ K) muon precession frequencies in LSCO across the doping range $x \leq 0.5$. The dashed line shows the approximate boundary between the regions I and II (as defined in the text), however no changes in the magnitudes of ν_i are resolvable.

5.2.2 Overview

In data measured at SμS spontaneous damped oscillations are visible at low temperature in the asymmetry spectra for all concentrations with $x \leq 0.5$. These are indicative of quasistatic local magnetic fields at the muon sites and confirm the presence of SO in each compound. The lowest temperature spectrum measured was fitted for each sample (employing a cosinusoidal oscillatory relaxation function), and the resulting low temperature precession frequencies $\nu_{T \to 0}$ are shown in Fig. 5.4. The two precession frequencies observed in most samples indicate two distinct classes of muon site with local field strengths in the approximate ratio 2:1 (although for certain concentrations only one frequency is resolvable). There is very little doping dependence in the magnitude of the two precession frequencies, supporting the claim that Co^{3+} ions remain in the non-magnetic LS ($S = 0$) state throughout this doping range [177, 178, 180], and that there is little variation in the moment size of the magnetic $S = 3/2$ Co^{2+} ions.

Before considering detailed analysis of individual dopant concentrations, a broad survey of the concentration-temperature (x–T) phase diagram shall be presented, which forms the main result of this study. To do this, it is illustrative to consider
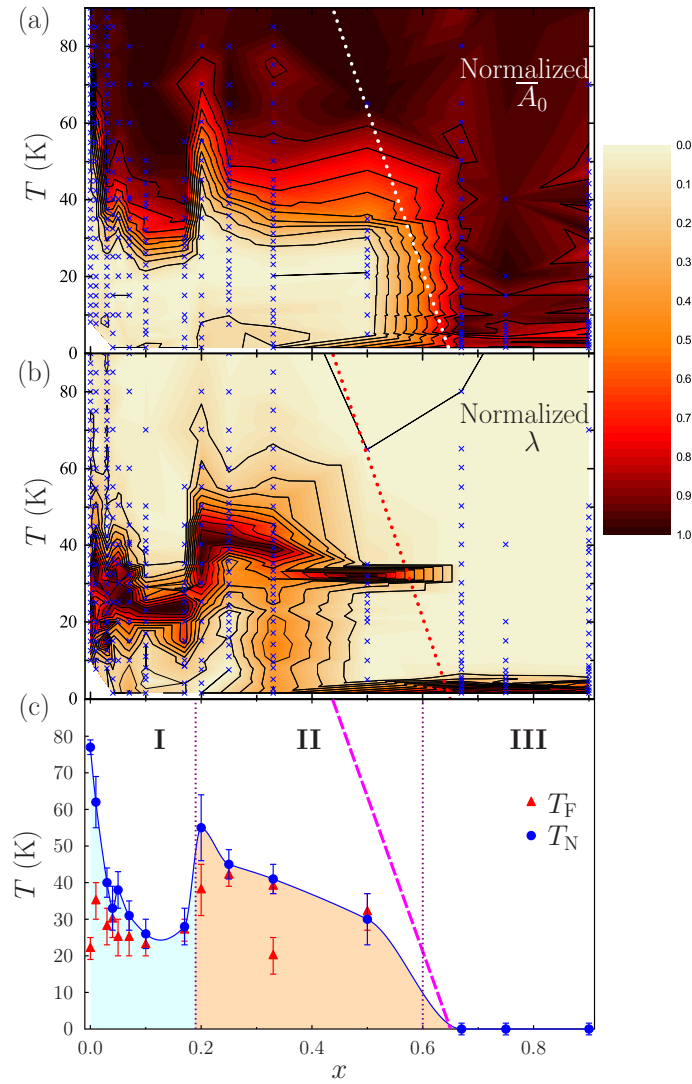
Figure 5.5: (a) Normalised early-time initial asymmetry $\overline{A}_0$ in the x–T plane. (b) Normalised relaxation rate λ. Blue crosses identify measured points and the dashed line shows the phase boundary from Ref. [183]. (c) Revised phase diagram showing the nominal transition temperature T_N and freezing temperature T_F. The dotted lines highlight the boundaries between three regions (I – III) of distinct behaviour.

the average early-time asymmetry $\overline{A}_0 \equiv \langle A(t \leq 0.13 \ \mu\text{s}) \rangle$, where the time averaging allows one to identify the depolarisation of the muon spin ensemble due to static or slowly fluctuating magnetism, shown in Fig. 5.5(a), where each data point is normalised between extreme values for that particular sample. For concentrations $x \geq 0.67$ no drop in initial asymmetry is observed in the data upon cooling. In order to eliminate changes in $\overline{A}_0$ due to fast relaxation resolvable in SμS spectra for these

samples ($x = 0.67$, 0.75, 0.9), the early-time averaging procedure was modified to use the time window $t \leq 0.015$ μs, and normalised between 0 and the maximum value of $\overline{A}_0$. At high temperatures, well above T_N, the muon spins are insensitive to rapidly fluctuating Co^{2+} moments (motional narrowing), leading to large values of $\overline{A}_0$. For concentrations $x \leq 0.5$ initial asymmetry is lost upon cooling, reflecting the presence of large internal magnetic fields, such as those giving rise to the oscillations described above. This drop in $\overline{A}_0$ may be fitted with a Fermi-like broadened step function

$$\overline{A}_0(T) = A_H + \frac{A_L - A_H}{e^{(T-T_c)/w} + 1},\tag{5.3}$$

which provides a transition temperature T_c by parametrising the continuous step of width w from high- to low-T asymmetry, A_H and A_L, respectively [104]. For this analysis the early-time averaging criterion of $t \leq 0.015$ μs was utilised for all data measured at SμS, to take fuller advantage of the increased time resolution relative to ISIS data. An onset temperature for magnetic ordering may be obtained using $T_N = (T_c + w) \pm w$, and these values are shown in the revised phase diagram Fig. 5.5(c).

The previous μSR study on $x = 0.33$ also demonstrated the technique's sensitivity to slow fluctuations and the freezing of dynamics [193]. To follow these features across the phase diagram of LSCO datasets were heavily binned to filter out high frequency components and fitted to the stretched exponential relaxation function

$$A(t) = A_{rel}e^{-(\lambda t)^\beta} + A_b,\tag{5.4}$$

where A_{rel} and A_b are the relaxing and non-relaxing baseline amplitudes, respectively and β was constrained to be greater than 0.5. This phenomenological expression is a versatile relaxation function, able to characterise a broad range of decaying curve shapes and extract a representative relaxation rate λ. This fitting routine was found to capture the same qualitative features at the same temperatures as more complex fitting routines involving sums of exponential and Gaussian terms, which have a more physically tractable basis. The versatility of the stretched exponential term allows direct comparisons to be made for the data measured across the entire x–T plane of the phase diagram. The data were binned into time intervals of $\Delta t = 16.0$ ns for ISIS data (the highest resolution available) and 3.91 ns for SμS data, for which

the greatest available resolution is $\Delta t = 0.977$ ns ($\Delta t = 9.77$ ns was used for the SμS data for $x = 0.9$ to account for the lower statistic datasets). This serves to average out the oscillations visible in $A(t)$ for low times in SμS data for samples below T_N, and hence reduce their impact on the coarser fit.

The resulting fitted relaxation rates λ (also normalised) are shown in Fig. 5.5(b). This analysis is sensitive to longitudinal dephasing of the muons' polarisation, where in the fast fluctuation limit it is expected that the relaxation rate $\lambda \propto \langle (B - \langle B \rangle)^2 \rangle \tau$ (i.e., the second moment of the magnetic field distribution multiplied by the correlation time τ [36]) reflecting both field distribution widths and fluctuation rates (see Sec. 2.4.4). A peak in λ is often indicative of a freezing of dynamics on the muon time scale as correlation times diverge, and so nominal freezing temperatures T_F defined as the temperature corresponding to peak values of λ are also presented in the phase diagram Fig. 5.5(c).

Three distinct regions in the phase diagram may be distinguished. For $x < 0.2$ (Region I, hereafter) the introduction of non-magnetic $S = 0$ Co^{3+} ions suppresses the ordering temperature of the commensurate nnAFM order, and there is evidence of a freezing of dynamics at lower temperatures for compounds with small x. For intermediate doping concentrations ($0.2 \leq x \lesssim 0.6$, Region II) the behaviour is consistent with that previously observed for $x = 0.33$, suggesting that CO within the CoO$_2$ layers may stabilise IC stripe-like SO with a cluster glass nature. For $x \gtrsim 0.6$ (Region III) the system remains in the paramagnetic state down to low temperatures. The data in each region is examined in more detail below.

In general, it should be noted that for all temperatures of interest in this study ($T \leq 100$ K) the crystal structure of LSCO has been shown to assume orthorhombic (*Cmca* or *Bmab*, depending on choice of axes) symmetry for $x \leq 0.33$ and tetragonal (*I4/mmm* symmetry) for $x \geq 0.4$ [183, 199–201]. This structural transition does not coincide with either boundary of region II, and so does not appear to be a driving factor for the magnetic behaviour in this system.
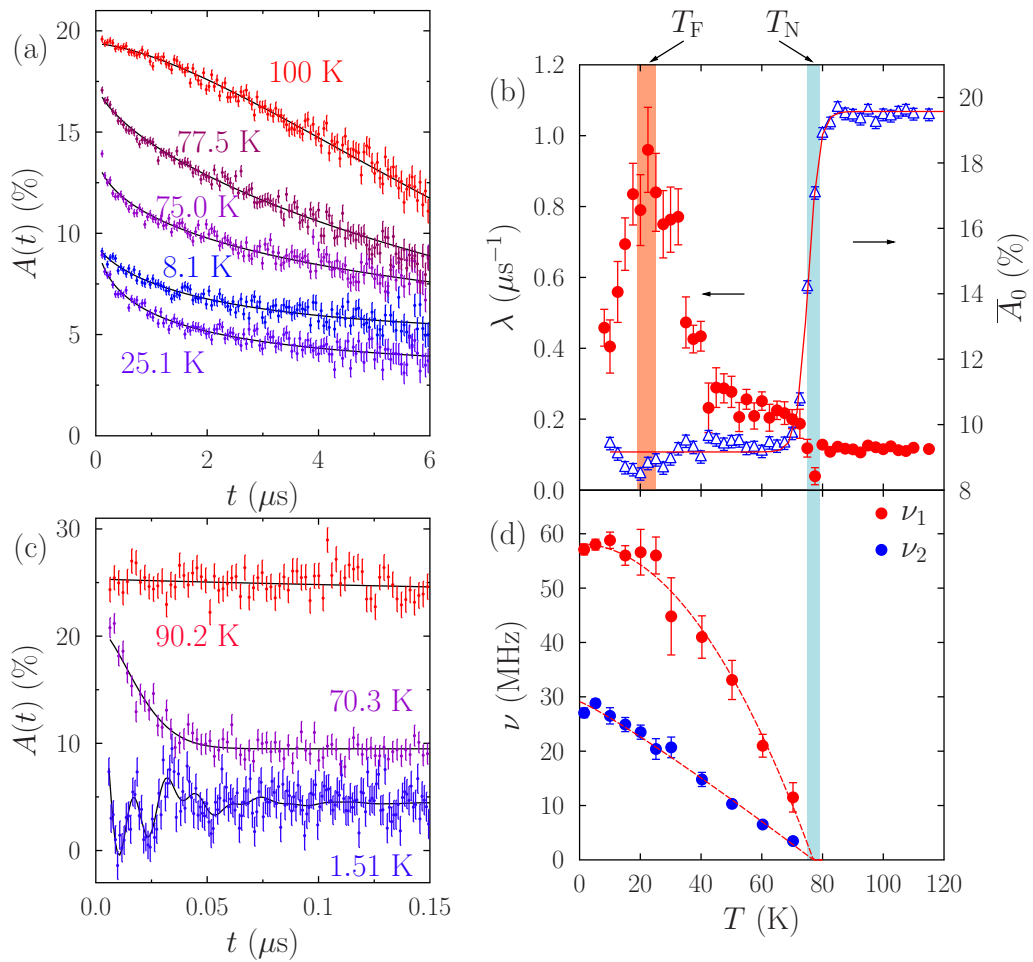
Figure 5.6: (a) Asymmetry data for $x = 0$ measured at ISIS. Solid lines are fits to Eq. 5.4. (b) Relaxation rate λ used to determine T_{F}, plus early-time asymmetry $\overline{A}_0$ used to locate T_{N} [non-normalised data from Fig. 5.5(b) and (a), respectively]. Red line is the fit to the broadened step function Eq. 5.3. Blue and salmon shaded regions show the ordering and freezing temperatures, T_{N} and T_{F}, respectively. (c) Data measured at SμS, showing spontaneous precession at low temperature (1.51 K data shifted by -5% for clarity). Solid lines are fits to the two-frequency relaxation function Eq. 5.5. (d) Temperature evolution of the two precession frequencies. Dashed lines are guides for the eye.

5.2.3   Region I

Data measured on the $x = 0$ compound La_2CoO_4 at SμS show spontaneous oscillations in the muon polarisation for temperatures below $T \approx 75$ K [Fig. 5.6(c)], confirming a transition to SO. The asymmetry spectra within the ordered regime were found to be best fitted for $t \leq 0.5$ μs to the two-frequency relaxation function

$$A(t) = \sum_{i=1,2} A_i \cos(2\pi\nu_i t)e^{-\lambda_i t} + A_{\rm rel}e^{-\lambda_{\rm rel}t}, \tag{5.5}$$

where the high and low frequency oscillatory components, with amplitudes $A_{1,2}$ fixed to their average values of 6% and 10%, respectively, indicate two magnetically inequivalent muon stopping sites. The fitted values of the precession frequencies $\nu_{1,2}$ are plotted in Fig. 5.6(d), and drop to zero at a temperature $T_{\rm N}$, as expected for a magnetic transition to a paramagnetic state.

Measurements made at ISIS are well suited to probing the slow dynamics of the system, typical spectra for $x = 0$ are shown in Fig. 5.6(a). An abrupt drop in average early-time asymmetry is apparent upon cooling below $T \approx 75$ K [Fig. 5.6(b)] and a fit to the broadened step function Eq. 5.3 yielded an ordering temperature value of $T_{\rm N} = 77(2)$ K, consistent with the vanishing of the oscillations in the SμS data. Upon further cooling below $T \approx 70$ K $\overline{A}_0$ does not change, but the longitudinal relaxation rate increases to a peak at around 22.5 K, before dropping again at lower temperatures. This is suggestive of a freezing of dynamics (as the correlation time τ increases) at much lower temperatures than the transition to magnetic long range SO. This feature is shared by the $x = 0.01$ sample, which could indicate that the introduction of frustration by small concentrations of non-magnetic, $S = 0$ Co^{3+} ions induces a freezing transition for a relaxation channel that has a characteristic time scale within the μSR dynamical range. The freezing is visible in the asymmetry spectra below $T_{\rm F}$ [see Fig. 5.6(a)] as an increase in the non-relaxing baseline amplitude, reflecting those components of muon-spin polarisation parallel to the local magnetic field which can only be relaxed by dynamic field fluctuations.

The value of $T_{\rm N} = 77(2)$ K determined using μSR for $x = 0$ is considerably suppressed compared to the accepted value of 275 K reported in Ref. [181]. We attribute this to oxygen non-stoichiometry, which is an alternative route to doping

holes into the CoO$_2$ layers (for La$_{2-x}$Sr$_x$CoO$_{4+\delta}$ the hole density is given by $n_h = x + 2\delta$), as seen in the cuprate and nickelate systems [202, 203]. Further annealing of an $x = 0$ sample led to a restored value of T_N of approximately 275 K, however, the lowered amplitude of the μSR signal and subsequent NMR measurements indicate that the annealing process introduces impurity phases, particularly at the surfaces of the crystals. As Sr is introduced within Region I ($x < 0.2$), T_N is found to drop abruptly to around 30 K by $x \approx 0.1$. This effect, together with that of the oxygen non-stoichiometry, demonstrates the sensitivity of the magnetism within the LSCO system to the concentration of non-magnetic Co^{3+} ions within the CoO$_2$ layers. The presence of holes due to excess oxygen dramatically suppresses the onset temperature compared to the pristine compound, and T_N is further reduced rapidly by further addition of holes via Sr doping. This is in contrast to both the previously reported phase diagram proposed on the basis of neutron scattering [183], and the predictions of percolation theory for static non-magnetic impurities in two dimensions where long range AFM SO would persist up to $x \approx 0.41$ [204, 205]. However, the effect is much less abrupt than in the superconducting series La$_{2-x}$Sr$_x$CuO$_4$ where long range SO is replaced by an IC spin-glass phase by just $x = 0.02$ [206] (in the revised phase diagram Fig. 5.5(c) $\frac{dT_N}{dx} \approx -10^3$ K/doped hole at low x; an order of magnitude smaller than in the cuprate series). The freezing temperature T_F does not decrease in the same manner, but remains at around 25 K across Region I. The convergence of T_N and T_F above around $x = 0.1$ suggests that for these concentrations the peak in relaxation rate is sensitive to the critical divergence in correlation times accompanying the transition to magnetic SO on the muon time scale.

5.2.4 Region II

As more holes are introduced into the CoO$_2$ layers via further Sr substitution, a marked change in behaviour for concentrations $x \geq 0.2$ is encountered, with samples in the region $0.2 \leq x \leq 0.5$ showing similar responses, suggestive that they share common features which might relate to stripe ordering. Stripe order in LSCO has been proposed for $x \geq 0.3$ on the basis of neutron scattering experiments [183]. Doping away from the parent compound introduces disorder and frustration into the

planes and intermediate doping levels have been suggested to lead to short-range stripe correlations which stabilise IC magnetic order. The most robust CO within the LSCO system is checkerboard CO which occurs at half doping ($x = 0.5$) [191, 192], where in-plane CO correlation lengths are largest [183]. Despite having different electronic properties to the cuprates, LSCO samples with $x = 0.33$ and 0.25 which exhibit disordered stripe CO correlations display the distinctive hourglass magnetic excitation spectrum, as discussed in Sec. 5.1.2. Simulations using a cluster spin glass model (CSGM) where frustrated magnetic ions decorate a background of short-range stripe CO correlations with quenched disorder [207] have reproduced the qualitative features of the hourglass excitation spectrum [190], strengthening the argument that stripes and hourglass excitation spectra are intimately linked. However, the origin of the hourglass spectrum and the nature of the CO in this region remains controversial. Specifically, due to the insulating nature of the material and the disparate energy scales of CO and SO it has been suggested that the origin of the IC magnetic order is not stripe-like physics [208]. Furthermore, nanoscale phase separation of regions of the undoped compound and the stable checkerboard CO exhibited by $x = 0.5$ doping has been proposed as the source of the hourglass excitation spectrum observed by INS [200, 201].

The results of μSR and NMR measurements of the $x = 1/3$ compound revealed the onset of magnetic order within partially disordered charge and spin stripes at around 35 K, with a further glassy freezing of dynamics involving the slow, collective motion of spins within the magnetic stripes at lower temperatures [193]. The new results presented here show that the μSR response of $x = 0.25$ is similar to that of the $x = 0.33$ material, although the slightly broader features preclude the identification of a second freezing feature at lower temperatures. This is consistent with the conclusions drawn in the previous neutron study that the behaviour in the $x = 0.25$ compound is qualitatively similar to that in $x = 0.33$, however the period-4 stripes exhibit a greater degree of disorder and shorter correlation lengths [190].

A key observation is that behaviour of $x = 0.2$ is markedly different to that of samples in Region I, and suggests stripe correlations exist to lower concentrations x than previously believed. Typical asymmetry spectra obtained at SμS are shown
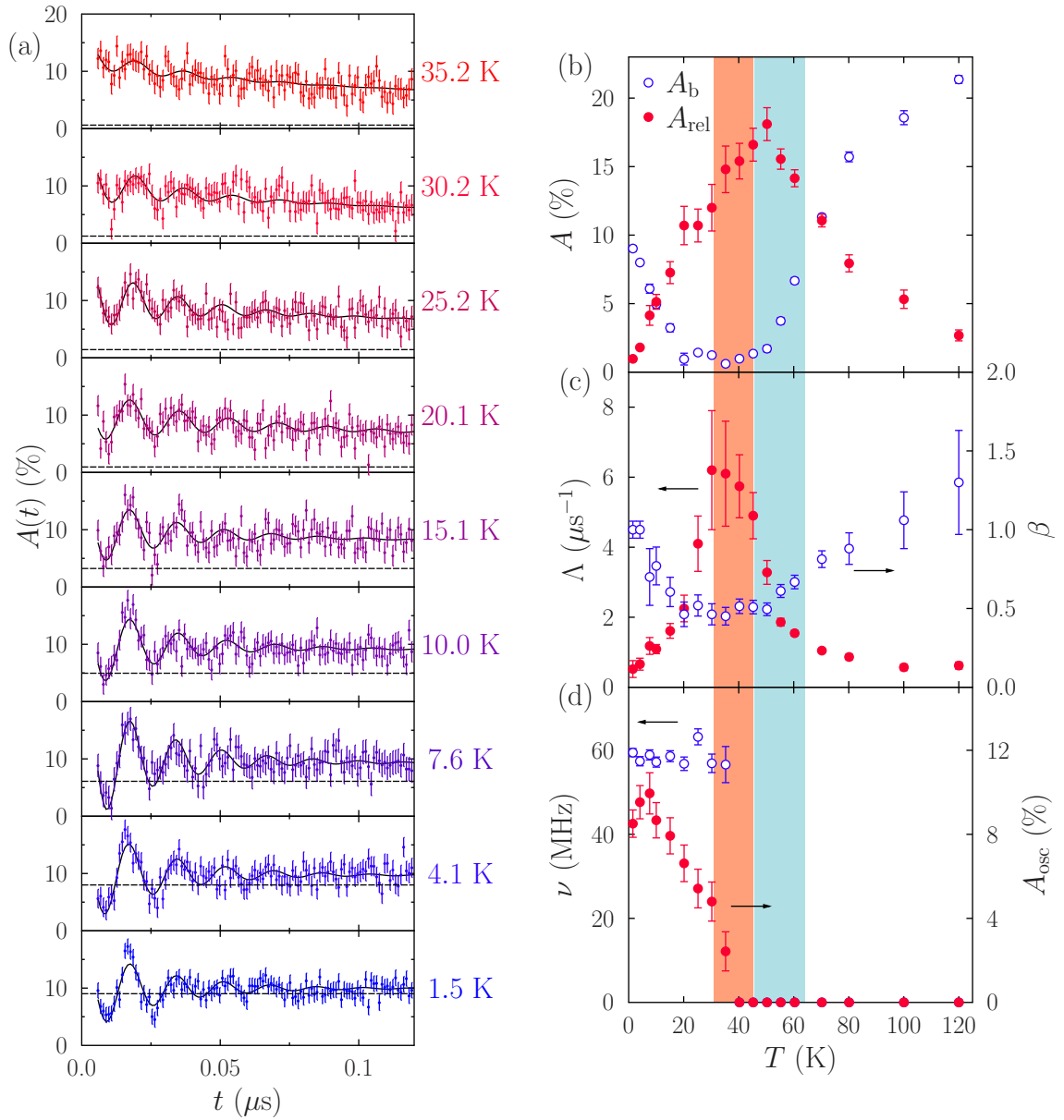
Figure 5.7: (a) Asymmetry data measured at SμS for $x = 0.2$ showing the evolution of oscillations, and the non-relaxing baseline (dashed horizontal lines), with temperature. Solid lines are fits to Eq. 5.6. (b) Amplitudes of relaxing and baseline components. (c) Longitudinal relaxation rate Λ and stretching exponent β. (d) Amplitude and frequency of the oscillatory component.

in Fig. 5.7(a), and exhibit oscillations due to coherent muon-spin precession for temperatures below around 40 K. Asymmetry spectra were best fitted to the single-frequency relaxation function

$$A(t) = A_{\text{osc}} \cos(2\pi\nu t + \phi)\mathrm{e}^{-\lambda_{\text{osc}}t} + A_{\text{rel}}\mathrm{e}^{-(\Lambda t)^\beta} + A_{\text{b}}, \qquad (5.6)$$

for the time window $t \leq 4.6$ μs, where the transverse relaxation rate λ_{osc} was fixed to its average value of 39 μs^{-1} and the oscillatory amplitude A_{osc} was fixed to zero once oscillations disappear for $T \geq 40$ K. Broad peaks in the temperature dependence of both longitudinal relaxation rate Λ and amplitude A_{rel} [Fig. 5.7(b), (c)] suggest a freezing temperature $T_{\text{F}} = 38(7)$ K, consistent with that obtained using the non-oscillatory relaxation function Eq. 5.4, discussed in Sec. 5.2.2. In this temperature region the stretched exponential exponent β takes its minimum value of about 0.5, reflecting the very rapid depolarisation of the muon ensemble. Interestingly, the precession frequency ν appears to be approximately independent of temperature for $T \leq T_{\text{F}}$ [Fig. 5.7(a), (d)], whereas the oscillating amplitude A_{osc} drops drops to zero upon warming towards T_{F} [Fig. 5.7(d)], reflecting a drop in the magnetic volume fraction within the sample. Upon cooling below 20 K, there is a gradual increase in the non-relaxing contribution A_{b} [Fig. 5.7(a), (b)] which points to a more static field distribution. Taken together, these results are consistent with slow dynamics within spatially inhomogeneous disordered stripes of magnetic Co^{2+} ions which start to freeze out upon cooling below around 40 K, with regions of static, glassy SO gradually appearing as temperatures are lowered further. This description is consistent with a cluster glass, previously observed only at higher x [190].

The $x = 0.5$ compound has been of special interest as it has been found to support checkerboard CO below around $T_{\text{CO}} \approx 800$ K [180, 191, 192]. Susceptibility and neutron scattering measurements reveal magnetic correlations appearing for $T \lesssim 60$ K [180, 209] and a spin freezing transition at around 30 K dominated by 180° antiferromagnetic interactions between Co^{2+} ions across the non-magnetic Co^{3+} sites [180]. Our muon data show a broad drop in $\overline{A}_0$ on cooling through around 30 K, coinciding with a peak in relaxation rate and the appearance of heavily damped oscillations indicating the onset of SO. No features are observed around 60 K, where moments are still fluctuating outside of the muon time scale. We

note that the high level of disorder for $x = 0.5$, indicated by the heavily damped nature of the oscillations, is surprising given the high charge ordering temperature for this compound [183, 191, 192]. However, the observation of a single oscillatory period within asymmetry data provides an approximate lower bound on the magnetic correlation length of around $10a \approx 4$ nm (where a is the nearest-neighbour spin separation) [26], which is consistent with previously reported in-plane correlation lengths deduced using neutron scattering experiments [180, 183, 191].

5.2.5 Region III

For Sr concentrations $x \gtrsim 0.5$, neutron measurements have revealed short range IC magnetic correlations on the neutron time scale [210]. Here, it was proposed that glassy SO is established within (and between) superstructures of phase separated, short range CO (i.e., regions of checkerboard, and period-3, -4... stripes). Our measurements in Region III detect no long range SO on the muon time scale down to the lowest measured temperatures ($T \approx 1.5$ K) for the compounds $x = 0.67$, 0.75 and 0.9. For these samples, no muon-spin precession is resolvable and full initial polarisation is maintained at all temperatures. Example spectra from this region are shown in Fig. 5.8(a)–(c), which also show that there is no static recovery at low temperatures; depolarisation increases monotonically upon cooling and no freezing temperature is discernible. Spectra were best fitted to a relaxation function comprising two exponentially decaying components plus a non-relaxing background contribution:

$$A(t) = A_{\mathrm{f}}\mathrm{e}^{-\lambda_{\mathrm{f}}t} + A_{\mathrm{s}}\mathrm{e}^{-\lambda_{\mathrm{s}}t} + A_{\mathrm{b}}, \tag{5.7}$$

where the initial asymmetry was fixed to the high-temperature value of $\overline{A}_0$ for each compound, and the ratio between fast (λ_{f}) and slow (λ_{s}) relaxation rates was approximately 10^2 (the fit quality was improved with λ_{s} fixed to its average value of 0.13 MHz for $x = 0.90$). The fit parameters show qualitatively similar behaviour for the three compounds: both the fast component amplitude A_{f} and relaxation rate λ_{f} increase as temperature is decreased from around 15 K in a very similar manner to the gradual increase in IC magnetic superstructure Bragg peak intensity observed using neutron scattering for samples with $x \geq 0.6$ [183, 211]. This behaviour can
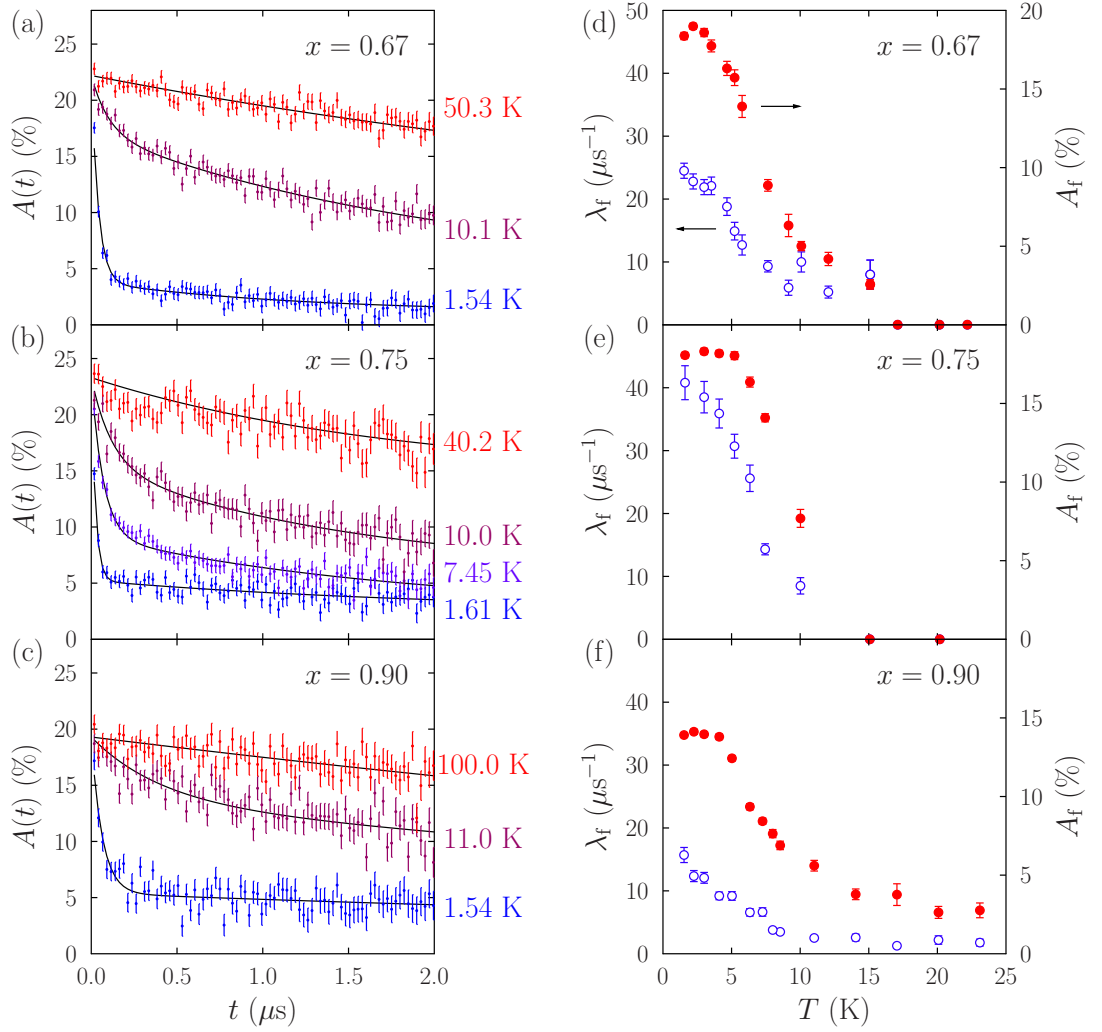
Figure 5.8: (a)–(c) Example asymmetry spectra from compounds in Region III ($x = 0.67$, 0.75 and 0.9), measured at SμS. Solid lines are fits to Eq. 5.7. (d)–(f) Fitted amplitudes and relaxation rates of the fast relaxing components.

be attributed to the moments fluctuating more slowly as temperature is lowered. The magnitude of λ_f as T approaches zero is greatest for $x = 0.75$, indicating longer magnetic correlation times for this concentration. The asymmetry in the fast relaxing component behaves similarly for the three compounds and does not scale with the concentration of non-magnetic Co^{3+} ions, suggesting that there is no straightforward phase separation within these samples. If SO occurs above 1.5 K, then it could be either short-ranged or still fluctuating too rapidly on the muon time scale to be detectable.

5.3 Discussion

It is natural to ask how the updated magnetic phase diagram for LSCO compares to those of related layered transition metal oxide systems. A comparison with the superconducting cuprate cousins of LSCO (described in Sec. 5.1.1) is of particular interest, since the relationship between CO, AFM SO and superconductivity in these systems is the subject of such intense theoretical and experimental research.

The unique high/low-spin nature of the magnetic and charge ordered cobalt ions in LSCO, and its ensuing insulating nature, means comparisons to other isostructural systems should be treated with caution. However, the revised phase diagram for LSCO derived by this study does share some features with those of the cuprates and nickelates. The rapid suppression of T_N with increasing x in lightly doped samples is reminiscent of $La_{2-x}Sr_xCuO_4$ and other cuprates, where local probe measurements also reveal a continuous spin-freezing transition at temperatures well below that of magnetic ordering [212–215]. It is important to recognise that the fundamental physics underlying the behaviour of cuprate systems is of a very different nature to that in LSCO. In prototypical layered cuprate materials Cu^{2+} ions have an electronic configuration $3d^9$, where a Jahn Teller distortion of the octahedral oxygen environment breaks the e_g orbital degeneracy and leads to a half occupied $d_{x^2-y^2}$ orbital (or, equivalently, one hole per Cu site, with $d_{x^2-y^2}$ character). This $d_{x^2-y^2}$ orbital has nodes oriented towards the four neighbouring O^{2-} $2p_{x,y}$ orbitals in the ab-plane, resulting in significant d–p hybridisation. The undoped parent compounds are in fact *charge transfer insulators* [216, 217] where, as for LSCO, the small spatial extent of Cu $3d$ orbitals leads to large correlations and on-site repulsion. However, in cuprate compounds the oxygen $2p$ orbitals lie at higher energies than the half-filled Cu $3d$ orbitals, and so low-energy excitations involve the motion of holes onto neighbouring oxygen p_x or p_y orbitals, rather than Cu ions in neighbouring unit cells. The large on-site repulsion in this picture still results in an electrically insulating parent state, in close analogy to the Mott insulator phase introduced in Sec. 5.1.

In cuprate systems the addition of doped holes rapidly suppresses the onset

temperature T_N of the nnAFM phase. This is because the doped holes occupy oxygen p orbitals, which subsequently mediate strong FM interactions between neighbouring Cu ions, frustrating and suppressing the parent nnAFM order [218]. In fact, it may be shown that a kinetic energy reduction is achieved if the doped hole delocalises as a coherent, symmetric superposition of hole states on four oxygen p orbitals neighbouring (and oriented towards) a central Cu ion. This superposition hole then hybridises with the original $d_{x^2-y^2}$ hole residing on the Cu ion, forming a so called 'Zhang–Rice' singlet [219]. The low-energy behaviour of this singlet state is well described by an effective single-band t–J model Hamiltonian, Eq. 5.2. In this picture the singlet is able to hop between neighbouring sites, with a large energy penalty for double occupancy, which explains the success of earlier treatments employing single-band theories, such as that by Anderson [220]. Furthermore, at higher dopant concentrations, charges may segregate and self-organise, where the proposed stripes lie parallel to Cu–O bond directions (stripes are oriented at 45° to Co–O bonds in LSCO).

A range of investigations have been conducted regarding the location of the muon stopping site in the cuprate system $La_{2-x}Sr_xCuO_4$, by considering magnetic dipole field arising from magnetic and nuclear moments, electrostatic potential landscapes and *ab initio* calculations. The broad consensus is that the muon is believed to come to rest near the apical oxygen of the CuO_6 octahedra [221–225]. It may be expected that the muon behaves similarly in the LSCO series. It is possible to show [226] that the depolarization of an implanted muon is sensitive to field correlations Φ_{ii} where i are directions in the plane perpendicular to the initial direction of the muon polarization $\boldsymbol{P}(t=0)$. In our experiments $\boldsymbol{P}(t=0)$ is parallel to the crystallographic c-axis of the tetragonal unit cell, and therefore i are directions in the ab-plane. Magnetic moments in ordered state are also confined within the ab-plane, however, since muons couple to dipole fields, the field and spin directions do not generally coincide. It is possible that density functional theory calculations (as discussed in Chap. 3) may be able to better identify the muon stopping site in LSCO, however this technique is still under development.

In addition to the comparison with cuprates, the μSR results of this study

indicate that the behaviour associated with region II extends over a broad range of x, implying that the updated phase diagram bears a greater similarity to that of $La_{2-x}Sr_xNiO_{4+\delta}$ (LSNO) [12, 227–230]. The appearance of stripe CO in LSNO is well established [227, 231], where site centred stripes of Ni^{3+} ions are oriented at 45° to Ni–O bonds, in close analogy to LSCO. However, the stripe phase in the nickelate system is of a very different character, since the charge stripes themselves remain magnetically active [232] and exchange interactions persist between and within regions of $S = 1$ Ni^{3+} and $S = 1/2$ Ni^{2+} ions. Previous μSR studies also revealed that the magnetic behaviour in LSNO is dependent on the absolute values of both x and δ, rather than merely the total hole dopant concentration $n_h = x + 2\delta$ [230, 233].

So, in answer to original question raised at the beginning of this section, direct comparisons to other layered perovskite systems must be treated with prudence. However, certain features of the updated magnetic phase diagram presented in this chapter for LSCO do suggest a greater degree of similarity to those of cuprates and nickelates.

5.4   Conclusion and Further Work

In summary, this μSR study has elucidated the doping dependence of the magnetic behaviour across the phase diagram of the non-cuprate hole-doped layered antiferromagnet $La_{2-x}Sr_xCoO_4$ on the muon (μs) time scale, enabling the identification of three distinct regions of behaviour:

- For $x \lesssim 0.2$ the ordering temperature T_N for the commensurate nnAFM SO is heavily suppressed by the introduction of holes into the CoO_2 layers. An additional freezing of slow dynamics is also observed at temperatures well below T_N for very small dopant concentrations.

- For $0.2 \lesssim x \lesssim 0.6$ ordering temperatures are larger and IC magnetic ordering is likely to be stabilised by stripe correlations in the CO, suggesting this putative stripe region extends to lower hole concentrations than previously believed.

- Finally, above $x \approx 0.6$ spin fluctuations slow upon cooling below around 15 K,

but the system remains paramagnetic down to temperatures of 1.5 K.

The major unresolved issue in the LSCO series is the nature of the SO and CO in the intermediate doping region, thought to host the putative stripe phase. On the basis of this study, it appears a better understanding of the behaviour of the $x = 0.2$ compound would help illuminate this discussion. An INS study of the magnetic excitation spectrum for this compound would be one way to further elucidate the physics at play within region II, and at the crossover to the nnAFM behaviour of region I.

6

Transverse-Field Muon-Spin Rotation Study of the Skyrmion Lattice Phase in Cu$_2$OSeO$_3$

This chapter shall present the results of the first transverse-field (TF) muon-spin rotation (μSR) measurements to be made on a skyrmion lattice (SL) phase. The response of the TF μSR signal is measured in the SL phase of Cu$_2$OSeO$_3$, together with that of the neighbouring ones, and it is suggested how the phases might be distinguished using the results of these measurements. AC susceptibility measurements confirm the presence of the SL phase in the polycrystalline powder samples used. Complementary dipole field simulations support the conclusion that the muon is sensitive to the SL via the TF lineshape and, based on this interpretation, these measurements suggest that the SL is quasistatic on a time scale $\tau > 100$ ns. This

chapter is based on work published in Ref. [234].

6.1 Introduction

6.1.1 Topology and Skyrmions

The understanding of matter and its excitations in terms of topology has a long history which is now allowing insight into the properties of quantum materials and the opportunity for their manipulation. Topological physics includes the study of kinks, vortices and monopoles in quantum field theory, which forms the basis of a successful branch of condensed matter physics [235, 236].

Within a general field theory, topological objects arise in broken symmetry states, reflecting the defects which occur when symmetry has been broken in different ways in different spatial regions [4]. Topological objects cost a finite amount of energy and are finite in spatial extent. They arise from translationally and Lorentz invariant field theories, meaning they may be localised anywhere and boosted to arbitrary velocity, and are therefore particle-like. Topologically protected objects possess an integer topological number which is conserved, in analogy with electrical charge, and may not be altered by continuous deformations of the field configuration. In this way a topological object is robust against perturbations and fluctuations. This topological charge is impervious to the metric (i.e., it is independent of exact spacetime geometries), which is why these objects are termed *topological*. The stability of these objects is due to the fact that they are time-independent and non-dissipative; they are held together by their own self-interaction.

This concept was employed by Tony Skyrme in order to explain the stability of a set of particle-like states in a non-linear field theory [237, 238]. The resultant localised, particle-like topological objects were termed *skyrmions*. Applications of this seminal theory permeate much of physics, from the original topic of hadrons within nuclear physics, to neutron stars within astrophysics and classical liquids [239]. Remarkably, the theory has proved extremely useful within the field of condensed matter physics, playing an important role in liquid crystals [240], Bose-Einstein condensates [241] and quantum Hall systems [242, 243]. Arguably, however, the most

successful realisation of skyrmions has been the stable spin structures which have been shown to exist in a range of magnetic materials at particularly well-defined conditions of temperature and magnetic field.

Within the context of magnetism, the simplest example of a topological object is that of a domain wall within a ferromagnet. Here, the domain wall is the boundary (of finite width) between different domains where the symmetry has been broken in two distinct ways (i.e., spins aligned in two different directions), and is an example of a *kink*. For an infinitely large sample, the removal of the kink would require 'flipping' a (semi)infinite number of spins, at an infinite energy cost.

A two-dimensional system with a magnetic order parameter of dimensionality $D = 2$ corresponds to the two-dimensional XY model, where spins are confined to a plane. In this system the Coleman-Wagner-Mermin theorem precludes symmetry breaking long range magnetic ordering for $T \neq 0$. However, the two-dimensional XY model may host topological objects known as *vortices*, which are localised swirling spin textures. It may be shown that a single vortex is unstable at zero temperature; its energy cost diverges as the size of the system tends to infinity. This energy cost arises since the spins are still swirling infinitely far from the vortex core, which competes with the rigidity of the system. This instability may be overcome by two distinct means. Firstly, bound vortex-antivortex pairs (with opposite topological charges) permit uniform (non-swirling) spin textures at infinity, and therefore cost finite energy. Secondly, unbound vortices may be spontaneously thermally produced at high temperatures, since the entropic benefit resulting from the freedom to localise the vortex core at any site within the sample diverges with the system size. This entropic reduction of the free energy $F = U - TS$ may outweigh the energy cost of an individual vortex, and free vortices are permitted. Both of these disordered states have been observed in real magnetic systems, and the topological phase transition between them is the Berezinskii-Kosterlitz-Thouless transition which occurs at a temperature K_{BKT} [244, 245].

If the order parameter dimensionality is increased to $D = 3$ (as for an isotropic Heisenberg spin) in a two-dimensional system, then singularities in the spin texture near the vortex centre are able to be avoided as spins may tilt out of the xy-plane and

acquire a z component. This configuration is called a *meron*, and a meron-antimeron pair with opposite spins generates a skyrmion spin texture. In three dimensions it may be shown that topological objects may assume the form of magnetic monopoles.

Magnetic skyrmions were theoretically predicted as stable ground states in the presence of chiral interactions (breaking inversion symmetry) [246], and were subsequently detected in reciprocal space using neutron diffraction [247], before Lorentz transmission electron microscopy (LTEM) [248] and spin-resolved scanning tunnelling microscopy [249] led to their observation in real space.

In general, an expression for the magnetic free energy may be minimised to give rise to numerous ground state magnetic textures, expressed as $\boldsymbol{m}(\boldsymbol{r}) = m\boldsymbol{n}(\boldsymbol{r})$, where $\boldsymbol{m}(\boldsymbol{r})$ is the magnetic moment of an individual spin centre with magnitude m and orientation $\boldsymbol{n}$ at the position $\boldsymbol{r} = (x, y)$. Two skyrmionic spin structures, namely Bloch- and Néel-type, are shown in Fig. 6.1, where the cross-sections taken through the vortex cores in each instance highlight the analogy with ferromagnetic domain walls which gave them their names. Both of these spin structures are characterised by non-zero integer topological skyrmion numbers, defined as [236]

$$N_{\mathrm{sk}} = \frac{1}{4\pi} \iint \mathrm{d}^2\boldsymbol{r}\, \boldsymbol{n} \cdot \left(\frac{\partial \boldsymbol{n}}{\partial x} \times \frac{\partial \boldsymbol{n}}{\partial y} \right), \tag{6.1}$$

where the integral is taken over the 2D magnetic unit cell, and $N_{\mathrm{sk}} = \pm 1$ for skymions and antiskyrmions, respectively, but is identically zero for topologically trivial ferromagnetic or helical states. In the Bloch-type (or 'whirlpool') skyrmion, as one moves from the core to the outer periphery of the vortex, spins rotate in the plane perpendicular to the radial unit vector, whereas in the Néel-type skyrmion (or Belavin Polyakov monopole [250]) the spins rotate in the radial planes.

The simplest example of a Néel-type skyrmion spin texture [6.1(b)] may be derived from a sphere studded with arrows pointing radially (a monopolar field configuration, reminiscent of a hedgehog). A skyrmion is formed if one stereographically projects the arrows onto a plane while keeping their orientations fixed [252]. A Bloch-type skyrmion [6.1(a)] is instead generated if one first 'combs' the sphere before performing the projection into the plane. Both of these procedures results in a twisting pattern which is topologically protected in analogy with a stable knot; it may be translated
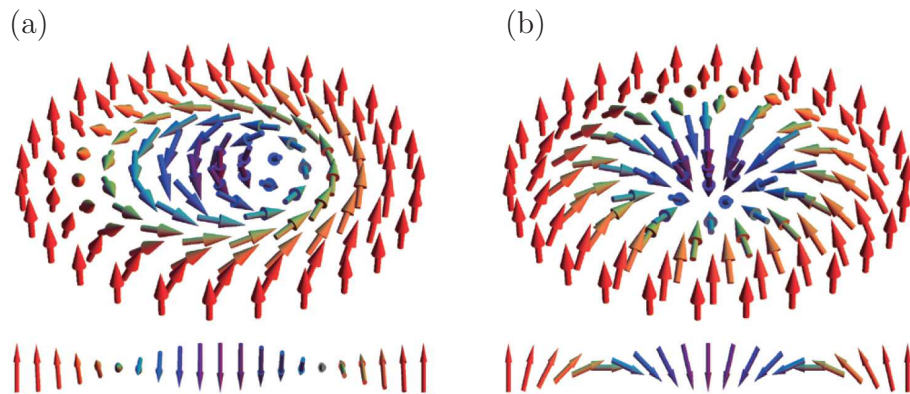
Figure 6.1: (a) Bloch- and (b) Néel-type skyrmion spin structures. Arrows represent the spin direction $\boldsymbol{n}$ at each spin centre. Cross-sections through the vortex core are shown for each case. Figure taken from Ref. [251].

and boosted like a localised particle, but is robust to any small perturbations and cannot be untied as long as the fields remain smooth and energetically finite.

It is clear that the Bloch-type skyrmion spin texture depicted in 6.1(a) has a specific chirality or handedness; the twisting or swirling pattern has a specific directionality. It is therefore unsurprising that systems which host skyrmions must be non-centrosymmetric, i.e., they lack inversion symmetry. Prototypical skyrmion materials share the same B20 structure (space group $P2_13$) with cubic chiral symmetry, and spectacular experimental successes have demonstrated not only the existence of magnetic skyrmions in these systems, but also their ordering into a periodic arrangement called a *skyrmion lattice* (SL). Small angle neutron scattering first revealed the presence of the SL phase in bulk samples of MnSi [247] and $Fe_{1-x}Co_xSi$ [253], within a small region of the B–T plane. The fact that the SL phases are found at temperatures near transitions to the paramagnetic state highlights the role played by thermal fluctuations in stabilising the complex spin structures. After these initial neutron studies, LTEM measurements of thin film [248, 254] and nanowire [255] samples allowed real-space imaging to be performed and revealed the SL regions of the phase diagrams have much greater extent in systems spatially confined to fewer dimensions. LTEM has also demonstrated the existence of a SL in FeGe [256] where, once again, the phase is greatly extended as the sample is thinned [257]. Inversion symmetry may also be broken in local regions by the presence of domain

walls or sample interfaces, and similar spin structures have been previously observed at domain boundaries and in specially constructed nanomagnetic systems [258–260].

The second class of skyrmion is the Néel-type shown in Fig. 6.1(b). This variety of skyrmions was theoretically predicted to exist in non-chiral crystal structures with C_{nv} symmetry. In fact, their existence has only been demonstrated recently, where they have been observed in the polar magnetic semiconductor GaV_4S_8 [251]. In contrast to Bloch-type skyrmions where the orientation of the plane containing the vortex is dictated by the direction of an external magnetic field (discussed in detail below), the Néel skyrmion is confined to the magnetic easy-axis arising due to the crystal structure. The broad extent of the novel skyrmion phase in the temperature-field plane makes this system a prime candidate for future study, however the rest of this discussion shall be concerned with Bloch-type skyrmions.

Materials hosting skyrmions provide a promising avenue of research for technological advancements in spintronic devices. In metallic (or semiconducting) skyrmionic materials spin-polarised conduction electrons experience a spin-transfer torque as they traverse a skyrmion spin texture and their spins are twisted to align with the local magnetisation direction $\boldsymbol{n}(\boldsymbol{r})$ [261, 262] (a consequence of Hund's coupling as the electron hops from ion to ion). This effect may be pictured in an alternative way; skyrmions generate fictitious magnetic fields which impart a quantum mechanical Berry Phase [263] upon electrons as they move through the system and, in analogy to the Lorentz force, also serve to deflect their trajectories. This transverse force is the underlying cause of the topological Hall effect observed in skyrmion phases [264, 265]. The converse effect of this interaction is that (spin-polarised) electric currents in turn exert a force upon the particle like skyrmions, and may therefore be used to manipulate the spin textures themselves. In fact, skyrmions may be moved in this way with extremely low current densities, several orders of magnitude lower than those required to move conventional ferromagnetic magnetic domain walls [266]. In addition, skyrmions' credentials as prospective candidates for use in logic devices and high density data storage have been enhanced by recent studies demonstrating the creation and annihilation of individual skyrmions (or writing and deleting in data storage nomenclature) using local spin polarised currents [267], inhomogeneous

currents [268] and even mechanical stress [269].

6.1.2 Skyrmions in Cu_2OSeO_3

A SL phase has been shown to exist in the insulating helimagnetic compound Cu_2OSeO_3 [270–273], which also crystallises in the cubic chiral B20 structure. The region of the Cu_2OSeO_3 phase diagram which hosts the SL (also known as the 'A-phase') is shown in Fig. 6.2(a), where the phase boundaries have been taken from Ref [270]. In this system, reported phase diagrams have varied slightly between different studies (e.g., Refs. [270, 272, 274]). These differences may reflect sample variation, where ferrimagnetic (FiM) spin arrangements (plus net magnetisation from spin canting at finite B_0) lead to the presence of demagnetising fields, which are dependent on sample geometry and very difficult to correct for. These demagnetising fields also depend on the strength and orientation of the externally applied field B_0 and may lead to the relocation and broadening of phase boundaries, which may help explain the coexistence of helical and SL phases (these effects have previously been observed in both Cu_2OSeO_3 [272] and MnSi [275, 276]).

In this material, spins are located on the Cu^{2+} ions, which are arranged in four tetrahedra within the unit cell, as illustrated in Fig. 6.2(b). The 16 Cu ions within the unit cell are divided into two crystallographically inequivalent classes denoted Cu1 and Cu2, with multiplicity 1 and 3, respectively. FiM ordering of these spins is favoured, with Cu1 ions oriented in the opposite direction to that of the Cu2 ions (in high magnetic fields Cu1 and Cu2 spins align antiparallel and parallel to the applied field, respectively) [277–279]. This FiM configuration persists within the more complicated spin configurations described below [280].

In systems such as Cu_2OSeO_3 which lack inversion symmetry, chiral interactions are capable of stabilising helically ordered configurations of spins [246]. The helical ordering is a collective effect, which may be understood in terms of an energy hierarchy comprising three interactions. The energetically dominant interaction is the isotropic ferromagnetic exchange interaction, which contributes a Heisenberg
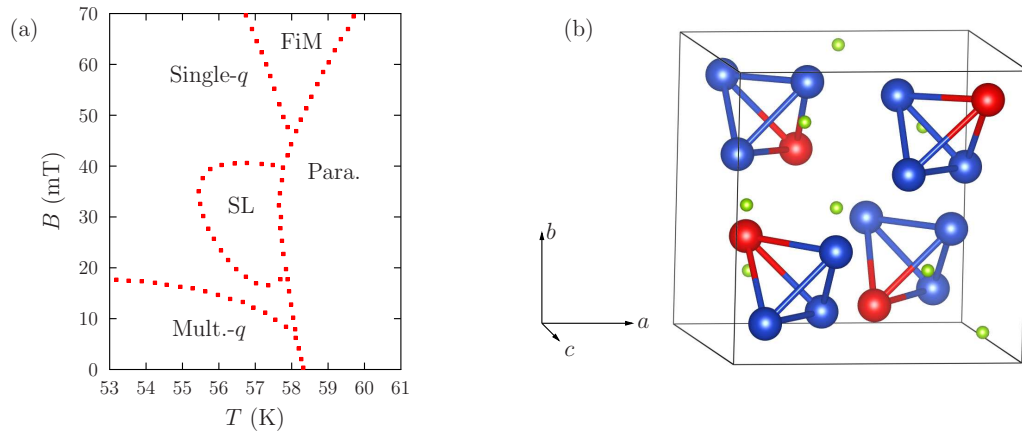
Figure 6.2: (a) The phase diagram of bulk Cu_2OSeO_3, indicating the locations of the paramagnetic, ferrimagnetic (FiM), single-q and multi-q helical, and skyrmion lattice (SL) phases described in the text. These phase boundaries are taken from Ref [270]. (b) Crystal unit cell of Cu_2OSeO_3. Bonds are shown to highlight the tetrahedral arrangement of Cu ions, and the Cu1 (red) and Cu2 (blue) classes of ions have been differentiated. Oxygen ions have been omitted and selenium ions (green) have been reduced in scale for clarity.

term to the Hamiltonian of the form

$$\hat{\mathcal{H}}_{\mathrm{H}} = -\sum_{\langle i,j \rangle} J_{ij} \ \hat{\boldsymbol{S}}_i \cdot \hat{\boldsymbol{S}}_j, \tag{6.2}$$

where the sum is performed over unique pairs of nearest-neighbour spins $\hat{\boldsymbol{S}}_{i,j}$. This term favours a collinear arrangement of spins (with magnetic moments lying parallel to one another in the ferromagnetic instance). The next largest contribution arises from the Dzyaloshinsky-Moriya interaction (DMI) or anisotropic exchange interaction [281–283]. Here, the relativistic spin-orbit interaction may promote one magnetic ion into an excited state, which subsequently interacts with the ground state of a neighbouring ion via $\hat{\mathcal{H}}_{\mathrm{H}}$. This leads to a DMI term in the Hamiltonian, with the form

$$\hat{\mathcal{H}}_{\mathrm{DM}} = \sum_{\langle i,j \rangle} \boldsymbol{D}_{ij} \cdot \hat{\boldsymbol{S}}_i \times \hat{\boldsymbol{S}}_j, \tag{6.3}$$

where the value and orientation of the vector $\boldsymbol{D}$ are determined by crystal symmetry [6, 7]. The vector $\boldsymbol{D}$ is identically zero when the crystal field has an inversion symmetry with respect to the centre midway between the two ions with spins $\hat{\boldsymbol{S}}_i$ and $\hat{\boldsymbol{S}}_j$. However, when this inversion symmetry is not present $\boldsymbol{D}$ may lie either parallel or in the plane perpendicular to the vector connecting the two spin centres,

depending on the exact symmetry relations at the centre between them. The cross product between neighbouring spin vectors in the DMI interaction favours non-collinear helical spin arrangements, with fixed chirality determined by the direction of $\boldsymbol{D}$. Taken together these dominant exchange interactions stabilise long wavelength helimagnetic spin textures in Cu_2OSeO_3. Finally, weak magnetic anisotropy leads to a preferential orientation of the propagation q vectors for this helical order. It is worth noting that other stabilising mechanisms have been identified for skyrmion spin textures, including long range dipolar interactions [284], geometric frustration [285] and dynamical effects [286].

In Cu_2OSeO_3 the result (in the presence of a small or zero external magnetic field) is the phase described as the multi-q helimagnetic (or simply the helimagnetic phase). In bulk single-crystal samples, this consists of multiple domains of helimagnetic stripes whose q vectors are aligned along the three $\langle 001 \rangle$ directions [271, 272]. The application of an external magnetic field (with magnitude above a lower critical field value) creates a single q vector, which is aligned parallel to the direction of the field, forming a single-q helimagnetic phase (also called the conical phase) where there are no multiple domains [270–272]. Above a second, larger critical field there is a transition to a FiM phase, where the (Cu1) Cu2 ion spins are aligned (anti)parallel to the applied field.

Above $T_c \approx 60$ K the system is a disordered paramagnet, however just below this transition temperature an applied external magnetic field (with magnitude between the lower and upper critical fields) can stabilise a SL phase. Approximate SL spin textures are formed from a phase-locked superposition of helimagnetic textures with a triangular arrangement of wave vectors $\boldsymbol{q}$ (with orientations differing by 120°) lying in the plane perpendicular to the field [287] (the resultant configuration is translationally invariant in the direction of the field). This is the so-called '3–$\boldsymbol{q}$' spin texture, which captures the topology of the SL phase. Originally this structure was proposed on the basis of a mean-field Landau-Ginzburg treatment, where it appears as a metastable state stabilised by thermal fluctuations [247]. More sophisticated treatments of the SL are possible, for example helical and SL spin structures may be shown to arise via minimisation of a magnetic free energy expression for magnetisation within a

cubic chiral magnet under various external magnetic field strengths (including the absence of an external field altogether) [246, 288, 289].

This A-phase or skyrmion lattice phase (often denoted SkX) is centred around $B_0 = 30$ mT and $T = 57$ K, nestled close to the critical temperature T_c [270–272]. It has further been shown in a bulk single crystal system that this phase may be further subdivided into two subphases, with the SL in the second being rotated by thirty degrees with respect to the lattice in the first [271]. The magnitude of applied magnetic fields over which the SL phase occurs in Cu_2OSeO_3 allows a characteristic muon time scale to be extracted via $\tau = (2\pi)/(\gamma_\mu B_0) \approx 0.25$ μs, which lies well within the ISIS and the SμS muon source time windows.

6.1.3   Another Topological Phase: the Vortex Lattice

There is considerable similarity between the SL and another topological phase in condensed matter physics: the vortex lattice (VL) found in type II superconductors in applied magnetic field. Like the SL, the superconducting VL leads to a textured, periodic distribution of magnetic field within the body of the material, which is large on the scale of the crystallographic unit cell. In practice, the same experimental techniques that have been successfully applied to probing VL physics, such as small angle neutron scattering [290] and, in particular, μSR could potentially be applied to probe the physics of the SL and this hypothesis is what motivates the μSR study presented in this chapter. This investigation was intended to determine the extent to which transverse-field (TF) μSR measurements are sensitive to the skyrmion phase in the multiferroic skyrmion material Cu_2OSeO_3.

In this study the use of TF μSR to probe the SL in Cu_2OSeO_3 is analogous to its use in probing the VL in a type II superconductor, where the technique provides a powerful means of measuring the internal magnetic field distribution caused by the presence of the magnetic field texture [37, 40]. Here, spin polarised muons are implanted in the bulk of a material, in the presence of an external magnetic field B_0, which is applied perpendicular to the initial muon spin direction. Muons stop at random positions on the length scale of the field texture where they precess about the total local magnetic field B at the muon site (mainly due to the field texture).

The observed property of the experiment is the time evolution of the muon spin polarisation $D_x(t)$, which allows the determination of the distribution $p(B)$ of local magnetic fields across the sample volume via $D_x(t) = \int_0^\infty dB\, p(B) \cos(\gamma_\mu B t + \phi)$, where the phase ϕ results from the detector geometry (see Sec. 2.4.3).

6.2   Sample Preparation and Characterisation

For this study polycrystalline powder and single crystal samples of Cu_2OSeO_3 were synthesised by G. Balakrishnan, University of Warwick, as described previously [277], where the same batch of polycrystalline powder was also used for the growth of the single crystals using the chemical vapour transport technique. The samples were characterised with powder and single crystal x-ray diffraction which confirmed that the samples were of the requisite B20 phase.

The magnetisation and AC magnetic susceptibility of both single crystal and polycrystalline powder samples were measured with a Quantum Design MPMS-XL SQUID magnetometer. Figure 6.3(a) and (b) show the temperature dependence of the real (χ') and imaginary (χ'') components of AC susceptibility, respectively, for a static external magnetic field of $B_0 = 25$ mT (plus an oscillatory component with magnitude 0.2 mT and frequency 700 Hz). The real component χ' data for the single crystal sample are in excellent agreement with the data presented in Ref. [271], and reveal a transition temperature $T_c \approx 57.5$ K and an approximate lower bound for the SL phase of $T \approx 55.5$ K (for this particular external field). These values are suppressed by around 0.5 K in comparison to those previously reported, however this small discrepancy is most probably due to the dependence of phase boundaries on the orientation of the magnetic field with respect to the crystal axes (it was not possible to identify the orientation of the single crystal used for the measurements presented here). The response of the powder sample displays a transition at T_c consistent with the single crystal sample [also revealed by the DC susceptibility shown in the inset to Fig. 6.3(a)], however assumes a slightly different shape below this temperature, where detail is most likely lost due to averaging over all crystal orientations. The single crystal sample exhibits a distinct peak in χ'' at temperatures just below T_c,
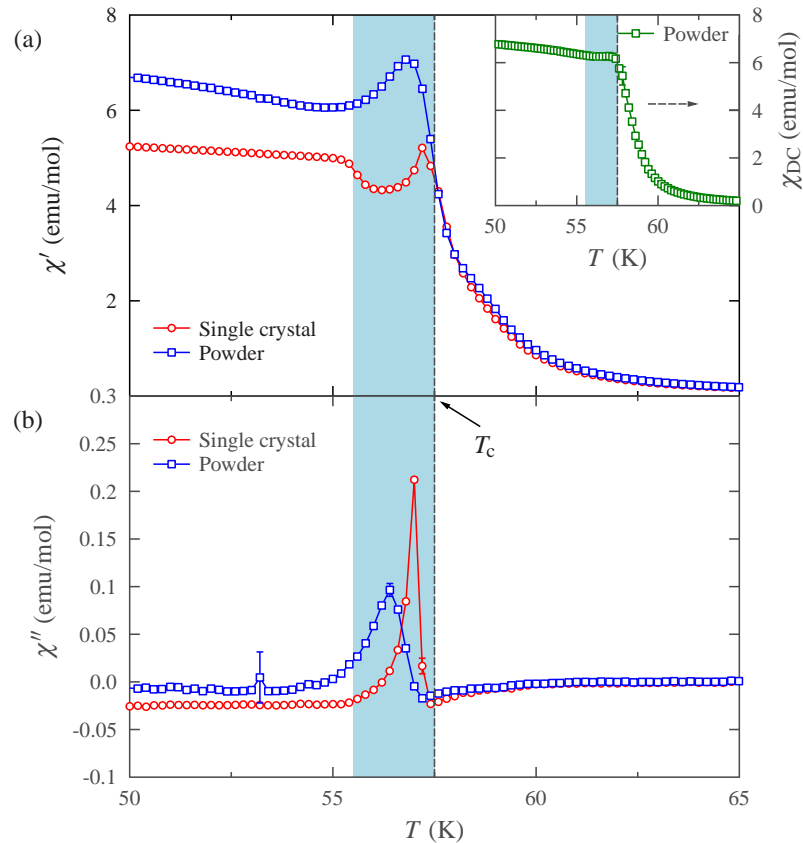
Figure 6.3: Temperature dependence of the (a) real χ' and (b) imaginary χ'' components of the molar AC susceptibility for single crystal and polycrystalline powder samples of Cu_2OSeO_3. Data were measured in a static magnetic field $B_0 = 25$ mT with an additional oscillatory field component of amplitude 0.2 mT and frequency 700 Hz. Inset to (a): DC magnetic susceptibility of the powder sample (also in a 25 mT field). The approximate SL phase region is highlighted (bound by 55.5 K $\leq T \leq T_c$ where $T_c \approx 57.5$ K).

where the peak rises sharply upon cooling through T_c before decaying more gradually as temperature is further decreased [Fig. 6.3(b)]. A similar feature is present in the powder sample, however it is broadened relative to the single crystal case, as one might expect considering the full range of crystal orientations present within a powder sample.

The magnetic field dependence of the AC susceptibility was also investigated, and data (for selected temperatures in the vicinity of the SL phase) are presented in Fig. 6.4 for both single crystal and powder samples. The real component of the AC susceptibility χ' behaves in a qualitatively similar manner for both the single crystal and powder samples, in good agreement with that previously reported [270, 271, 291].
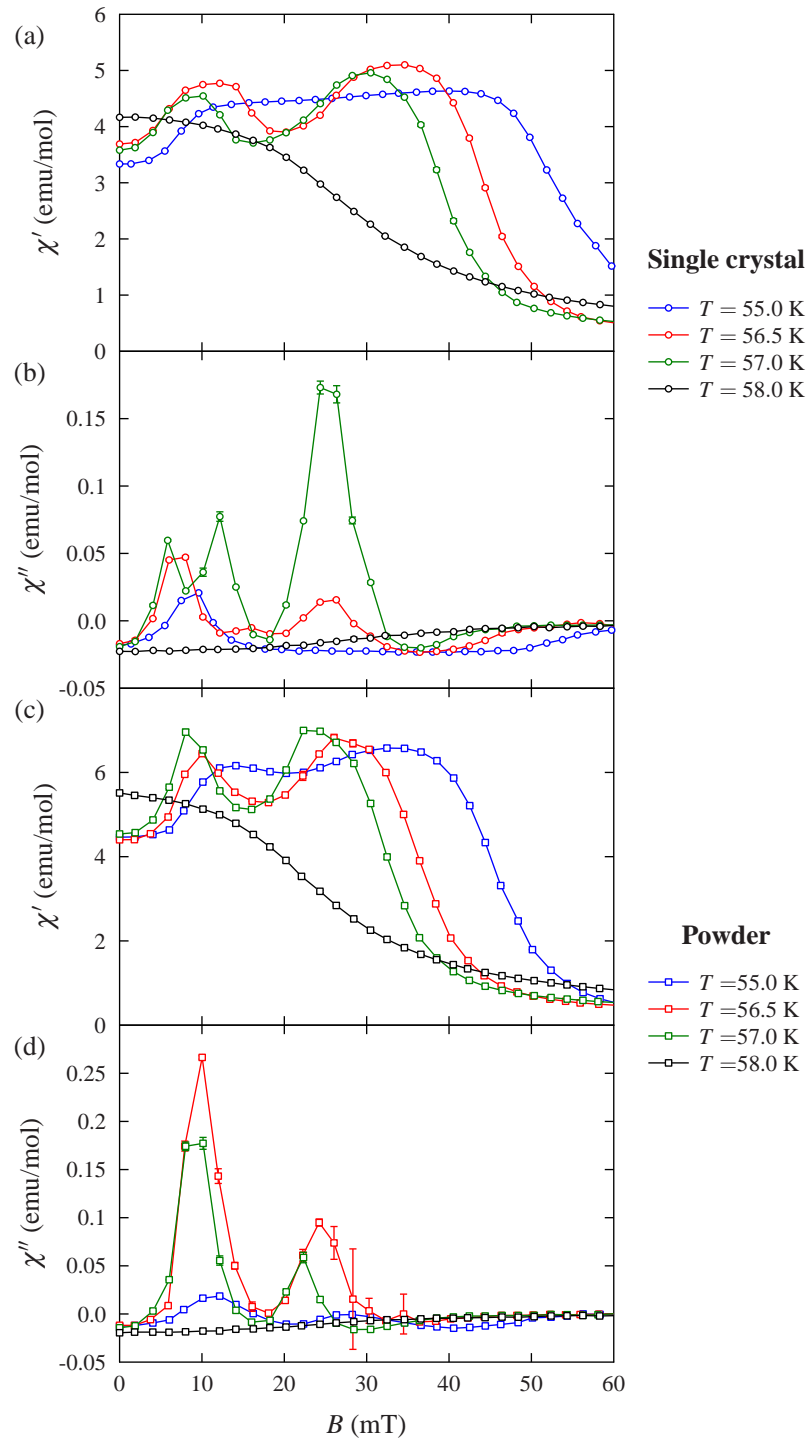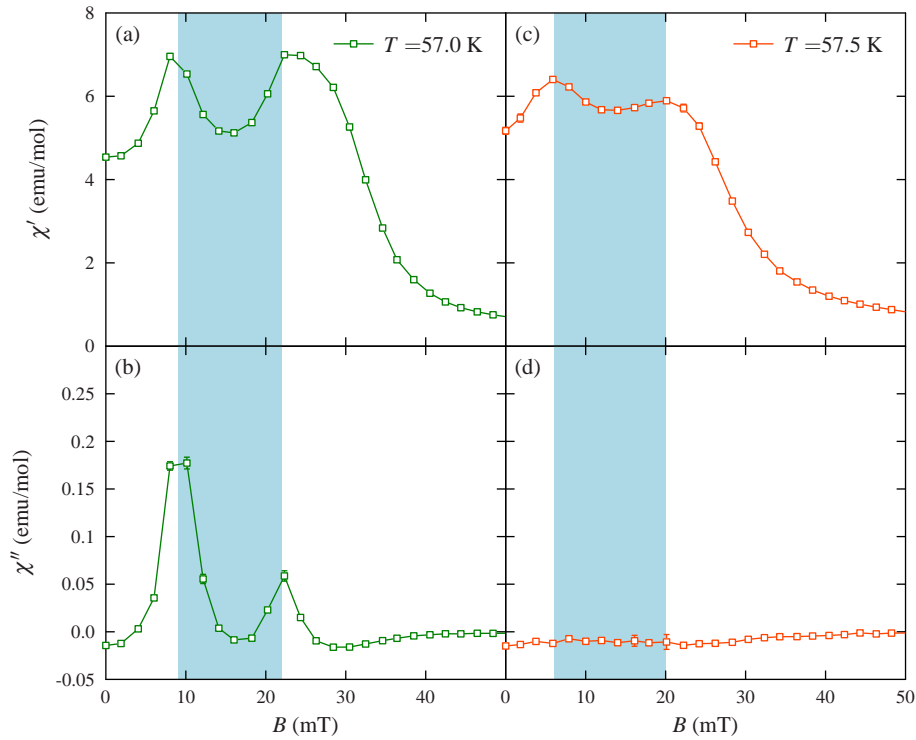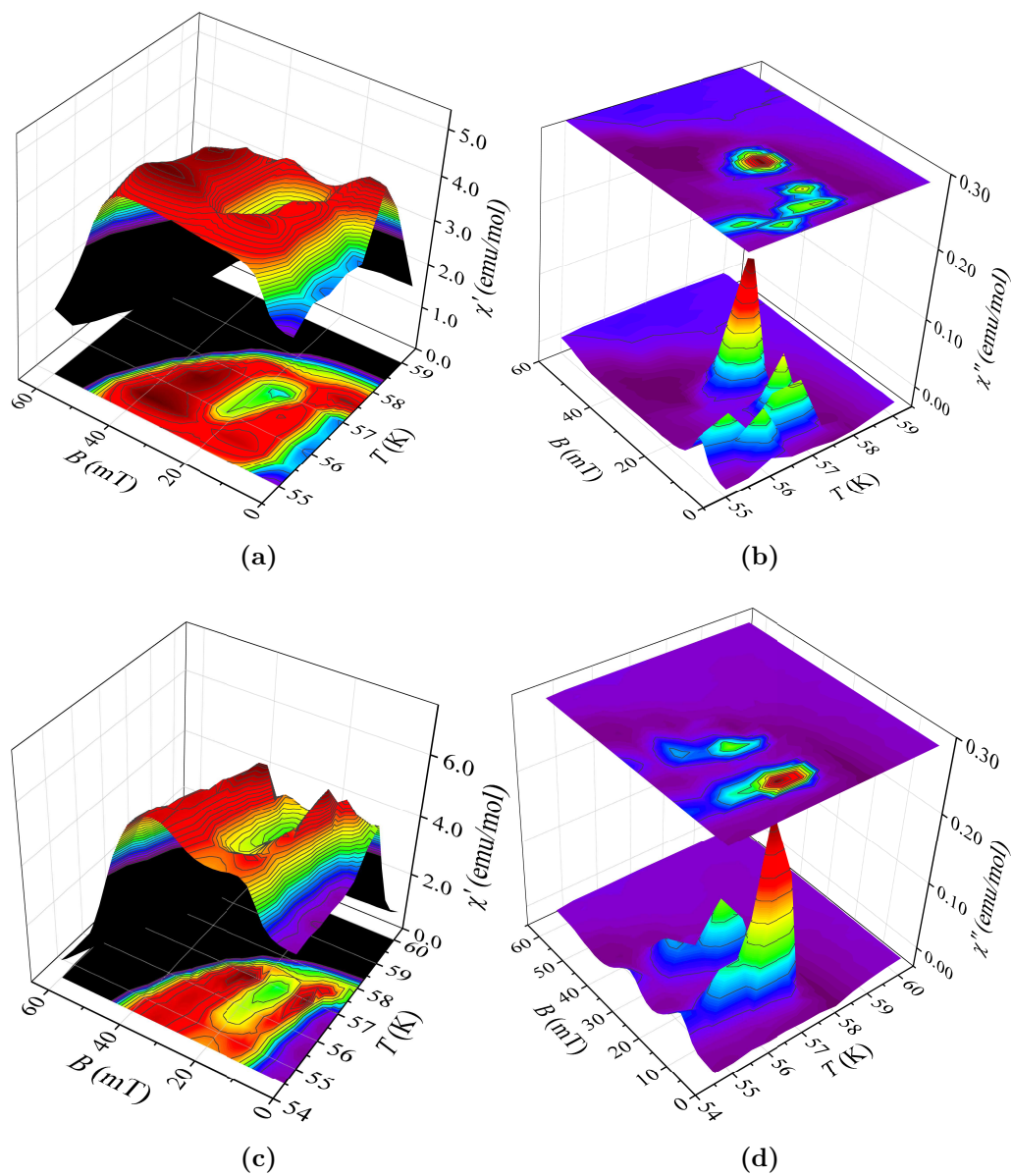
Figure 6.4: Magnetic field dependence of the real χ' and imaginary χ'' components of the molar AC susceptibility for single crystal [(a) and (b), respectively] and polycrystalline powder [(c) and (d), respectively] samples of Cu_2OSeO_3.

Figure 6.5: Magnetic field dependence of the (a), (c) real χ' and (b), (d) imaginary χ'' components of the molar AC susceptibility for polycrystalline powder samples of Cu_2OSeO_3. Data were measured at temperatures of (a), (b) 57 K and (c), (d) 57.5 K. The approximate SL phase region is highlighted for each temperature.

Field sweeps at temperatures lying below the lower boundary of the SL phase display a broad plateau coinciding with the single-q helical phase, lying between the multi-q (low field) and FiM (high field) phases (visible in the blue $T = 55.0$ K curves). For field sweeps which intersect the SL phase, a dip in χ' is present in this plateau, leading to a signal with a distinctive 'double hump' shape [see the red and green $T = 56.5, 57.0$ K curves in Fig. 6.4 (a), (c)]. Again, slight differences in the χ' response are apparent between the single crystal and powder samples, which may partly be ascribed to the effect of powder averaging of field orientations (relative to the crystal axes). Magnetic field orientation has previously been shown to relocate the A-Phase within the B–T plane [270, 271], which also suggests one might expect extra phase coexistence between crystallites in the powder sample, in addition to that expected within each crystallite near the boundaries of the A-phase (indicated by the LTEM results, described below).

In addition to the response of χ', it appears that a coincident suppression in

Figure 6.6: Magnetic field and temperature dependence of the real χ' and imaginary χ'' components of the molar AC susceptibility for single crystal [(a) and (b), respectively] and polycrystalline powder [(c) and (d), respectively] samples of Cu_2OSeO_3.

the imaginary component of the AC susceptibility χ'' is also able to identify the skyrmion phase in this compound, as illustrated for $T = 57$ K in the powder sample in Fig. 6.5(a), (b). However, the data suggest that this feature is less pronounced than that in χ' near the SL phase boundaries, as illustrated in Fig. 6.5(c), (d) for $T = 57.5$ K . This greater resolution in χ' is probably enhanced by the fact that the real, in phase, component of the sample magnetisation m' was found to be two orders of magnitude greater than the imaginary, out of phase, component m''. All of the AC susceptibility data may be combined to form 3D surface plots of χ' and χ'' in the B–T plane, as shown in Fig. 6.6. The SL phase is most readily identifiable as a depression in the real component of the AC susceptibility [Figs. 6.6(a) and (c)]. The location of this A-phase within the B–T plane is remarkably similar for the single crystal and polycrystalline powder samples; it appears that the effect of powder averaging has not severely broadened the features of the χ' surface. This similarity is perhaps made less surprising by the fact that crystallites in the powder sample are still large on the scale of the skyrmion spin texture (in Cu_2OSeO_3 the skyrmion wavelength is $L_{sk} = 50$ nm [270]), whereas phase diagrams derived for thin films use samples which have thickness of order L_{sk}.

I do not attempt to derive a phase diagram on the basis of these AC susceptibility measurements, since the samples measured here are small fragments of those used in the μSR study presented in Sec. 6.3 and, as discussed in Sec. 6.1.2, phase boundaries have been found to be sensitive to the exact sample geometry. Also, as discussed in Ref. [276], phase boundaries for a particular sample identified using χ' do not consistently agree with those determined by other experimental techniques, such as DC magnetisation.

To establish the existence of skyrmions in our Cu_2OSeO_3 samples, a thin film sample was prepared for electron microscopy by J. C. Loudon, University of Cambridge. A thinned crystal of approximate thickness 50 nm was obtained from a single crystal facet [a (110) face] using mechanical polishing and argon ion beam irradiation. LTEM images taken from this film are shown in Fig. 6.7 and confirm the presence of skyrmion spin textures. These occur over an extended region of the phase diagram, compared to results on bulk materials, as observed previously [270].
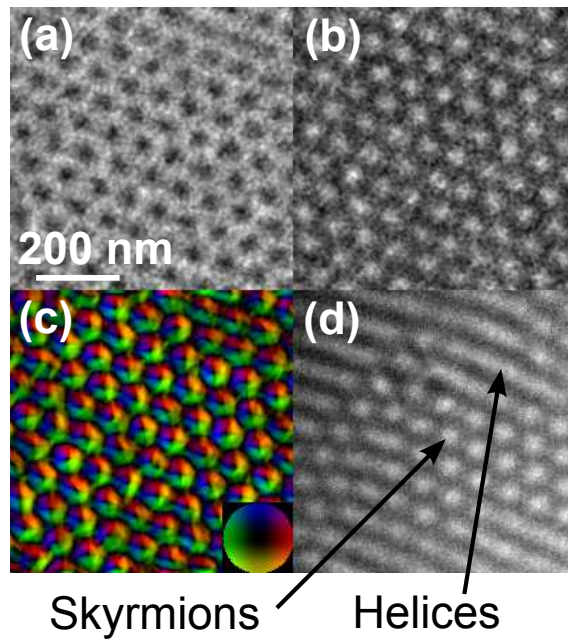
Figure 6.7: (a), (b) Skyrmions in Cu_2OSeO_3 imaged with LTEM at 10 K in a field of $B_0 = 30$ mT with defoci ± 0.7 mm. These images are obtained from a thin film (approximate thickness 50 nm) obtained from a single crystal from the same batch as the polycrystalline powder used in μSR measurements. (c) Magnetic induction map constructed from (a) and (b) using the transport of intensity equation. The direction of the local induction is indicated by the colour wheel (inset). (d) Skyrmions coexisting with the helical phase at 30 K in a field of $B_0 = 40$ mT. Similar observations were made by Seki *et al.* [270]. Figure taken from Ref. [234].

Also of interest is the coexistence of skyrmions and helices [Fig. 6.7(d)], as seen in the previous microscopy study [270].

6.3   TF μSR Measurements

TF μSR measurements on the polycrystalline powder sample were made using the MuSR spectrometer at the ISIS facility and the GPS spectrometer at the Swiss Muon Source (SμS). For measurements at ISIS the sample was mounted on a haematite backing plate in order that muons that are implanted in the haematite would be rapidly depolarised and therefore removed from the spectrum (Fe_2O_3 has large internal magnetic fields within the antiferromagnetic state for temperatures below the Morin temperature $T \approx 250$ K). For measurements at GPS the so-called 'flypast' geometry was employed, where the sample is suspended on a fork, which prevents
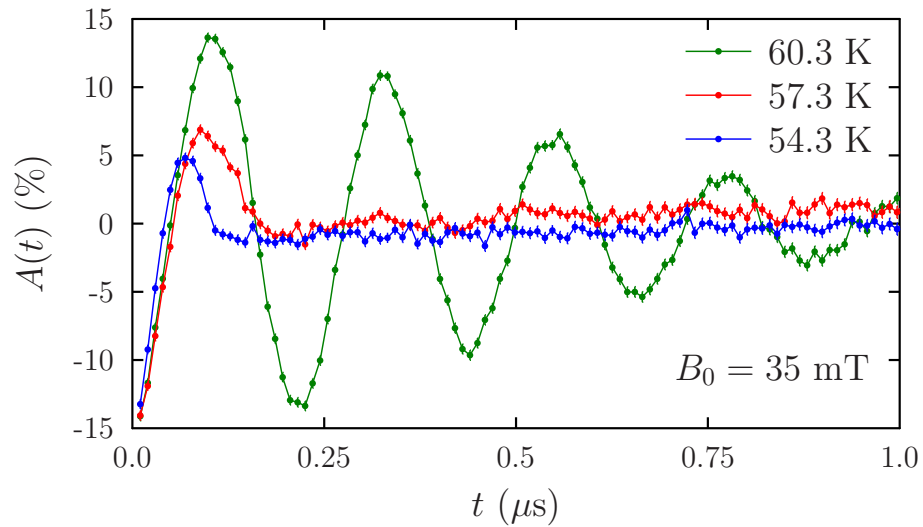
Figure 6.8: (a) Time domain spectra measured in an applied transverse magnetic field of $B_0 = 35$ mT in the paramagnetic phase at 60.3 K, the skyrmion phase at 57.3 K and the single-q phase at 54.3 K.

those muons that do not implant in the sample from contributing to the signal. For all measurements presented, the sample was cooled from $T > 60$ K in the applied field (using a continuous-flow helium-4 evaporation cryostat).

6.3.1 SμS Data

Example TF μSR time domain spectra measured at SμS are shown in Fig. 6.8, where the increase in damping upon entering a magnetically ordered phase (in this case the skyrmion and single-q phases) is evident. For our purposes, it is more instructive to consider the frequency domain spectra, as shown in Figs. 6.9 and 6.10. These were obtained via a fast Fourier transform of the time domain spectra, where the average was taken of the real components of the Fourier transformed data collected by each detector group, corrected for each of their relative phases to the initial muon polarisation direction. A Gaussian filter with time constant 2 μs was utilised during each transform, since this was found to best describe the envelope function of data measured in the paramagnetic phase (this is the least damped data measured, shown for example as the green data in Fig. 6.8). In these spectra the spectral density is proportional to $p(B)$.

It may be seen that spectra in the skyrmion phase (shown in red in Fig. 6.9)
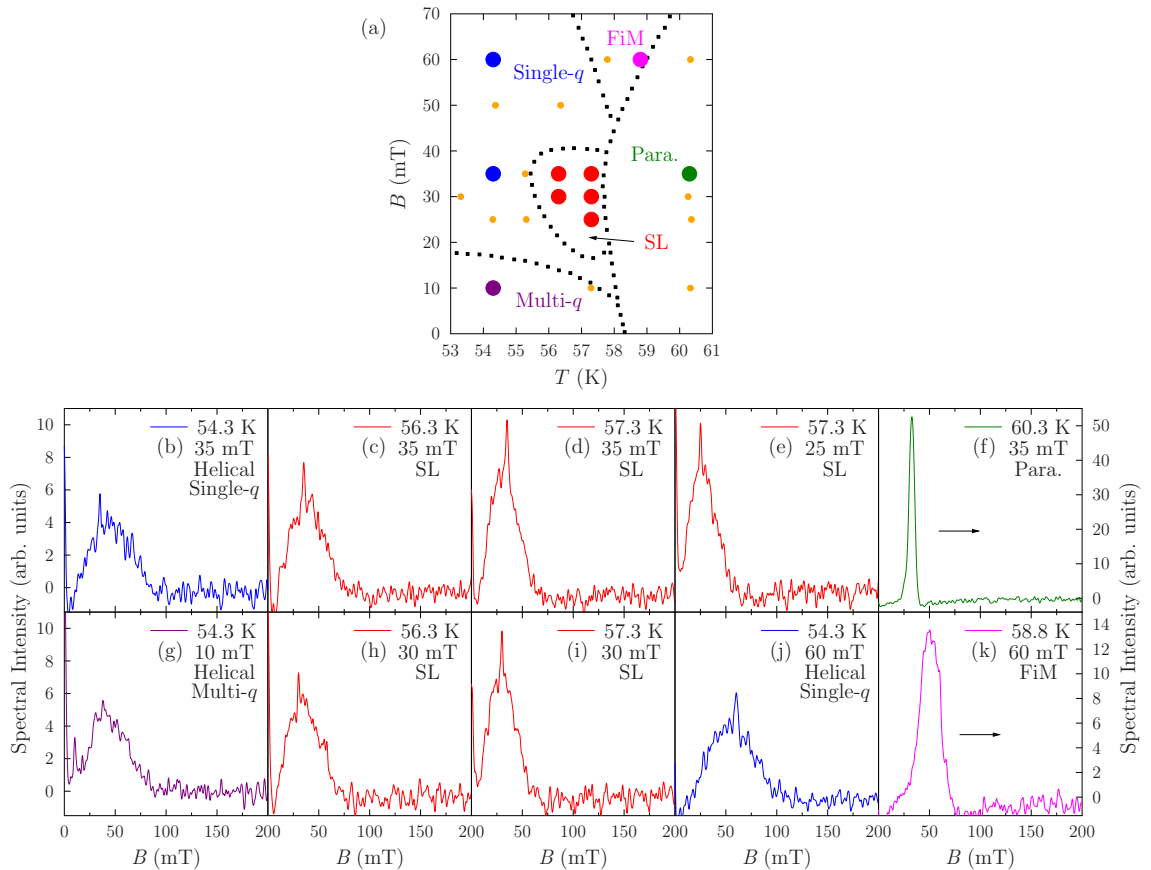
Figure 6.9: (a) The phase diagram of Cu_2OSeO_3. Small orange circles show where measurements were taken, and the bold circles correspond to the frequency spectra displayed in (b-k). (b-k) Evolution of the magnetic field distribution measured at SμS, with temperature and applied field. (b, j) Single-q helical phase; (c-e, h, i) the SL phase; (f) paramagnetic phase; (g) the multi-q helical phase; and (k) the FiM phase. All data are plotted to the same spectral intensity scale, except (f) and (k).

are characterised via a relatively narrow, asymmetric spectral density distribution, which rises steeply on the low field side leading to a sharp peak, when compared to spectra within the helical phases. This peak then decays, first very rapidly and then more gradually with increasing field. In contrast, the single- (blue) and multi-q (purple) helical phases give rise to less asymmetric distributions with broader maxima and spectral weight distributed over a larger range of fields. In further contrast, the ferrimagnetic phase (pink) shows a narrowed, fairly symmetric line; while the paramagnetic regime (green) is characterised by a very narrow linewidth (note the change of scale in Fig. 6.9 for spectra from these latter two phases).

Spectra in the single-q phase do not show a significant change with temperature
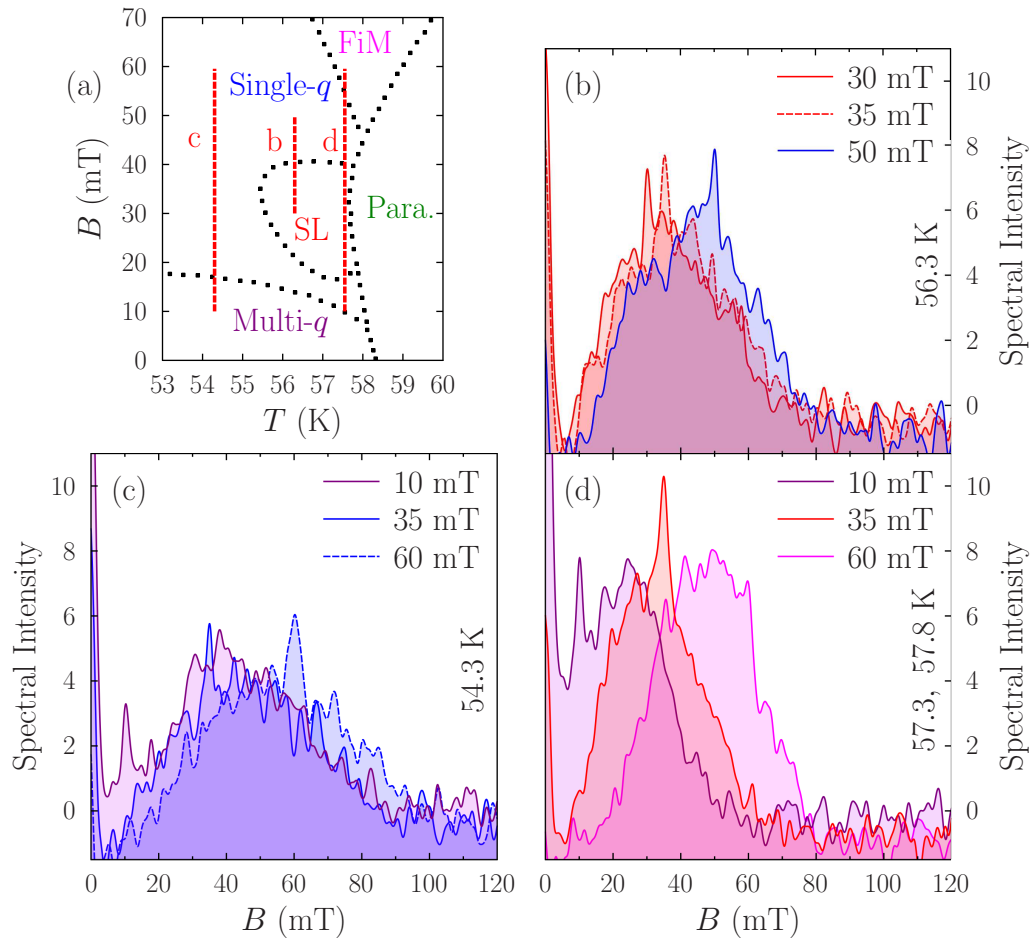
Figure 6.10: (a) The cuts through the phase diagram at constant temperature displayed in (b-d). (b) Applied magnetic field-dependence of the TF lineshape measured at $T = 56.3$ K. (c) Field sweep within the multi- and single-q phases at 54.3 K. (d) Field sweep through multi-q, SL and FiM phases.

below 55 K. However, as temperature is increased close to the transition to the paramagnetic region (Fig. 6.10), a temperature-driven effect is apparent in the single-q, multi-q and skyrmion regions, which causes the spectra to show more spectral weight at the applied field, taking on a more heavily peaked appearance. This effect is evident in several spectra [see e.g., Fig. 6.10(d)], but can be most clearly seen in the single-q phase data measured at 50 mT and 56.3 K [Fig. 6.10(b)] when compared to spectra measured at lower temperature in that phase [Fig. 6.10(c)], which are quite unresponsive to changes in applied field. However, comparing this latter single-q phase spectrum with those measured at the same temperature, but in fields thought to promote the SL phase [Fig. 6.10(b)], the spectra may still be distinguished: the
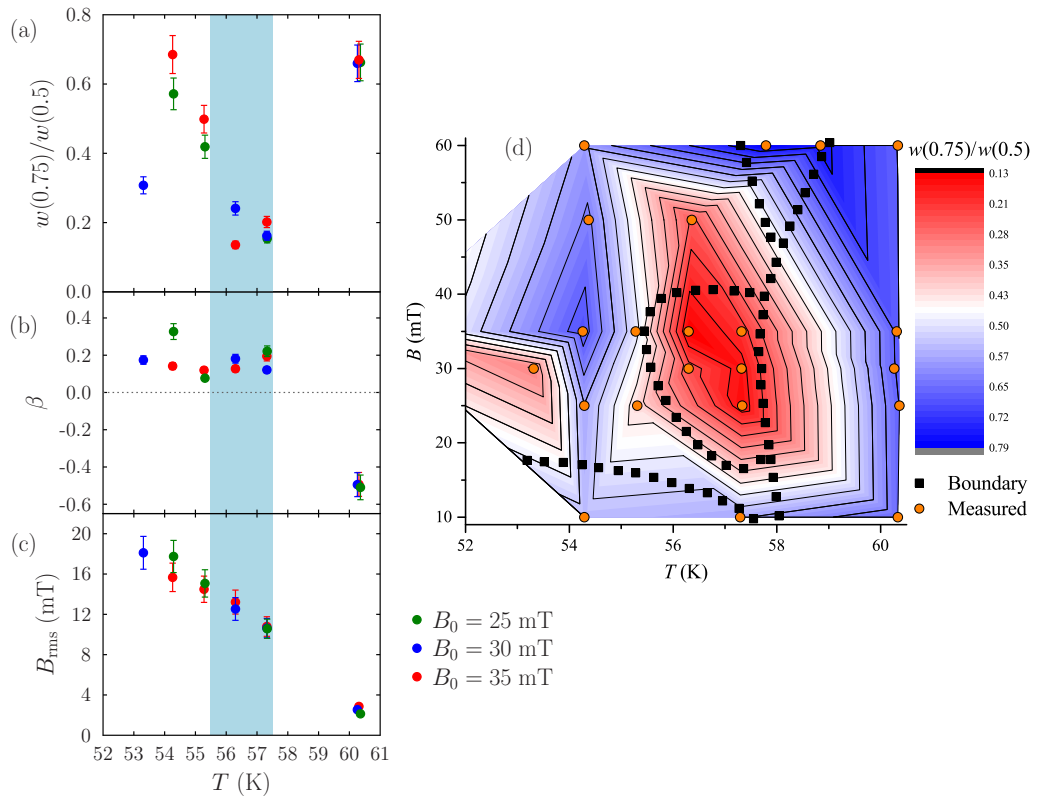
Figure 6.11: (a) The ratio of peak widths $w(0.75)/w(0.5)$ discussed in the text. (b) The skewness β and (c) standard deviation B_{rms} as a function of temperature. (d) Contour plot of $w(0.75)/w(0.5)$ from which the SL phase may be identified.

SL phase spectra are more asymmetric, with spectral weight persisting on the high field side of the peak. It is worth recalling that in the LTEM measurements there is evidence for the coexistence of skyrmions and helical spin textures [Fig. 6.7(d)]. It could be, therefore, the case that the data point in question ($B_0 = 50$ mT and $T = 56.3$ K), measured on a polycrystalline sample, features a contribution from both single-q and SL phases. However, it is also worth noting that the phase diagram of thinned samples supports the existence of skyrmions over a wider range of the B–T phase diagram than for the bulk, so the cases are not straightforwardly comparable.

One crude way to identify the SL region of the phase diagram from these data is via the relatively tapered lineshape observed in that phase. To this end, Fig. 6.11(a) shows one possible parametrisation of the data that approximately captures the characteristic signal in the SL region. Figure 6.11(a) shows the ratio of $w(0.75)$ (the full peak width at 0.75 of the maximum spectral weight) to $w(0.5)$ (the full width at half maximum). The contour plot in Fig. 6.11(d) shows that this quantity picks out

the SL phase as an island centered around 57 K and 30 mT where $w(0.75)/w(0.5)$ is suppressed. Moreover, despite the resolution of this contour plot being limited by the number of data points, it bears a striking resemblance to the skyrmion phase reported elsewhere (the phase boundaries illustrated in Fig. 6.11(d) are taken from Ref. [270]). Most of the spectra obtained outside of the paramagnetic region display a small additional peak at the value of the applied field, which is ascribed to the diamagnetic response from a small portion of the muon ensemble. This might cause a further suppression of $w(0.75)/w(0.5)$ within the SL phase, whose suppression is otherwise caused by the tapered nature of the lineshape, as the diamagnetic contribution coincides with the peak in spectral weight in the muon response caused by the internal field distribution. The limitation of this method is apparent, however, in that the data point at 50 mT and 56.3 K discussed above gives a rather similar ratio to the points in the SL region, despite its lineshape being distinguishable via its asymmetry. As described above, one interpretation of this spectrum involves some portion of the signal arising from skyrmions, but it remains distinct from the other spectra from the SL phase, suggesting that there is a significant single-q phase contribution.

The normalised skewness of the distribution β is shown in Fig. 6.11(b), defined via

$$\beta = \int \mathrm{d}B \, p(B) \left[\frac{B - \langle B \rangle}{B_{\mathrm{rms}}} \right]^3 , \tag{6.4}$$

where

$$B_{\mathrm{rms}} = \sqrt{\langle (B - \langle B \rangle)^2 \rangle} = \left(\int \mathrm{d}B \, p(B) \, [B - \langle B \rangle]^2 \right)^{1/2} \tag{6.5}$$

is the standard deviation of the distribution, and

$$\langle B \rangle = \int \mathrm{d}B \, p(B) \, B \tag{6.6}$$

is the average magnetic field of the normalised distribution $p(B)$. It may be seen that β is similar in both the SL and single-q phases, but drops to a negative value in the paramagnetic phase. Finally, the standard deviation of the distribution increases fairly smoothly with decreasing temperature, but is less sensitive to the SL phase boundaries [Fig. 6.11(c)].

These results suggest that TF μSR is sensitive to the SL phase through the muon lineshape. Assuming that this is the case one may consider the mechanisms for muon relaxation and the time scales involved. In contrast to muon spectroscopy, neutron measurements of the SL are insensitive to fluctuations on time scales much slower than $\hbar/\Delta E \approx 10^{-11}$ s (where $\Delta E \approx 1$ meV is the energy scale of the resolution of the measurement) and so fluctuations on time scales longer than this appear static. Neutrons therefore take a 'snapshot' of the behaviour compared to μSR measurements whose characteristic time scale is set by the gyromagnetic ratio of the muon ($\gamma_\mu = 2\pi \times 135.5$ MHz T^{-1}, see Sec. 2.2.3). The sensitivity of the muon to the SL would imply that the signal from the long-range spin texture is not significantly motionally narrowed, which further implies that the SL itself is likely to be quasistatic on time scales $\tau \gg (1/\gamma_\mu B_{\mathrm{rms}}) > 100$ ns. This is consistent with the long length scale dynamics observed via Lorentz microscopy [292], which suggest rotations of the skyrmion texture take place on a 0.1 s time scale. The observation that the muon signal below T_{c} is dominated by the distribution of static internal magnetic fields is consistent with the results of the previous zero-field μSR study of this material [279]. Those measurements showed sizeable transverse relaxation of the muon precession signal, which decreased as the transition was approached from below, consistent with the decrease of the internal field with increasing temperature. This was accompanied by an increase in a small longitudinal relaxation rate, suggesting a slowing of residual dynamic fluctuations above 50 K (i.e., in the region of interest for our study). It might be expected that the nature of the dynamics changes in each of the magnetic phases. However, the contribution to the muon lineshape from the dynamic effects would seem to make only a small contribution to the overall shape.

6.3.2 ISIS Data

Further TF measurements were also made on a powder sample at ISIS using the MuSR instrument. In this case, similar responses are obtained as those reported above, although the analysis of these data are complicated by a sizeable background contribution from muons stopping in the sample holder, haematite backing plate or cryostat tails. Example frequency spectra, obtained via maximum entropy analysis of
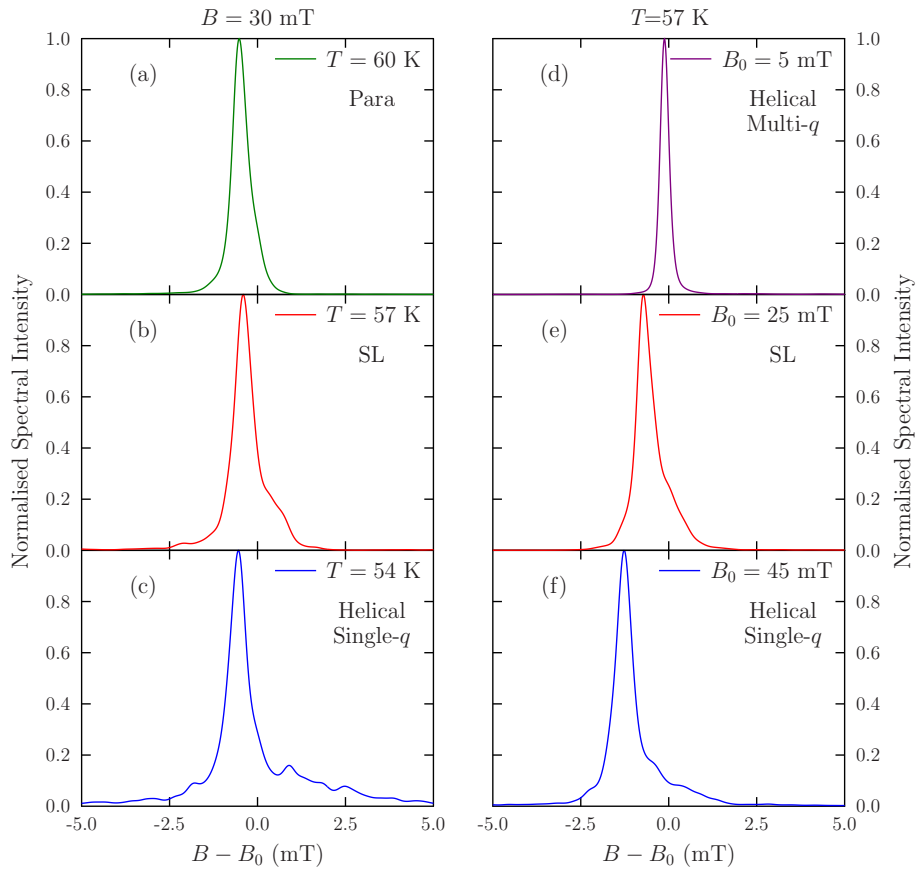
Figure 6.12: Evolution of the magnetic field distribution (relative to the applied field B_0) measured at ISIS for measurements made on a powder sample in a field of $B_0 = 30$ mT (a-c) and at a temperature of 57 K (d-f). (a) Paramagnetic phase; (b, e) The SL phase; (c, f) single-q helical phase; and (d) multi-q phase.

the measured time domain spectra [293–296], are shown in Fig. 6.12 for cuts through the SL phase in both field and temperature. In these plots it may be seen that a knee in the spectrum develops in the SL phase [red spectra in Fig. 6.12(b), (e)] on the high field side of the peak region [compared to the relatively narrow peaked response in the paramagnetic phase, Fig. 6.12(a)]. This corresponds to the slow decay of the lineshape in high field seen in the SμS data in Fig. 6.9. This feature is lost upon entrance to the single-q phase [blue spectra in Fig. 6.12(c), (f)], where the spectral weight in the knee is seen to decay into a broad distribution. In the multi-q phase, the line is seen to be very narrow, suggesting that the background contribution is dominant in this case [purple spectrum in Fig. 6.12(d)].

Measurements were repeated on other batches of powder sample, which showed some slight deviations in the position of the phase boundary to the paramagnetic

phase, which is attributed to sample variability. Measurements were also made at ISIS on mosaics of unoriented single crystal samples, which show consistent results, although the lack of angular averaging and some sample variability makes a detailed comparison difficult.

6.4   Discussion

In order to understand these μSR results, a colleague in Durham (I. O. Thomas) simulated the expected distribution $p(B)$ for the spin configurations of the various magnetic phases of Cu_2OSeO_3. Owing to the complexity of the problem in a system with multiple muon sites and a complicated FiM spin configuration, expected field distributions were simulated for a single crystal orientation, with the applied magnetic field along [001]. For simplicity skyrmion spin textures generated here employed the 3–q approach (discussed in Sec. 6.1.2, and outlined in detail below), and canting of spins in the presence of an applied magnetic field (resulting in a net magnetisation [270, 271, 291]) has not been included.

For these simulations the SL and helical spin configurations were evaluated as follows:

- Skyrmion-like spin configurations were generated using $\boldsymbol{m}(\boldsymbol{r}) = \boldsymbol{m}_{\mathrm{sk}}(\boldsymbol{r})/|\boldsymbol{m}_{\mathrm{sk}}(\boldsymbol{r})|$ where

$$\boldsymbol{m}_{\mathrm{sk}}(\boldsymbol{r}) = \sum_{i=1}^{3} \left[\hat{\boldsymbol{e}}_z \cos(\boldsymbol{q}_i \cdot \boldsymbol{r} + \pi) + \hat{\boldsymbol{e}}_i \sin(\boldsymbol{q}_i \cdot \boldsymbol{r} + \pi) \right]. \qquad (6.7)$$

Here, $\boldsymbol{q}_i$ are the SL modulation vectors, taken to be perpendicular to the applied field B_0 ($\parallel \hat{\boldsymbol{e}}_z$), and $\hat{\boldsymbol{e}}_i$ are the unit vectors of the skyrmion lattice (also perpendicular to B_0) [247, 291] . A skyrmion lattice magnetisation texture is generated in the [110] plane by taking $\boldsymbol{q}_1 = F(-1, 0, 0)$, $\boldsymbol{q}_2 = F(\frac{1}{2}, -\frac{\sqrt{3}}{2}, 0)$, $\boldsymbol{q}_3 = F(\frac{1}{2}, \frac{\sqrt{3}}{2}, 0)$, $\hat{\boldsymbol{e}}_1 = (0, 1, 0)$, $\hat{\boldsymbol{e}}_2 = (-\frac{\sqrt{3}}{2}, -\frac{1}{2}, 0)$ and $\hat{\boldsymbol{e}}_3 = (\frac{\sqrt{3}}{2}, -\frac{1}{2}, 0)$, where $F = 2\pi/L_{\mathrm{sk}}$ and L_{sk} is the skyrmion wavelength, taken to be $L_{\mathrm{sk}} = 70$ unit cells, similar to that suggested in Ref. [271]. By reversing the spin on the Cu1 sites, FiM configurations are generated, which results in textures that match the observed magnetic structures of the system introduced in Sec. 6.1.2.

- Single-q helical configurations were calculated for B_0 parallel to the [001] direction using [291]:

$$\boldsymbol{m}(\boldsymbol{r}) = \left[\hat{\boldsymbol{e}}_x \cos(q_z z) + \hat{\boldsymbol{e}}_y \sin(q_z z)\right], \tag{6.8}$$

where $q_z = 2\pi/L_{\text{sk}}$. Reversing the Cu1 spin direction again generates the required FiM configuration.

- The exact spin configuration of the more complicated multi-q phase is not confirmed and so a trial structure was investigated. This phase was modelled by calculating and averaging over the field distributions for FiM configurations reflecting six possible domains, each with equal population. Each domain has $\boldsymbol{q}$ either parallel or antiparallel to the [100], [010] or [001] axes. Its texture is given by a generalised version of Eq. 6.8:

$$\boldsymbol{m}(\boldsymbol{r}) = \left[\hat{\boldsymbol{e}}_i \cos(\boldsymbol{q} \cdot \boldsymbol{r}) + \hat{\boldsymbol{e}}_j \sin(\boldsymbol{q} \cdot \boldsymbol{r})\right], \tag{6.9}$$

where $\hat{\boldsymbol{e}}_i$ and $\hat{\boldsymbol{e}}_j$ are unit vectors in the plane perpendicular to $\boldsymbol{q}$ and $\boldsymbol{q} = \pm\hat{\boldsymbol{e}}_q|\boldsymbol{q}|$ for the parallel and antiparallel cases respectively. Here $\hat{\boldsymbol{e}}_q$ is the unit vector in the direction of $\boldsymbol{q}$ and $|\boldsymbol{q}| = 2\pi/L_{\text{sk}}$.

In order to generate simulated field distributions $p(B)$ from these spin configurations, it is assumed muons couple to the dipolar magnetic fields of the Cu^{2+} spins in the material. The total magnetic field component B^i at a position $\boldsymbol{r}$ is given by the sum of the dipolar contribution and externally applied field [26, 120, 279]:

$$B^i(\boldsymbol{r}) = \frac{C\mu_{\text{B}}\mu_0}{4\pi} \sum_{n,j} \frac{m^j(\boldsymbol{r}_n)}{R_n^3} \left(\frac{3R_n^i R_n^j}{R_n^2} - \delta^{ij}\right) + B_0^i, \tag{6.10}$$

where i and j run over all three cartesian directions, n labels a Cu ion at position $\boldsymbol{r}_n$, C scales the magnetic moment to match the previously observed Cu ion magnetic moment $0.25\mu_{\text{B}}$ [277] and $\boldsymbol{R}_n = \boldsymbol{r} - \boldsymbol{r}_n$. A previous zero field μSR study of this material [279] found five muon stopping sites in each chemical unit cell at positions $A = (0.215, 0.700, 0.970)$, $B = (0.035, 0.720, 0.805)$, $C = (0.195, 0.555, 0.795)$, $D = (0.275, 0.295, 0.460)$ and $E = (0.635, 0.550, 0.525)$. Assuming these muon sites are populated with equal probabilities, the field distribution $p(B)$ is simulated in each of
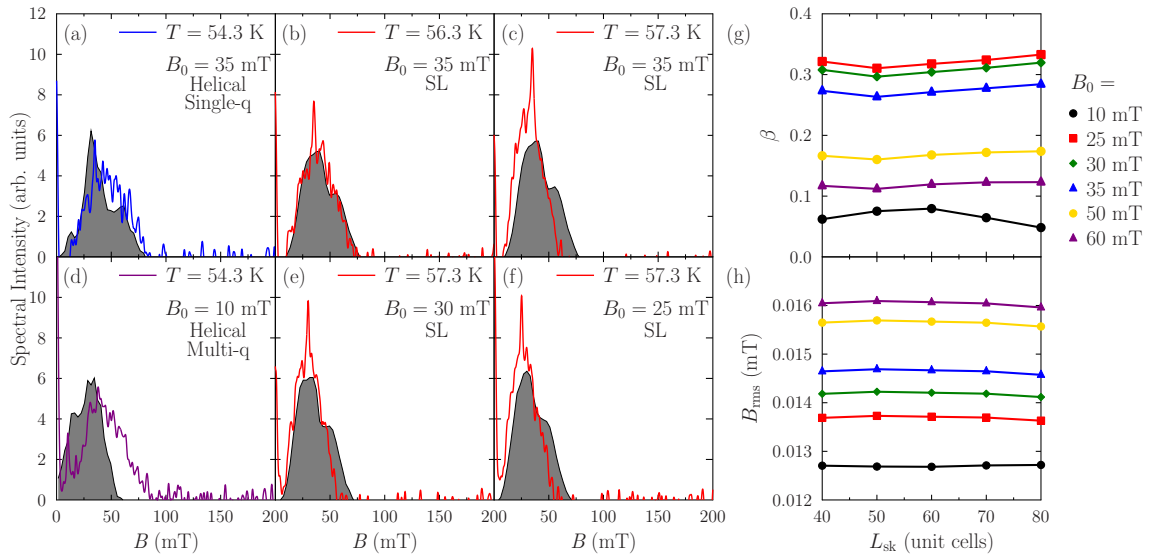
Figure 6.13: (a-f) Results of dipole simulations of $p(B)$ in each phase (shown shaded) compared with the spectra measured at SμS. In order to compare the simulation and experiment, the area under the simulated distribution is scaled to that under the experimental distribution, assuming a constant background contribution. Scaling of the (g) skewness and (h) B_{rms} of the simulated distribution with the skyrmion lattice length scale L_{sk}.

the phases at a variety of applied magnetic fields. For comparison with the measured spectra, the distributions were convolved with a simulated instrument function, generated with the WiMDA program.

The results of these simulations are compared with the observed spectra in Fig. 6.13, where the simulated response is summed over each of the five muon stopping sites A–E (assuming an equal population of each). This comparison shows that the simulations capture the lineshape in the skyrmion regime quite well and are distinguishable from the predicted lineshapes in the other magnetic phases. Although the agreement for the single-q helical phase is reasonable, a discrepancy is evident in the multi-q helical phase, as might be expected if the trial structure is not the correct one. (It is possible in this case that an alternative trial structure would produce results that match the measured spectra more closely.) These results appear to be consistent with magnetic moments being localised on the Cu^{2+} ions, as was previously found from x-ray measurements [273], although it is possible that a delocalised arrangement would match the data more closely in the multi-q phase.

The simulations may also be used to test whether the muon lineshape has a
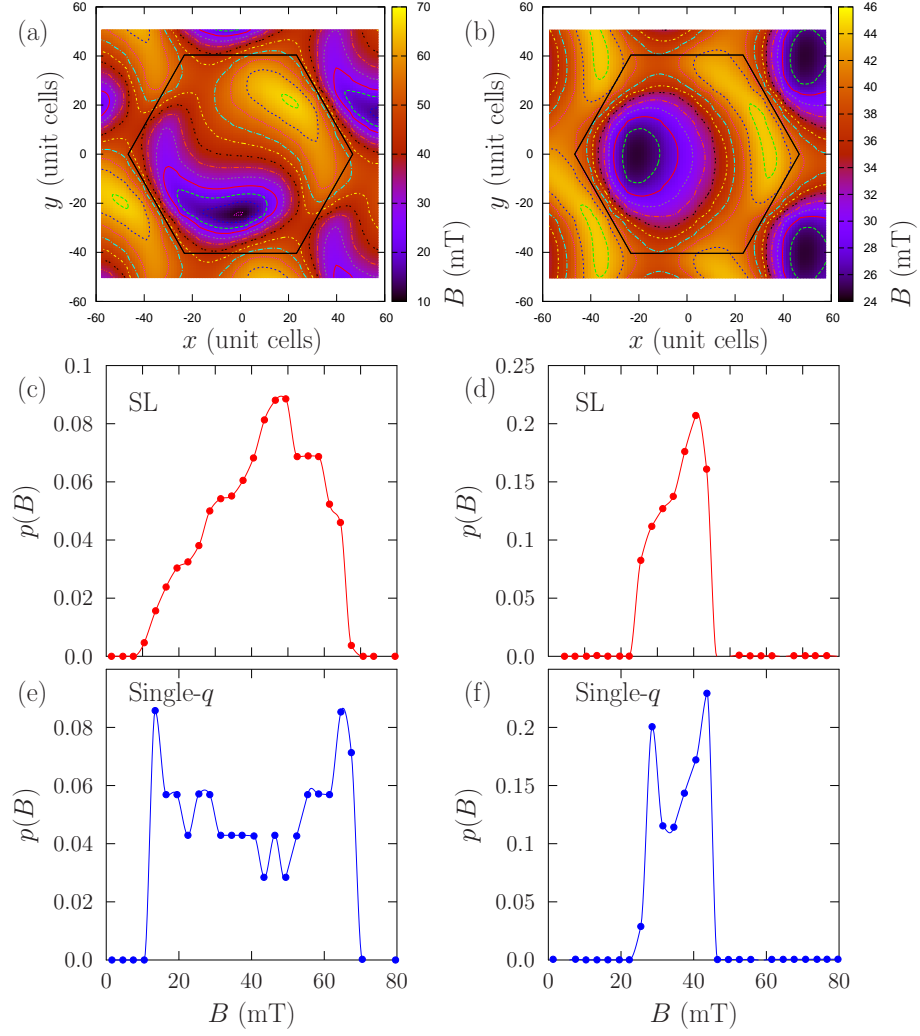
Figure 6.14: The magnitude of the dipole field at the (a) A and (b) E muon sites due to a skyrmion in an applied field of $B_0 = 35$ mT. Field distribution for the SL and single-q helical phases at A [(c) and (e), respectively] and E [(d) and (f), respectively] sites.

sensitivity to the length scale L_{sk} that characterises the SL. Plots of the width B_{rms} and skewness β against L_{sk} are shown in Fig. 6.13 for various applied field strengths, which reveal that there is little variation with L_{sk}. It would therefore be difficult for this system to determine L_{sk} in the absence of other detailed information about the phase, such as the magnetic structure, muon sites and moment sizes.

To gain some insight into how the field distributions shown in Fig. 6.13 arise from the SL phase spin textures, one may consider the dipole fields produced by a skyrmion at each individual class of muon site. In Cu_2OSeO_3 this is complicated by the large number of inequivalent muon sites [279] and the ferrimagnetic arrangements

of Cu^{2+} spins that forms the basis of the skyrmion spin texture. Figure 6.14(a) and (b) show examples of the magnitude of the dipole field found at two of the five crystallographically distinct muon sites, evaluated across a single skyrmion. The corresponding field distribution $p(B)$ derived from each is also shown [Fig. 6.14(c) and (d)]. The skyrmion texture is shown to give rise to an asymmetric field distribution at each site, with spectral weight skewed towards high fields. When summed over all muon sites these individual distributions produce the total $p(B)$ distribution shown in Fig. 6.13. These distributions may be contrasted with those found in the single-q helical phase [Fig. 6.14(e) and (f)], which are more symmetrical. It is difficult from these results to make general predictions regarding the dipole field distribution expected from other skyrmion materials, beyond the expectation of asymmetric field distributions at each muon site. The apparent complexity of SL spectra is in marked contrast to the relative simplicity of the VL spectrum, where characteristic spectral features map directly onto special positions within the VL (see Fig. 2.6 in Sec. 2.4.3).

6.5 Conclusion and Further Work

In conclusion, the results of TF μSR measurements have been presented that suggest that the technique is sensitive to the skyrmion lattice via measurements similar to those carried out on the vortex lattice in type II superconductors. This would imply that in Cu_2OSeO_3 the SL is static on a time scale $\tau > 100$ ns. Independent work, currently being prepared for publication [297], demonstrates that longitudinal field μSR measurements [36] are also sensitive to the skyrmion phase via changes in the spin dynamics. Taken together, these results suggest that in favourable cases μSR could be utilised as a method for identifying skyrmionic materials, characterising the behaviour of the skyrmion lattice and deriving their phase diagrams.

Cu_2OSeO_3 is an insulator, and so does not exhibit the phenomena accompanying conduction electrons discussed in Sec. 6.1.1. In contrast, insulating skyrmion systems display multiferroic behaviour where the coexistence of magnetic and electric polar orders permits the manipulation of magnetic textures via electric fields without ohmic heating [298]. Such nondissipative electronic control of nanoscopic magnetic objects

would also be very useful in spintronic devices. Magnetoelectric coupling in Cu_2OSeO_3 was explored soon after the initial discovery of skyrmions in this compound [274, 291] and electric field control of the SL in this system was also demonstrated [299, 300], including the manipulation of the entire lattice [292]. Multiferroicity is also present in the Néel-type skyrmion material GaV_4S_8 [301]. The recent discovery of a skyrmion host in a different family of cubic chiral magnets (distinct to the B20 class), which exhibits skyrmions above room temperature [302], and also the development of artificial skyrmion systems [303] both encourage optimism for a role for skyrmions in future spintronic applications.

Spintronic applications (whether in conducting or multiferroic materials) will most likely depend on devices comprising thin films or nanowires, in order to capitalise on the larger SL phase within the B–T plane, and to keep the devices compact. There is therefore motivation for the use of μSR to study SL phases within thin films samples, utilising the LEM instrument at SμS. The first study of this kind has already been performed on epitaxially grown MnSi thin films [304]. This case study is of particular interest due to the controversy surrounding epitaxial films of MnSi. That is to say, there is intense debate over the origin of an anomalous topoligical Hall effect, and whether LTEM images are sensitive to magnetic structures or in fact exhibit moiré fringes arising through tensile strain due to the sample–substrate lattice mismatch [305–309].

7

Conclusion and Further Work

Collectively, the results presented in this thesis have demonstrated the use of muon-spin spectroscopy as a sensitive local probe of static and dynamic magnetism in correlated magnetic oxides. One major advantage of employing μSR measurements in the study of such materials is the time scale of fluctuations to which it is sensitive; the gyromagnetic ratio of the muon is such that μSR has a dynamic window which is both distinct and complementary to those of other experimental techniques such as magnetisation and neutron scattering (see Sec. 2.2.3). This asset was particularly apparent in the study of the double perovskite Sr_2CoOsO_6 in Chap. 3, where exotic lattice-site-specific dynamics leads to several non-trivial, partially ordered magnetic structures. The results of the muon investigation into the tetrahedral spin-chain oxide $CsCoO_2$, in Chap. 4, helped elucidate a complex freezing of dynamics which were found to accompany a structural distortion that impacts upon magnetic superexchange pathways. In addition, μSR was able to probe the magnetic ordering

and dynamics within the antiferromagnetic layered perovskite series $La_{2-x}Sr_xCoO_4$, leading to a revised magnetic phase diagram for this system, presented in in Chap. 5. This series is believed to host intriguing charge and spin ordered stripe phases, and these results reveal a rich phase diagram which shares some common characteristics with those of its superconducting cuprate analogues.

Another application of μSR is the use of the transverse field geometry to examine static magnetic field distributions, which has proved highly successful in the vortex lattice state of Type II superconductors. In Chap. 6, results were presented of the first 'proof of principle' investigation which extended this principle to another topological phase in condensed matter physics, the skyrmion lattice (SL). Here, the muon response to the SL phase of Cu_2OSeO_3 was investigated, which was found to be identifiable by its frequency domain lineshape. This outcome, despite the complex ferrimagnetic spin arrangements found in this material, encourages optimism for the use of μSR to add new insight into other SL hosting materials. Experiments are under way at ISIS investigating the use of longitudinal field μSR to probe slow dynamics within the SL phase of $Co_8Zn_8Mn_4$, which crystallises in the β-Mn-type structure, distinct to the B20 group [302]. The sensitivity of this technique to the SL phase has been previously demonstrated [297], and it is expected that the SL should promote emergent low-energy excitations. Other future projects include μSR measurements of the newly realised Néel-type SL in GaV_4S_8, in order to increase our understanding of the role μSR might play in studying this exciting branch of topological condensed matter.

Muon-spin spectroscopy continues to develop and mature as a technique, aided by technological advancements in experimental instruments. However, uncertainty in the precise muon stopping site remains the single greatest limitation in the interpretation of μSR data. This detailed knowledge is not essential in many circumstances, for example when identifying temperatures where magnetic behaviour changes abruptly or investigating magnetic field distributions with large periodicity which vary smoothly on the length scale of the crystal unit cell (such as the vortex lattice discussed in Sec. 2.4.3). However, as has become clear for the materials studied within this thesis, a deeper *quantitative* understanding of the nature of magnetic

structures and dynamics becomes achievable once the researcher has a greater degree of certainty over the location of the muon.

The most widely adopted and straightforward method of identifying candidate muon stopping sites is to use dipole field calculations. Here, experimentally observed magnetic field strengths (as evidenced by the precession frequencies observed in the asymmetry data) are compared to simulated field textures arising due to dipolar fields within the magnetic unit cell in order to locate potential stopping sites. Alternatively, interactions between the muon and nuclear dipole (and quadrupole) moments may also be analysed to investigated the location of the muon [36,225]. As an advancement to this treatment, the Bayesian analysis introduced in Chap. 4 is a computationally inexpensive way to assess where the muon is *likely* to reside within the unit cell, *given* the local magnetic field strengths experienced by the muon ensemble. Furthermore, probabilistic constraints may be inferred to improve upon *a priori* assumptions regarding plausible ordered moment sizes and magnetic structures, as demonstrated by Steele *et al.* in Ref. [104]. At the very least, this technique provides an elegant basis for self-consistency arguments to ensure conclusions drawn from muon measurements are consonant with those of other techniques. This was the case for $CsCoO_2$ in Chap. 4, where the μSR data was found to agree well with ordered moment sizes and spin structures determined using neutron diffraction experiments and *ab initio* electronic structure calculations.

In the TF μSR study of the SL within Cu_2OSeO_3, in Chap. 6, candidate muon sites previously identified via dipole field calculations in conjunction with ZF μSR measurements [279] were utilised to simulate internal field distributions $p(B)$ for complex skyrmion spin structures. Within the large skyrmion magnetic unit cell the Cu moments are themselves arranged ferrimagnetically within the crystal unit cell, as discussed in Sec. 6.1.2. This additional complication, together with the complex nature of dipole fields relative to fields arising due to screening currents in superconductor vortex lattices, means $p(B)$ varies dramatically depending on which muon site is considered. Since there is no available information to assess the relative energies and occupancies of the five proposed sites, it is difficult to simulate the overall response from a full muon ensemble. As for the example of $CsCoO_2$ discussed

above, the muon is again assumed to be an innocent probe within the sample; the extent to which the muon perturbs its local electronic and crystal environment is not considered.

The most significant advancements in addressing these limitations comes from density functional theory, as introduced in Chap. 3. Here, calculations are performed where the muon and ions are permitted to relax, and the energies of resultant arrangements may be assessed energetically. Together, these considerations allow one to identify classes of muon sites, their relative likelihoods and subsequent perturbations on the host material. This approach can also be extended to treat the muon as a quantum mechanical impurity [310] and may be applied to diamagnetic and paramagnetic (including bound electron-muon states known as muonium, see Sec. 2.3). Continuing development of electron structure methods combined with the ever-increasing capabilities of computational resources will allow more ubiquitous use of this technique in the future, with greater accuracy and detail.

Bibliography

[1] P. W. Anderson, Science **177**, 393 (1972).

[2] A. Altland and B. Simons, *Condensed Matter Field Theory* (Cambridge University Press, 2010).

[3] J. J. Binney, N. J. Dowrick, A. J. Fisher, and M. E. J. Newman, *The Theory of Critical Phenomena: An Introduction to the Renormalization Group* (Clarendon Press, 1992).

[4] T. Lancaster and S. J. Blundell, *Quantum Field Theory for the Gifted Amateur* (Oxford University Press, 2014).

[5] N. D. Mermin, Rev. Mod. Phys. **51**, 591 (1979).

[6] K. Yosida, *Theory of Magnetism* (Springer Science & Business Media, 1996).

[7] S. J. Blundell, *Magnetism in Condensed Matter* (Oxford University Press, 2001).

[8] P. Coleman and A. J. Schofield, Nature **433**, 226 (2005).

[9] W. Witczak-Krempa, G. Chen, Y. B. Kim, and L. Balents, Annu. Rev. Condens. Matter Phys. **5**, 57 (2014).

[10] J. G. Rau, E. K.-H. Lee, and H.-Y. Kee, Annu. Rev. Condens. Matter Phys. **7**, 195 (2016).

[11] E. Fradkin, S. A. Kivelson, and J. M. Tranquada, Rev. Mod. Phys. **87**, 457 (2015).

[12] H. Ulbrich and M. Braden, Phys. C Supercond. **481**, 31 (2012).

[13] T. D. Lee and C. N. Yang, Phys. Rev. **104**, 254 (1956).

[14] C. S. Wu, E. Ambler, R. W. Hayward, D. D. Hoppes, and R. P. Hudson, Phys.

Rev. **105**, 1413 (1957).

[15] R. L. Garwin, L. M. Lederman, and M. Weinrich, Phys. Rev. **105**, 1415 (1957).

[16] R. L. Garwin, Phys. B Condens. Matter **326**, 1 (2003).

[17] R. A. Swanson, Phys. Rev. **112**, 580 (1958).

[18] E. Roduner, Appl. Magn. Reson. **13**, 1 (1997).

[19] S. P. Cottrell, S. F. J. Cox, J. S. Lord, and C. A. Scott, Appl. Magn. Reson. **15**, 469 (1998).

[20] T. D. Lee and C. N. Yang, Phys. Rev. **105**, 1671 (1957).

[21] K. Hagiwara, A. D. Martin, D. Nomura, and T. Teubner, Phys. Rev. D **69**, 093003 (2004).

[22] J. Beringer, J.-F. Arguin, R. M. Barnett, K. Copic, O. Dahl, D. E. Groom, C.-J. Lin, J. Lys, H. Murayama, C. G. Wohl, W.-M. Yao, P. A. Zyla, *et al.*, Phys. Rev. D **86**, 010001 (2012).

[23] S. L. Lee, S. H. Kilcoyne, and R. Cywinski, eds., *Muon Science* (Institute of Physics, 1999).

[24] A. Pifer, T. Bowen, and K. R. Kendall, Nucl. Instruments Methods **135**, 39 (1976).

[25] B. D. Patterson, Rev. Mod. Phys. **60**, 69 (1988).

[26] A. Yaouanc and P. Dalmas De Réotier, *Muon Spin Rotation, Relaxation, and Resonance* (Oxford University Press, 2011).

[27] P. Dalmas De Réotier and A. Yaouanc, J. Phys. Condens. Matter **9**, 9113 (1997).

[28] M. A. Ruderman and C. Kittel, Phys. Rev. **96**, 99 (1954).

[29] T. Kasuya, Prog. Theor. Phys. **16**, 45 (1956).

[30] K. Yosida, Phys. Rev. **106**, 893 (1957).

[31] R. P. Feynman, *Statistical Mechanics* (Perseus Books, 1972).

[32] E. Roduner and H. Fischer, Chem. Phys. **54**, 261 (1981).

[33] R. P. Feynman, *Feynman Lectures On Physics, Volume III* (Basic Books, 1965).

[34] R. E. Walstedt and L. R. Walker, Phys. Rev. B **9**, 4857 (1974).

[35] R. Kubo, Hyperfine Interact. **8**, 731 (1981).

[36] R. S. Hayano, Y. J. Uemura, J. Imazato, N. Nishida, T. Yamazaki, and R. Kubo, Phys. Rev. B **20**, 850 (1979).

[37] J. E. Sonier, J. H. Brewer, and R. F. Kiefl, Rev. Mod. Phys. **72**, 769 (2000).

[38] E. H. Brandt, Phys. Rev. B **37**, 2349 (1988).

[39] Y. J. Uemura, G. M. Luke, B. J. Sternlieb, J. H. Brewer, J. F. Carolan, W. N. Hardy, R. Kadono, J. R. Kempton, R. F. Kiefl, S. R. Kreitzman, P. Mulhern, T. M. Riseman, *et al.*, Phys. Rev. Lett. **62**, 2317 (1989).

[40] S. J. Blundell, Contemp. Phys. **40**, 175 (1999).

[41] K. W. Kehr, G. Honig, and D. Richter, Zeitschrift für Phys. B **32**, 49 (1978).

[42] A. Keren, Phys. Rev. B **50**, 10039 (1994).

[43] A. Abragam, *Principles of Nuclear Magnetism* (Clarendon Press, 1961).

[44] J. S. Möller, D. Ceresoli, T. Lancaster, N. Marzari, and S. J. Blundell, Phys. Rev. B **87**, 121108 (2013).

[45] T. Lancaster, S. J. Blundell, P. J. Baker, M. L. Brooks, W. Hayes, F. L. Pratt, J. L. Manson, M. M. Conner, and J. A. Schlueter, Phys. Rev. Lett. **99**, 267601 (2007).

[46] J. H. Brewer, S. R. Kreitzman, D. R. Noakes, E. J. Ansaldo, D. R. Harshman, and R. Keitel, Phys. Rev. B **33**, 7813 (1986).

[47] F. L. Pratt, Phys. B Condens. Matter **289-290**, 710 (2000).

[48] S. J. Blundell and F. L. Pratt, J. Phys. Condens. Matter **16**, R771 (2004).

[49] S. J. Blundell, Contemp. Phys. **48**, 275 (2007).

[50] I. Affleck, J. Phys. Condens. Matter **1**, 3047 (1989).

[51] S. Chakravarty, B. I. Halperin, and D. R. Nelson, Phys. Rev. B **39**, 2344 (1989).

[52] P. A. Goddard, J. L. Manson, J. Singleton, I. Franke, T. Lancaster, A. J. Steele, S. J. Blundell, C. Baines, F. L. Pratt, R. D. McDonald, O. E. Ayala-Valenzuela, J. F. Corbey, *et al.*, Phys. Rev. Lett. **108**, 077208 (2012).

[53] S. Ghannadzadeh, J. S. Möller, P. A. Goddard, T. Lancaster, F. Xiao, S. J. Blundell, A. Maisuradze, R. Khasanov, J. L. Manson, S. W. Tozer, D. Graf, and J. A. Schlueter, Phys. Rev. B **87**, 241102 (2013).

[54] S. Sachdev, *Quantum Phase Transitions* (Cambridge University Press, 2011).

[55] N. D. Mermin and H. Wagner, Phys. Rev. Lett. **17**, 1133 (1966).

[56] P. A. Goddard, J. Singleton, P. Sengupta, R. D. McDonald, T. Lancaster, S. J. Blundell, F. L. Pratt, S. Cox, N. Harrison, J. L. Manson, H. I. Southerland, and J. A. Schlueter, New J. Phys. **10**, 083025 (2008).

[57] T. Lancaster, S. J. Blundell, and F. L. Pratt, Phys. Scr. **88**, 068506 (2013).

[58] P. Hasenfratz and F. Niedermayer, Phys. Lett. B **268**, 231 (1991).

[59] M. Greven, R. J. Birgeneau, Y. Endoh, M. A. Kastner, B. Keimer, M. Matsuda, G. Shirane, and T. R. Thurston, Phys. Rev. Lett. **72**, 1096 (1994).

[60] P. Sengupta, A. W. Sandvik, and R. R. P. Singh, Phys. Rev. B **68**, 094423 (2003).

[61] P. A. Goddard, J. Singleton, C. Maitland, S. J. Blundell, T. Lancaster, P. J. Baker, R. D. McDonald, S. Cox, P. Sengupta, J. L. Manson, K. A. Funk, and J. A. Schlueter, Phys. Rev. B **78**, 052408 (2008).

[62] R. T. Butcher, C. P. Landee, M. M. Turnbull, and F. Xiao, Inorganica Chim. Acta **361**, 3654 (2008).

[63] T. Lancaster, S. J. Blundell, F. L. Pratt, M. L. Brooks, J. L. Manson, E. K. Brechin, C. Cadiou, D. Low, E. J. L. McInnes, and R. E. P. Winpenny, J. Phys. Condens. Matter **16**, S4563 (2004).

[64] S. H. Lapidus, J. L. Manson, J. Liu, M. J. Smith, P. Goddard, J. Bendix, C. V. Topping, J. Singleton, C. Dunmars, J. F. Mitchell, and J. A. Schlueter, Chem. Commun. **49**, 3558 (2013).

[65] B. Yan, A. K. Paul, S. Kanungo, M. Reehuis, A. Hoser, D. M. Többens, W. Schnelle, R. C. Williams, T. Lancaster, F. Xiao, J. S. Möller, S. J. Blundell, *et al.*, Phys. Rev. Lett. **112**, 147202 (2014).

[66] R. C. Williams, F. Xiao, I. O. Thomas, S. J. Clark, T. Lancaster, G. A. Cornish, S. J. Blundell, W. Hayes, A. K. Paul, C. Felser, and M. Jansen, J. Phys. Condens. Matter **28**, 076001 (2016).

[67] Y. Tokunaga, N. Furukawa, H. Sakai, Y. Taguchi, T.-H. Arima, and Y. Tokura, Nat. Mater. **8**, 558 (2009).

[68] R. Ramesh and N. A. Spaldin, Nat. Mater. **6**, 21 (2007).

[69] S.-W. Cheong and M. Mostovoy, Nat. Mater. **6**, 13 (2007).

[70] R. J. Cava, B. Batlogg, J. J. Krajewski, R. Farrow, L. W. Rupp, A. E. White,

K. Short, W. F. Peck, and T. Kometani, Nature **332**, 814 (1988).

[71] H. Jin, S. H. Rhim, J. Im, and A. J. Freeman, Sci. Rep. **3**, 1651 (2013).

[72] S. Vasala and M. Karppinen, Prog. Solid State Chem. **43**, 1 (2015).

[73] L. Balents, Nature **464**, 199 (2010).

[74] F. L. Pratt, P. J. Baker, S. J. Blundell, T. Lancaster, S. Ohira-Kawamura, C. Baines, Y. Shimizu, K. Kanoda, I. Watanabe, and G. Saito, Nature **471**, 612 (2011).

[75] A. P. Ramirez, Annu. Rev. Mater. Sci. **24**, 453 (1994).

[76] R. Moessner, Can. J. Phys. **79**, 1283 (2001).

[77] P. D. Battle, T. C. Gibb, C. W. Jones, and F. Studer, J. Solid State Chem. **78**, 281 (1989).

[78] K. Momma and F. Izumi, J. Appl. Crystallogr. **41**, 653 (2008).

[79] K. Momma and F. Izumi, J. Appl. Crystallogr. **44**, 1272 (2011).

[80] K.-I. Kobayashi, T. Kimura, H. Sawada, K. Terakura, and Y. Tokura, Nature **395**, 677 (1998).

[81] K.-I. Kobayashi, T. Kimura, Y. Tomioka, H. Sawada, K. Terakura, and Y. Tokura, Phys. Rev. B **59**, 11159 (1999).

[82] Y. Krockenberger, K. Mogare, M. Reehuis, M. Tovar, M. Jansen, G. Vaitheeswaran, V. Kanchana, F. Bultmark, A. Delin, F. Wilhelm, A. Rogalev, A. Winkler, *et al.*, Phys. Rev. B **75**, 020404 (2007).

[83] H. Das, M. De Raychaudhury, and T. Saha-Dasgupta, Appl. Phys. Lett. **92**, 201912 (2008).

[84] H. Das, P. Sanyal, T. Saha-Dasgupta, and D. D. Sarma, Phys. Rev. B **83**, 104418 (2011).

[85] O. N. Meetei, O. Erten, M. Randeria, N. Trivedi, and P. Woodward, Phys. Rev. Lett. **110**, 087203 (2013).

[86] K. Samanta, P. Sanyal, and T. Saha-Dasgupta, Sci. Rep. **5**, 15010 (2015).

[87] C. Zener, Phys. Rev. **82**, 403 (1951).

[88] P. W. Anderson and H. Hasegawa, Phys. Rev. **100**, 675 (1955).

[89] J. Kanamori and K. Terakura, J. Phys. Soc. Japan **70**, 1433 (2001).

[90] B. J. Kim, H. Jin, S. J. Moon, J.-Y. Kim, B.-G. Park, C. S. Leem, J. Yu, T. W.

Noh, C. Kim, S.-J. Oh, J.-H. Park, V. Durairaj, *et al.*, Phys. Rev. Lett. **101**, 076402 (2008).

[91] B. J. Kim, H. Ohsumi, T. Komesu, S. Sakai, T. Morita, H. Takagi, and T. Arima, Science **323**, 1329 (2009).

[92] J. Kanamori, J. Phys. Chem. Solids **10**, 87 (1959).

[93] J. B. Goodenough, *Magnetism and the Chemical Bond* (Interscience, 1963).

[94] P. W. Anderson, Phys. Rev. **115**, 2 (1959).

[95] A. K. Paul, M. Reehuis, C. Felser, P. M. Abdala, and M. Jansen, Zeitschrift für Anorg. und Allg. Chemie **639**, 2421 (2013).

[96] K. Binder and A. P. Young, Rev. Mod. Phys. **58**, 801 (1986).

[97] R. Morrow, R. Mishra, O. D. Restrepo, M. R. Ball, W. Windl, S. Wurmehl, U. Stockert, B. Büchner, and P. M. Woodward, J. Am. Chem. Soc. **135**, 18824 (2013).

[98] A. K. Paul, M. Jansen, B. Yan, C. Felser, M. Reehuis, and P. M. Abdala, Inorg. Chem. **52**, 6713 (2013).

[99] J. Wang, J. Meng, and Z. Wu, Chem. Phys. Lett. **501**, 324 (2011).

[100] P. Adler, V. Ksenofontov, A. K. Paul, M. Reehuis, B. Yan, M. Jansen, and C. Felser, Hyperfine Interact. **226**, 289 (2014).

[101] A. K. Paul, M. Reehuis, V. Ksenofontov, B. Yan, A. Hoser, D. M. Többens, P. M. Abdala, P. Adler, M. Jansen, and C. Felser, Phys. Rev. Lett. **111**, 167205 (2013).

[102] S. Kanungo, B. Yan, M. Jansen, and C. Felser, Phys. Rev. B **89**, 214414 (2014).

[103] L. S. I. Veiga, G. Fabbris, M. van Veenendaal, N. M. Souza-Neto, H. L. Feng, K. Yamaura, and D. Haskel, Phys. Rev. B **91**, 235135 (2015).

[104] A. J. Steele, T. Lancaster, S. J. Blundell, P. J. Baker, F. L. Pratt, C. Baines, M. M. Conner, H. I. Southerland, J. L. Manson, and J. A. Schlueter, Phys. Rev. B **84**, 064412 (2011).

[105] A. K. Paul, A. Sarapulova, P. Adler, M. Reehuis, S. Kanungo, D. Mikhailova, W. Schnelle, Z. Hu, C. Kuo, V. Siruguri, S. Rayaprol, Y. Soo, *et al.*, Zeitschrift für Anorg. und Allg. Chemie **641**, 197 (2015).

[106] E. V. Kuz'min, S. G. Ovchinnikov, and D. J. Singh, Phys. Rev. B **68**, 024409

(2003).

[107] A. Amato, Rev. Mod. Phys. **69**, 1119 (1997).

[108] P. Dalmas De Réotier, G. Lapertot, A. Yaouanc, P. C. M. Gubbens, S. Sakarya, and A. Amato, Phys. Lett. A **349**, 513 (2006).

[109] J. Major, J. Mundy, M. Schmolz, A. Seeger, K.-P. Döring, K. Fürderer, M. Gladisch, D. Herlach, and G. Majer, Hyperfine Interact. **31**, 259 (1986).

[110] A. A. Aczel, D. E. Bugaris, L. Li, J.-Q. Yan, C. de la Cruz, H.-C. zur Loye, and S. E. Nagler, Phys. Rev. B **87**, 014435 (2013).

[111] A. A. Aczel, P. J. Baker, D. E. Bugaris, J. Yeon, H.-C. zur Loye, T. Guidi, and D. T. Adroja, Phys. Rev. Lett. **112**, 117603 (2014).

[112] K. Lefmann and C. Rischel, Eur. Phys. J. B **21**, 313 (2001).

[113] J. S. Möller, P. Bonfà, D. Ceresoli, F. Bernardini, S. J. Blundell, T. Lancaster, R. De Renzi, N. Marzari, I. Watanabe, S. Sulaiman, and M. I. Mohamed-Ibrahim, Phys. Scr. **88**, 068510 (2013).

[114] S. R. Giblin, I. Terry, S. J. Clark, T. Prokscha, D. Prabhakaran, A. T. Boothroyd, J. Wu, and C. Leighton, Europhys. Lett. **70**, 677 (2005).

[115] P. Bonfà, F. Sartori, and R. De Renzi, J. Phys. Chem. C **119**, 4278 (2015).

[116] M. C. Payne, M. P. Teter, D. C. Allan, T. A. Arias, and J. D. Joannopoulos, Rev. Mod. Phys. **64**, 1045 (1992).

[117] S. J. Clark, M. D. Segall, C. J. Pickard, P. J. Hasnip, M. I. J. Probert, K. Refson, and M. C. Payne, Zeitschrift für Krist. - Cryst. Mater. **220**, 567 (2005).

[118] P. J. Hasnip, K. Refson, M. I. J. Probert, J. R. Yates, S. J. Clark, and C. J. Pickard, Philos. Trans. R. Soc. A Math. Phys. Eng. Sci. **372**, 20130270 (2014).

[119] Jmol: an open-source Java viewer for chemical structures in 3D. http://www.jmol.org/ .

[120] S. J. Blundell, Phys. B Condens. Matter **404**, 581 (2009).

[121] A. E. Taylor, R. Morrow, D. J. Singh, S. Calder, M. D. Lumsden, P. M. Woodward, and A. D. Christianson, Phys. Rev. B **91**, 100406 (2015).

[122] J. S. Gardner, M. J. P. Gingras, and J. E. Greedan, Rev. Mod. Phys. **82**, 53 (2010).

[123] S. T. Bramwell and M. J. P. Gingras, Science **294**, 1495 (2001).

[124] C. Castelnovo, R. Moessner, and S. Sondhi, Annu. Rev. Condens. Matter Phys. **3**, 35 (2012).

[125] C. Castelnovo, R. Moessner, and S. L. Sondhi, Nature **451**, 42 (2008).

[126] L. D. C. Jaubert and P. C. W. Holdsworth, Nat. Phys. **5**, 258 (2009).

[127] S. T. Bramwell, S. R. Giblin, S. Calder, R. Aldus, D. Prabhakaran, and T. Fennell, Nature **461**, 956 (2009).

[128] N. Z. Ali, R. C. Williams, F. Xiao, S. J. Clark, T. Lancaster, S. J. Blundell, D. V. Sheptyakov, and M. Jansen, Phys. Rev. B **91**, 024419 (2015).

[129] K. Mizushima, P. C. Jones, P. J. Wiseman, and J. B. Goodenough, Mater. Res. Bull. **15**, 783 (1980).

[130] B. Wang, J. B. Bates, F. X. Hart, B. C. Sales, R. A. Zuhr, and J. D. Robertson, J. Electrochem. Soc. **143**, 3203 (1996).

[131] E. Antolini, Solid State Ionics **170**, 159 (2004).

[132] M. Jansen and R. Hoppe, Zeitschrift für Anorg. und Allg. Chemie **408**, 104 (1974).

[133] I. Terasaki, Y. Sasago, and K. Uchinokura, Phys. Rev. B **56**, R12685 (1997).

[134] W. Koshibae, K. Tsutsui, and S. Maekawa, Phys. Rev. B **62**, 6869 (2000).

[135] A. Maignan, S. Hébert, L. Pi, D. Pelloquin, C. Martin, C. Michel, M. Hervieu, and B. Raveau, Cryst. Eng. **5**, 365 (2002).

[136] Y. Wang, N. S. Rogado, R. J. Cava, and N. P. Ong, Nature **423**, 425 (2003).

[137] K. Takada, H. Sakurai, E. Takayama-Muromachi, F. Izumi, R. A. Dilanian, and T. Sasaki, Nature **422**, 53 (2003).

[138] R. E. Schaak, T. Klimczuk, M. L. Foo, and R. J. Cava, Nature **424**, 527 (2003).

[139] F. C. Chou, J. H. Cho, P. A. Lee, E. T. Abel, K. Matan, and Y. S. Lee, Phys. Rev. Lett. **92**, 157004 (2004).

[140] T. Fujimoto, G.-Q. Zheng, Y. Kitaoka, R. L. Meng, J. Cmaidalka, and C. W. Chu, Phys. Rev. Lett. **92**, 047004 (2004).

[141] M. Pouchard, A. Villesuzanne, and J.-P. Doumerc, J. Solid State Chem. **162**, 282 (2001).

[142] W. Stählin and H.-R. Oswald, Zeitschrift für Anorg. und Allg. Chemie **373**, 69 (1970).

[143] M. Jansen and R. Hoppe, Zeitschrift für Anorg. und Allg. Chemie **417**, 31 (1975).

[144] J. Birx and R. Hoppe, Zeitschrift für Anorg. und Allg. Chemie **597**, 19 (1991).

[145] M. Sofin, E.-M. Peters, and M. Jansen, J. Solid State Chem. **177**, 2550 (2004).

[146] M. Sofin, H.-U. Güdel, R. Bircher, E.-M. Peters, and M. Jansen, Angew. Chemie **115**, 3651 (2003).

[147] N. Stüßer, M. Sofin, R. Bircher, H.-U. Güdel, and M. Jansen, Chem. Eur. J. **12**, 5452 (2006).

[148] N. Z. Ali, J. Nuss, R. K. Kremer, and M. Jansen, Inorg. Chem. **51**, 12336 (2012).

[149] Z. A. Gál, P. M. Mallinson, H. J. Orchard, and S. J. Clarke, Inorg. Chem. **43**, 3998 (2004).

[150] M. Jansen, Zeitschrift für Anorg. und Allg. Chemie **638**, 1910 (2012).

[151] M. E. Fisher, Philos. Mag. **7**, 1731 (1962).

[152] P. F. Meier, Solid State Commun. **17**, 987 (1975).

[153] A. J. Steele, *Quantum magnetism probed with muon-spin relaxation*, Ph.D. thesis, University of Oxford (2011).

[154] J. H. Brewer, R. F. Kiefl, J. F. Carolan, P. Dosanjh, W. N. Hardy, S. R. Kreitzman, Q. Li, T. M. Riseman, P. Schleger, H. Zhou, E. J. Ansaldo, D. R. Noakes, *et al.*, Hyperfine Interact. **63**, 177 (1991).

[155] L. Van Hove, Phys. Rev. **89**, 1189 (1953).

[156] T. Bayes and R. Price, Philos. Trans. **53**, 370 (1763).

[157] R. Christensen, W. Johnson, A. Branscum, and T. E. Hanson, *Bayesian Ideas and Data Analysis: An Introduction for Scientists and Statisticians* (CRC Press, 2011).

[158] S. J. Blundell, A. J. Steele, T. Lancaster, J. D. Wright, and F. L. Pratt, Phys. Procedia **30**, 113 (2012).

[159] A. J. Steele, P. J. Baker, T. Lancaster, F. L. Pratt, I. Franke, S. Ghannadzadeh, P. A. Goddard, W. Hayes, D. Prabhakaran, and S. J. Blundell, Phys. Rev. B **84**, 144416 (2011).

[160] S. M. Disseler, Phys. Rev. B **89**, 140413 (2014).

[161] R. C. Williams, F. Xiao, T. Lancaster, R. De Renzi, G. Allodi, S. Bordignon, P. G. Freeman, F. L. Pratt, S. R. Giblin, J. S. Möller, S. J. Blundell, A. T. Boothroyd, *et al.*, Phys. Rev. B **93**, 140406 (2016).

[162] P. A. Lee, N. Nagaosa, and X.-G. Wen, Rev. Mod. Phys. **78**, 17 (2006).

[163] V. J. Emery and S. A. Kivelson, Phys. C Supercond. **209**, 597 (1993).

[164] S. A. Kivelson, E. Fradkin, and V. J. Emery, Nature **393**, 550 (1998).

[165] M. Vojta, Adv. Phys. **58**, 699 (2009).

[166] J. G. Bednorz and K. A. Müller, Zeitschrift für Phys. B Condens. Matter **64**, 189 (1986).

[167] B. Keimer, S. A. Kivelson, M. R. Norman, S. Uchida, and J. Zaanen, Nature **518**, 179 (2015).

[168] E. Fradkin and S. A. Kivelson, Nat. Phys. **8**, 864 (2012).

[169] J. M. Tranquada, Phys. B Condens. Matter **407**, 1771 (2012).

[170] R. Comin and A. Damascelli, Annu. Rev. Condens. Matter Phys. **7**, 369 (2016).

[171] V. Hinkov, D. Haug, B. Fauqué, P. Bourges, Y. Sidis, A. Ivanov, C. Bernhard, C. T. Lin, and B. Keimer, Science **319**, 597 (2008).

[172] R. Daou, J. Chang, D. LeBoeuf, O. Cyr-Choinière, F. Laliberté, N. Doiron-Leyraud, B. J. Ramshaw, R. Liang, D. A. Bonn, W. N. Hardy, and L. Taillefer, Nature **463**, 519 (2010).

[173] C. V. Parker, P. Aynajian, E. H. da Silva Neto, A. Pushp, S. Ono, J. Wen, Z. Xu, G. Gu, and A. Yazdani, Nature **468**, 677 (2010).

[174] J. M. Tranquada, B. J. Sternlieb, J. D. Axe, Y. Nakamura, and S. Uchida, Nature **375**, 561 (1995).

[175] Q. Li, M. Hücker, G. D. Gu, A. M. Tsvelik, and J. M. Tranquada, Phys. Rev. Lett. **99**, 067001 (2007).

[176] J. Chang, E. Blackburn, A. T. Holmes, N. B. Christensen, J. Larsen, J. Mesot, R. Liang, D. A. Bonn, W. N. Hardy, A. Watenphul, M. v. Zimmermann, E. M. Forgan, *et al.*, Nat. Phys. **8**, 871 (2012).

[177] N. Hollmann, M. W. Haverkort, M. Cwik, M. Benomar, M. Reuther, A. Tanaka, and T. Lorenz, New J. Phys. **10**, 023018 (2008).

[178] N. Hollmann, M. W. Haverkort, M. Benomar, M. Cwik, M. Braden, and

T. Lorenz, Phys. Rev. B **83**, 174435 (2011).

[179] C. F. Chang, Z. Hu, H. Wu, T. Burnus, N. Hollmann, M. Benomar, T. Lorenz, A. Tanaka, H.-J. Lin, H. H. Hsieh, C. T. Chen, and L. H. Tjeng, Phys. Rev. Lett. **102**, 116401 (2009).

[180] L. M. Helme, A. T. Boothroyd, R. Coldea, D. Prabhakaran, C. D. Frost, D. A. Keen, L. P. Regnault, P. G. Freeman, M. Enderle, and J. Kulda, Phys. Rev. B **80**, 134414 (2009).

[181] K. Yamada, M. Matsuda, Y. Endoh, B. Keimer, R. J. Birgeneau, S. Onodera, J. Mizusaki, T. Matsuura, and G. Shirane, Phys. Rev. B **39**, 2336 (1989).

[182] P. Babkevich, D. Prabhakaran, C. D. Frost, and A. T. Boothroyd, Phys. Rev. B **82**, 184425 (2010).

[183] M. Cwik, M. Benomar, T. Finger, Y. Sidis, D. Senff, M. Reuther, T. Lorenz, and M. Braden, Phys. Rev. Lett. **102**, 057201 (2009).

[184] A. T. Boothroyd, P. Babkevich, D. Prabhakaran, and P. G. Freeman, Nature **471**, 341 (2011).

[185] J. M. Tranquada, H. Woo, T. G. Perring, H. Goka, G. D. Gu, G. Xu, M. Fujita, and K. Yamada, Nature **429**, 534 (2004).

[186] S. M. Hayden, H. A. Mook, P. Dai, T. G. Perring, and F. Doğan, Nature **429**, 531 (2004).

[187] V. Hinkov, P. Bourges, S. Pailhès, Y. Sidis, A. Ivanov, C. D. Frost, T. G. Perring, C. T. Lin, D. P. Chen, and B. Keimer, Nat. Phys. **3**, 780 (2007).

[188] O. J. Lipscombe, S. M. Hayden, B. Vignolle, D. F. McMorrow, and T. G. Perring, Phys. Rev. Lett. **99**, 067002 (2007).

[189] G. Xu, J. M. Tranquada, T. G. Perring, G. D. Gu, M. Fujita, and K. Yamada, Phys. Rev. B **76**, 014508 (2007).

[190] S. M. Gaw, E. C. Andrade, M. Vojta, C. D. Frost, D. T. Adroja, D. Prabhakaran, and A. T. Boothroyd, Phys. Rev. B **88**, 165121 (2013).

[191] I. A. Zaliznyak, J. P. Hill, J. M. Tranquada, R. Erwin, and Y. Moritomo, Phys. Rev. Lett. **85**, 4353 (2000).

[192] I. A. Zaliznyak, J. M. Tranquada, R. Erwin, and Y. Moritomo, Phys. Rev. B **64**, 195117 (2001).

[193] T. Lancaster, S. R. Giblin, G. Allodi, S. Bordignon, M. Mazzani, R. De Renzi, P. G. Freeman, P. J. Baker, F. L. Pratt, P. Babkevich, S. J. Blundell, A. T. Boothroyd, *et al.*, Phys. Rev. B **89**, 020405 (2014).

[194] A. Nemudry, P. Rudolf, and R. Schöllhorn, Solid State Ionics **109**, 213 (1998).

[195] F. Girgsdies and R. Schöllhorn, Solid State Commun. **91**, 111 (1994).

[196] L. Le Dréau, C. Prestipino, O. Hernandez, J. Schefer, G. Vaughan, S. Paofai, J. M. Perez-Mato, S. Hosoya, and W. Paulus, Inorg. Chem. **51**, 9789 (2012).

[197] D. Prabhakaran, P. Isla, and A. T. Boothroyd, J. Cryst. Growth **237-239**, 815 (2002).

[198] C. A. Steer, *Muon Studies of Colossal Magnetoresistive and Related Compounds*, Ph.D. thesis, University of Oxford (2003).

[199] M. Cwik, *The Interplay of Lattice, Spin, and Charge Degrees of Freedom in Layered Cobaltates*, Ph.D. thesis, Universität zu Köln (2007).

[200] Y. Drees, D. Lamago, A. Piovano, and A. C. Komarek, Nat. Commun. **4**, 2449 (2013).

[201] Y. Drees, Z. W. Li, A. Ricci, M. Rotter, W. Schmidt, D. Lamago, O. Sobolev, U. Rütt, O. Gutowski, M. Sprung, A. Piovano, J. P. Castellan, *et al.*, Nat. Commun. **5**, 5731 (2014).

[202] B. O. Wells, Y. S. Lee, M. A. Kastner, R. J. Christianson, R. J. Birgeneau, K. Yamada, Y. Endoh, and G. Shirane, Science **277**, 1067 (1997).

[203] J. M. Tranquada, Y. Kong, J. E. Lorenzo, D. J. Buttrey, D. E. Rice, and V. Sachan, Phys. Rev. B **50**, 6340 (1994).

[204] M. E. J. Newman and R. M. Ziff, Phys. Rev. Lett. **85**, 4104 (2000).

[205] O. P. Vajk, P. K. Mang, M. Greven, P. M. Gehring, and J. W. Lynn, Science **295**, 1691 (2002).

[206] M. Matsuda, M. Fujita, K. Yamada, R. J. Birgeneau, Y. Endoh, and G. Shirane, Phys. Rev. B **65**, 134515 (2002).

[207] E. C. Andrade and M. Vojta, Phys. Rev. Lett. **109**, 147201 (2012).

[208] A. T. Savici, I. A. Zaliznyak, G. D. Gu, and R. Erwin, Phys. Rev. B **75**, 184443 (2007).

[209] Y. Moritomo, K. Higashi, K. Matsuda, and A. Nakamura, Phys. Rev. B **55**,

R14725 (1997).

[210] N. Sakiyama, I. A. Zaliznyak, S.-H. Lee, Y. Mitsui, and H. Yoshizawa, Phys. Rev. B **78**, 180406 (2008).

[211] A. T. Boothroyd, Not yet published .

[212] F. C. Chou, F. Borsa, J. H. Cho, D. C. Johnston, A. Lascialfari, D. R. Torgeson, and J. Ziolo, Phys. Rev. Lett. **71**, 2323 (1993).

[213] F. Borsa, P. Carretta, J. H. Cho, F. C. Chou, Q. Hu, D. C. Johnston, A. Lascialfari, D. R. Torgeson, R. J. Gooding, N. M. Salem, and K. J. E. Vos, Phys. Rev. B **52**, 7334 (1995).

[214] S. Sanna, G. Allodi, G. Concas, A. D. Hillier, and R. De Renzi, Phys. Rev. Lett. **93**, 207001 (2004).

[215] S. Sanna, F. Coneri, A. Rigoldi, G. Concas, S. R. Giblin, and R. De Renzi, Phys. Rev. B **82**, 100503 (2010).

[216] J. Zaanen, G. A. Sawatzky, and J. W. Allen, Phys. Rev. Lett. **55**, 418 (1985).

[217] M. Ogata and H. Fukuyama, Reports Prog. Phys. **71**, 036501 (2008).

[218] A. Aharony, R. J. Birgeneau, A. Coniglio, M. A. Kastner, and H. E. Stanley, Phys. Rev. Lett. **60**, 1330 (1988).

[219] F. C. Zhang and T. M. Rice, Phys. Rev. B **37**, 3759 (1988).

[220] P. W. Anderson, Science **235**, 1196 (1987).

[221] B. Hitti, P. Birrer, K. Fischer, F. N. Gygax, E. Lippelt, H. Maletta, A. Schenck, and M. Weber, Hyperfine Interact. **63**, 287 (1991).

[222] E. Torikai, K. Nagamine, H. Kitazawa, I. Tanaka, H. Kojima, S. B. Sulaiman, S. Srinivas, and T. P. Das, Hyperfine Interact. **79**, 921 (1993).

[223] S. B. Sulaiman, S. Srinivas, N. Sahoo, F. Hagelberg, T. P. Das, E. Torikai, and K. Nagamine, Phys. Rev. B **49**, 9879 (1994).

[224] B. Nachumi, Y. Fudamoto, A. Keren, K. M. Kojima, M. Larkin, G. M. Luke, J. Merrin, O. Tchernyshyov, Y. J. Uemura, N. Ichikawa, M. Goto, H. Takagi, *et al.*, Phys. Rev. B **58**, 8760 (1998).

[225] W. Huang, V. Pacradouni, M. P. Kennett, S. Komiya, and J. E. Sonier, Phys. Rev. B **85**, 104527 (2012).

[226] T. McMullen and E. Zaremba, Phys. Rev. B **18**, 3026 (1978).

[227] V. Sachan, D. J. Buttrey, J. M. Tranquada, J. E. Lorenzo, and G. Shirane, Phys. Rev. B **51**, 12742 (1995).

[228] H. Yoshizawa, T. Kakeshita, R. Kajimoto, T. Tanabe, T. Katsufuji, and Y. Tokura, Phys. Rev. B **61**, R854 (2000).

[229] R. Kajimoto, K. Ishizaka, H. Yoshizawa, and Y. Tokura, Phys. Rev. B **67**, 014511 (2003).

[230] T. Jestädt, K. H. Chow, S. J. Blundell, W. Hayes, F. L. Pratt, B. W. Lovett, M. A. Green, J. E. Millburn, and M. J. Rosseinsky, Phys. Rev. B **59**, 3775 (1999).

[231] C. H. Chen, S.-W. Cheong, and A. S. Cooper, Phys. Rev. Lett. **71**, 2461 (1993).

[232] A. T. Boothroyd, P. G. Freeman, D. Prabhakaran, A. Hiess, M. Enderle, J. Kulda, and F. Altorfer, Phys. Rev. Lett. **91**, 257201 (2003).

[233] K. H. Chow, P. A. Pattenden, S. J. Blundell, W. Hayes, F. L. Pratt, T. Jestädt, M. A. Green, J. E. Millburn, M. J. Rosseinsky, B. Hitti, S. R. Dunsiger, R. F. Kiefl, *et al.*, Phys. Rev. B **53**, R14725 (1996).

[234] T. Lancaster, R. C. Williams, I. O. Thomas, F. Xiao, F. L. Pratt, S. J. Blundell, J. C. Loudon, T. Hesjedal, S. J. Clark, P. D. Hatton, M. Ciomaga Hatnean, D. S. Keeble, *et al.*, Phys. Rev. B **91**, 224408 (2015).

[235] P. M. Chaikin and T. C. Lubensky, *Principles of Condensed Matter Physics* (Cambridge University Press, 1995).

[236] N. Nagaosa and Y. Tokura, Nat. Nanotechnol. **8**, 899 (2013).

[237] T. H. R. Skyrme, Proc. R. Soc. A Math. Phys. Eng. Sci. **260**, 127 (1961).

[238] T. H. R. Skyrme, Nucl. Phys. **31**, 556 (1962).

[239] G. E. Brown and M. Rho, *The Multifaceted Skyrmion* (World Scientific, 2014).

[240] D. C. Wright and N. D. Mermin, Rev. Mod. Phys. **61**, 385 (1989).

[241] U. Al Khawaja and H. Stoof, Nature **411**, 918 (2001).

[242] S. L. Sondhi, A. Karlhede, S. A. Kivelson, and E. H. Rezayi, Phys. Rev. B **47**, 16419 (1993).

[243] L. Brey, H. A. Fertig, R. Côté, and A. H. MacDonald, Phys. Rev. Lett. **75**, 2562 (1995).

[244] V. L. Berezinskii, Sov. Phys. JETP **59**, 907 (1971).

[245] J. M. Kosterlitz and D. J. Thouless, J. Phys. C Solid State Phys. **6**, 1181 (1973).

[246] U. K. Rößler, A. N. Bogdanov, and C. Pfleiderer, Nature **442**, 797 (2006).

[247] S. Mühlbauer, B. Binz, F. Jonietz, C. Pfleiderer, A. Rosch, A. Neubauer, R. Georgii, and P. Böni, Science **323**, 915 (2009).

[248] X. Z. Yu, Y. Onose, N. Kanazawa, J. H. Park, J. H. Han, Y. Matsui, N. Nagaosa, and Y. Tokura, Nature **465**, 901 (2010).

[249] S. Heinze, K. von Bergmann, M. Menzel, J. Brede, A. Kubetzka, R. Wiesendanger, G. Bihlmayer, and S. Blügel, Nat. Phys. **7**, 713 (2011).

[250] A. A. Belavin and A. M. Polyakov, JETP Lett. **22**, 245 (1975).

[251] I. Kézsmárki, S. Bordács, P. Milde, E. Neuber, L. M. Eng, J. S. White, H. M. Rønnow, C. D. Dewhurst, M. Mochizuki, K. Yanai, H. Nakamura, D. Ehlers, *et al.*, Nat. Mater. **14**, 1116 (2015).

[252] C. Pfleiderer and A. Rosch, Nature **465**, 880 (2010).

[253] W. Münzer, A. Neubauer, T. Adams, S. Mühlbauer, C. Franz, F. Jonietz, R. Georgii, P. Böni, B. Pedersen, M. Schmidt, A. Rosch, and C. Pfleiderer, Phys. Rev. B **81**, 041203 (2010).

[254] A. Tonomura, X. Yu, K. Yanagisawa, T. Matsuda, Y. Onose, N. Kanazawa, H. S. Park, and Y. Tokura, Nano Lett. **12**, 1673 (2012).

[255] X. Yu, J. P. DeGrave, Y. Hara, T. Hara, S. Jin, and Y. Tokura, Nano Lett. **13**, 3755 (2013).

[256] X. Z. Yu, N. Kanazawa, Y. Onose, K. Kimoto, W. Z. Zhang, S. Ishiwata, Y. Matsui, and Y. Tokura, Nat. Mater. **10**, 106 (2011).

[257] S. X. Huang and C. L. Chien, Phys. Rev. Lett. **108**, 267201 (2012).

[258] S. D. Bader, Rev. Mod. Phys. **78**, 1 (2006).

[259] M. Bode, M. Heide, K. von Bergmann, P. Ferriani, S. Heinze, G. Bihlmayer, A. Kubetzka, O. Pietzsch, S. Blügel, and R. Wiesendanger, Nature **447**, 190 (2007).

[260] C. Pfleiderer, Nat. Phys. **7**, 673 (2011).

[261] F. Jonietz, S. Mühlbauer, C. Pfleiderer, A. Neubauer, W. Münzer, A. Bauer, T. Adams, R. Georgii, P. Böni, R. A. Duine, K. Everschor, M. Garst, *et al.*,

Science **330**, 1648 (2010).

[262] T. Schulz, R. Ritz, A. Bauer, M. Halder, M. Wagner, C. Franz, C. Pfleiderer, K. Everschor, M. Garst, and A. Rosch, Nat. Phys. **8**, 301 (2012).

[263] M. V. Berry, Proc. R. Soc. A Math. Phys. Eng. Sci. **392**, 45 (1984).

[264] M. Lee, W. Kang, Y. Onose, Y. Tokura, and N. P. Ong, Phys. Rev. Lett. **102**, 186601 (2009).

[265] A. Neubauer, C. Pfleiderer, B. Binz, A. Rosch, R. Ritz, P. G. Niklowitz, and P. Böni, Phys. Rev. Lett. **102**, 186602 (2009).

[266] A. Fert, V. Cros, and J. Sampaio, Nat. Nanotechnol. **8**, 152 (2013).

[267] N. Romming, C. Hanneken, M. Menzel, J. E. Bickel, B. Wolter, K. von Bergmann, A. Kubetzka, and R. Wiesendanger, Science **341**, 636 (2013).

[268] W. Jiang, P. Upadhyaya, W. Zhang, G. Yu, M. B. Jungfleisch, F. Y. Fradin, J. E. Pearson, Y. Tserkovnyak, K. L. Wang, O. Heinonen, S. G. E. te Velthuis, and A. Hoffmann, Science **349**, 283 (2015).

[269] Y. Nii, T. Nakajima, A. Kikkawa, Y. Yamasaki, K. Ohishi, J. Suzuki, Y. Taguchi, T. Arima, Y. Tokura, and Y. Iwasa, Nat. Commun. **6**, 8539 (2015).

[270] S. Seki, X. Z. Yu, S. Ishiwata, and Y. Tokura, Science **336**, 198 (2012).

[271] S. Seki, J.-H. Kim, D. S. Inosov, R. Georgii, B. Keimer, S. Ishiwata, and Y. Tokura, Phys. Rev. B **85**, 220406 (2012).

[272] T. Adams, A. Chacon, M. Wagner, A. Bauer, G. Brandl, B. Pedersen, H. Berger, P. Lemmens, and C. Pfleiderer, Phys. Rev. Lett. **108**, 237204 (2012).

[273] M. C. Langner, S. Roy, S. K. Mishra, J. C. T. Lee, X. W. Shi, M. A. Hossain, Y.-D. Chuang, S. Seki, Y. Tokura, S. D. Kevan, and R. W. Schoenlein, Phys. Rev. Lett. **112**, 167202 (2014).

[274] A. A. Omrani, J. S. White, K. Prša, I. Živković, H. Berger, A. Magrez, Y.-H. Liu, J. H. Han, and H. M. Rønnow, Phys. Rev. B **89**, 064406 (2014).

[275] T. Adams, S. Mühlbauer, C. Pfleiderer, F. Jonietz, A. Bauer, A. Neubauer, R. Georgii, P. Böni, U. Keiderling, K. Everschor, M. Garst, and A. Rosch, Phys. Rev. Lett. **107**, 217206 (2011).

[276] A. Bauer and C. Pfleiderer, Phys. Rev. B **85**, 214418 (2012).

[277] J.-W. G. Bos, C. V. Colin, and T. T. M. Palstra, Phys. Rev. B **78**, 094416 (2008).

[278] M. Belesi, I. Rousochatzakis, H. C. Wu, H. Berger, I. V. Shvets, F. Mila, and J. P. Ansermet, Phys. Rev. B **82**, 094422 (2010).

[279] A. Maisuradze, Z. Guguchia, B. Graneli, H. M. Rønnow, H. Berger, and H. Keller, Phys. Rev. B **84**, 064433 (2011).

[280] O. Janson, I. Rousochatzakis, A. A. Tsirlin, M. Belesi, A. A. Leonov, U. K. Rößler, J. van den Brink, and H. Rosner, Nat. Commun. **5**, 5376 (2014).

[281] I. Dzyaloshinsky, J. Phys. Chem. Solids **4**, 241 (1958).

[282] T. Moriya, Phys. Rev. Lett. **4**, 228 (1960).

[283] T. Moriya, Phys. Rev. **120**, 91 (1960).

[284] M. Ezawa, Phys. Rev. Lett. **105**, 197202 (2010).

[285] T. Okubo, S. Chung, and H. Kawamura, Phys. Rev. Lett. **108**, 017206 (2012).

[286] Y. Zhou, E. Iacocca, A. A. Awad, R. K. Dumas, F. C. Zhang, H. B. Braun, and J. Åkerman, Nat. Commun. **6**, 8193 (2015).

[287] O. Petrova and O. Tchernyshyov, Phys. Rev. B **84**, 214433 (2011).

[288] A. N. Bogdanov, U. K. Rößler, and C. Pfleiderer, Phys. B Condens. Matter **359-361**, 1162 (2005).

[289] U. K. Rößler, A. A. Leonov, and A. N. Bogdanov, J. Phys. Conf. Ser. **303**, 012105 (2011).

[290] M. R. Eskildsen, E. M. Forgan, and H. Kawano-Furukawa, Reports Prog. Phys. **74**, 124504 (2011).

[291] S. Seki, S. Ishiwata, and Y. Tokura, Phys. Rev. B **86**, 060403 (2012).

[292] M. Mochizuki, X. Z. Yu, S. Seki, N. Kanazawa, W. Koshibae, J. Zang, M. Mostovoy, Y. Tokura, and N. Nagaosa, Nat. Mater. **13**, 241 (2014).

[293] E. T. Jaynes, Phys. Rev. **106**, 620 (1957).

[294] E. T. Jaynes, Phys. Rev. **108**, 171 (1957).

[295] B. D. Rainford and G. J. Daniell, Hyperfine Interact. **87**, 1129 (1994).

[296] T. M. Riseman and E. M. Forgan, Phys. B Condens. Matter **289-290**, 718 (2000).

[297] L. Liu and Y. J. Uemura *et. al*, paper presented at MuSR2014, Grindelwald,

Switzerland (Unpublished) (abstract available at www.psi.ch/musr2014) .

[298] N. A. Spaldin and M. Fiebig, Science **309**, 391 (2005).

[299] J. S. White, I. Levatić, A. A. Omrani, N. Egetenmeyer, K. Prša, I. Živković, J. L. Gavilano, J. Kohlbrecher, M. Bartkowiak, H. Berger, and H. M. Rønnow, J. Phys. Condens. Matter **24**, 432201 (2012).

[300] J. S. White, K. Prša, P. Huang, A. A. Omrani, I. Živković, M. Bartkowiak, H. Berger, A. Magrez, J. L. Gavilano, G. Nagy, J. Zang, and H. M. Rønnow, Phys. Rev. Lett. **113**, 107203 (2014).

[301] E. Ruff, P. Lunkenheimer, A. Loidl, H. Berger, and S. Krohns, Sci. Rep. **5**, 15025 (2015).

[302] Y. Tokunaga, X. Z. Yu, J. S. White, H. M. Rønnow, D. Morikawa, Y. Taguchi, and Y. Tokura, Nat. Commun. **6**, 7638 (2015).

[303] D. A. Gilbert, B. B. Maranville, A. L. Balk, B. J. Kirby, P. Fischer, D. T. Pierce, J. Unguris, J. A. Borchers, and K. Liu, Nat. Commun. **6**, 8462 (2015).

[304] T. Lancaster, F. Xiao, Z. Salman, I. O. Thomas, S. J. Blundell, F. L. Pratt, S. J. Clark, T. Prokscha, A. Suter, S. L. Zhang, A. A. Baker, and T. Hesjedal, arxiv 1511.04972 (2015).

[305] E. Karhu, S. Kahwaji, T. L. Monchesky, C. Parsons, M. D. Robertson, and C. Maunders, Phys. Rev. B **82**, 184417 (2010).

[306] Y. Li, N. Kanazawa, X. Z. Yu, A. Tsukazaki, M. Kawasaki, M. Ichikawa, X. F. Jin, F. Kagawa, and Y. Tokura, Phys. Rev. Lett. **110**, 117202 (2013).

[307] T. L. Monchesky, J. C. Loudon, M. D. Robertson, and A. N. Bogdanov, Phys. Rev. Lett. **112**, 059701 (2014).

[308] Y. Li, N. Kanazawa, X. Z. Yu, F. Kagawa, and Y. Tokura, Phys. Rev. Lett. **112**, 059702 (2014).

[309] S. A. Meynell, M. N. Wilson, J. C. Loudon, A. Spitzig, F. N. Rybakov, M. B. Johnson, and T. L. Monchesky, Phys. Rev. B **90**, 224419 (2014).

[310] J. S. Möller, *Muon-spin relaxation and its application in the study of molecular quantum magnets*, Ph.D. thesis, University of Oxford (2013).